Highly Sensitive Quantitative Microscopy for Cellular and Subcellular Analysis

Maxwell Bertrand Zeigler

A dissertation

submitted in partial fulfillment of the

requirements for the degree of

Doctor of Philosophy

University of Washington

2013

Reading Committee:

Daniel Chiu, Chair

Champak Chatterjee

Bo Zhang

Program Authorized to Offer Degree:

Chemistry

University of Washington

Abstract

Highly Sensitive Quantitative Microscopy for Cellular and Subcellular Analysis

Maxwell B. Zeigler

Chair of the Supervisory Committee:

Professor Daniel T. Chiu

Department of Chemistry

The purpose of this research has been to implement optical methods to investigate subcellular biological function. The diffraction limit of light for conventional optical microscopy is roughly $\lambda/2$, or 200 nanometers for visible light; significantly larger than the size of most macromolecules. One way to overcome this limitation is through the careful use of polarization optics and choices in fluorescent probes. Like an antenna, fluorescent molecules have an orientation at which they preferentially absorb polarized electromagnetic radiation. By adjusting the excitation polarization and observing the anisotropic polarization of light emitted from the probe, information about the local environment of the fluorescent probe or macromolecules that they are bound to can be

gleaned on a scale much smaller than the diffraction limit of light. I use this anisotropic polarization to probe the interior of synaptic vesicles which were genetically modified to lack the SV2 glycoprotein. I also made fluorescent polymer nanoparticles that exhibited high fluorescence anisotropy and demonstrated their value as observers of molecular motor function. This was done by observing the rotation of microtubules as they precessed in a microtubule gliding assay. In chapter 4 I discuss the importance of laser choice on cell viability in single-cell nanosurgery. Finally, chapter 5 is a "how-to" guide for building and using optical tweezers that was written for a book on methods in molecular biology.

Table of Contents

List of Figures

List of Tables

Acknowledgements

I would like to thank my advisor Daniel Chiu for his advice and direction through my graduate school career. The depth of his knowledge and his dedication to our research group served as a great example to me, and his even disposition makes him a paragon for the way science should be conducted.

I would like to thank my lab-mates for the collaborative atmosphere we shared and for their assistance in ways big and small. I would particularly like to thank Kady Gregersen, Peter Allen, and John Edgar for their valuable mentorship and great patience when I had no idea what I was doing. Also, many thanks to Wei Sun, Bryant Fujimoto, Yu Rong, and Changfeng Wu; their technical knowledge was invaluable in the completion of this work.

I would like to thank my mother Yaeko and my brother Alex for their continued love and support, and my girlfriend Antoinette for her nearly saint-like patience while I was writing my thesis. You are the center of my universe. Finally, I would like to thank my friends who made these last few years such an exciting and memorable time for me.

Dedication

To my father; I wish you were here to read this.

Chapter 1– Fluorescence Microscopy: Fundamentals, Techniques, and Considerations

1.1 FLUORESCENCE FUNDAMENALS

Excitation and Emission. George C. Stokes first published the observation that certain materials, when illuminated with ultraviolet light, would emit light of a longer wavelength. These materials are now known as fluorophores after the mineral fluorspar (now called fluorite), from which fluorescence received its name. The wavelength of emitted light was always found to be red shifted in comparison to the source, and the difference in energy between absorption and emission is known as the Stokes shift. By selectively filtering the light of excitation and only observing the emitted light, an image consisting primarily of the species of interest can be obtained. In the case of Stokes, he used the sun as his excitation source, a tinted church window as an excitation filter to selectively pass ultraviolet light, and a quinine solution as his fluorescent sample. He used a glass of white wine as an emission filter to absorb the ultraviolet light and isolate the fluorescence from quinine[1]. Modern fluorescence microscopy relies on the same mechanisms for isolating the fluorescence of the species of interest as Stokes used to observe quinine, but in a much different package.

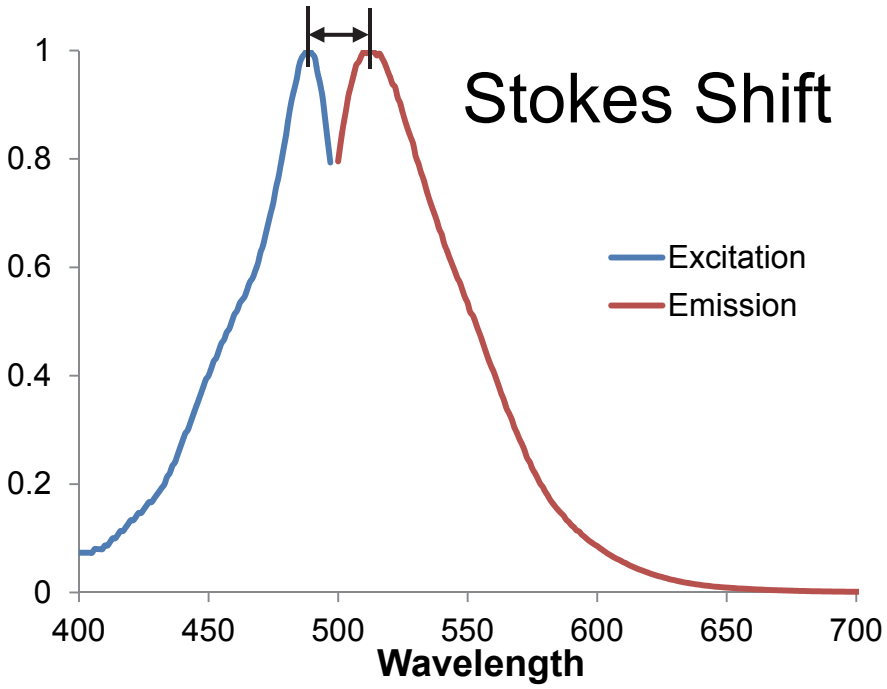

Figure 1.1. Absorption and emission spectra of the organic fluorophore Oregon Green, with stokes shift.

The Stokes shift is the basic principle behind all photoluminescence. If an excited state material emits light quickly, on the time scale of nanoseconds, then it is likely due to fluorescence. Phosphorescence is another form of photoluminescence that emits on the order of microseconds or longer, but it will not be discussed here. At the quantum mechanical level, fluorescence is due to the absorption of a single photon by an electron within a fluorescent molecule, raising the electron's energy from the highest occupied molecular orbital (HOMO) to the lowest unoccupied molecular orbital (LUMO). Vibrational relaxation and spontaneous emission of a photon as the excited electron returns from the LUMO to the HOMO completes the process of fluorescence. The energy difference between the HOMO and the LUMO is dependent on characteristics of the specific molecule. Only certain energy transitions are allowed, as governed by quantum mechanical selection rules[2].

Fluorescence Intensity and Quantum Yield. The ratio of all photons emitted by a fluorophore integrated over all wavelengths, divided by all photons absorbed by a fluorophore is equal to its quantum yield. Due to non-radiative emission, which does not result in a photon, this ratio is always less than one and varies greatly between fluorophores. A fluorophore's brightness can be found by multiplying the quantum yield by the fluorophore's extinction coefficient, which is a measure of how strongly a fluorophore absorbs light at a given wavelength. Generally, the brightness of a fluorophore is linearly proportional to the intensity of excitation light. However, under high intensity excitation from a laser, it is possible to saturate the emission of a fluorophore. In this case, the population in the excited state is too great and the fluorophore must emit a photon before re-absorption. To avoid saturation, it is useful to employ fluorophores with short fluorescence lifetimes as well as high quantum yields to prevent the formation of long-lived triplet excitation states which lower the rate of fluorescence emission.

Microscope Resolution. The resolution power of a microscope is defined by the minimum distinguishable distance between two objects. Assuming that the optical components are free of aberration, then the factor that limits optical resolution is the wave nature of light. Such an optical setup is described as diffraction-limited. As light from a point source passes through the aperture of a microscope objective, it will diffract and form an Airy disk[3]. The Airy Disk is a radially symmetric diffraction pattern of bright and dark rings created by the constructive and destructive interference of light from a single point source with itself as it passes through an aperture. The limit for

resolution is the distance between the first minima and maxima created by two nearby Airy disks. The equation to calculate this resolution limit is shown below.

$$R = \frac{1.22\lambda}{2\eta sin\theta}$$

Where λ is the wavelength of light, η is the refractive index of the medium, and θ is the half angle of light collected by the objective. An example of an Airy Disk is shown in figure 1.2. For an oil immersion objective, the practical limit of resolution for visible light is approximately 170 nanometers. Although objects smaller than this limit cannot be resolved with traditional optical microscopy, single molecules smaller than the limit of resolution can be detected, and resolution can be increased beyond the diffraction limit using fluorescence microscopy techniques that are beyond the scope of this introduction[4].

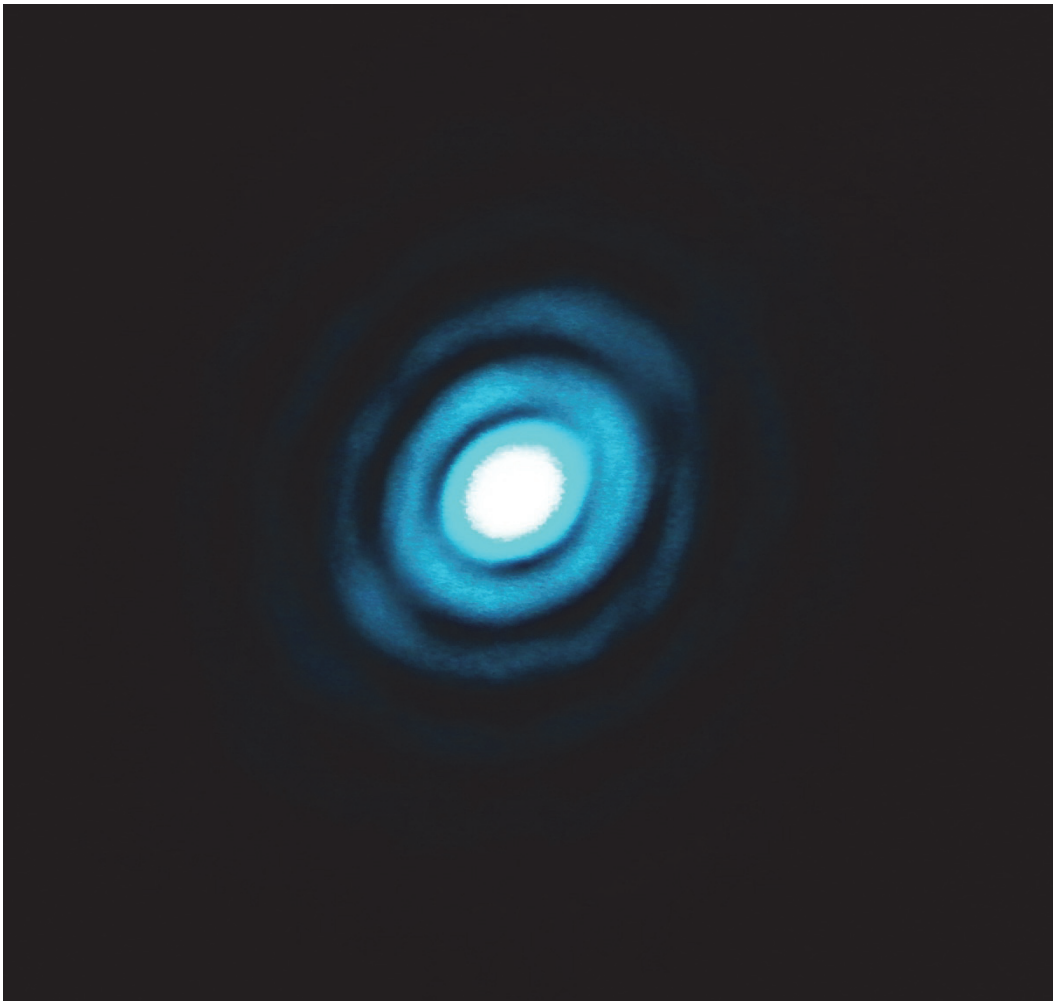

Figure 1.2. An image of an Airy disk formed by a focused laser beam passing through a pinhole.

1.2 OPTICAL TECHNIQUES

Epifluorescence Microscopy. The imaging technique with the most widespread use for observing fluorescent samples is epifluorescence microscopy. By focusing an excitation light source at the rear focal plane of an objective lens, the resulting excitation light will exit the objective and illuminate its sample in a collimated beam as shown in figure 1.3. To prevent vignetting and create even illumination, it is necessary to make

sure that the rear aperture of the objective is filled completely. Fluorescence of the sample is collected using the same objective, and back-scattered excitation light is filtered out using an emission filter. The intensity of the excitation source can be hundreds of thousands of times as intense as the intensity of the fluorescence emission, so use of the proper emission filter is critical in isolating the fluorescent species of interest from the background.

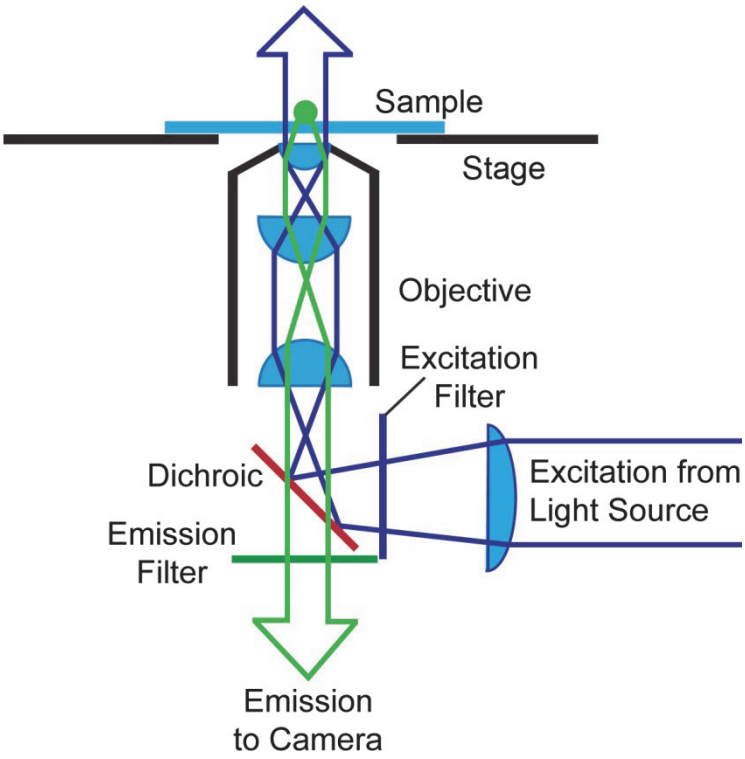

Figure 1.3. Diagram of epifluorescence sample illumination using an inverted microscope. The microscope objective is used for both illumination and imaging of the sample. The blue arrow is a ray trace of the exciting beam and the green arrow is a ray trace of the light emitted by the fluorescent sample.

Because of the technique's simplicity and imaging specificity, its application has been adopted by scientific disciplines too numerous to discuss. The number of fluorescent probes is equally vast; Life Technology's 11th edition of the molecular probes handbook contains over 3,000 novel fluorescent compounds spanning all manner of

desired photophysical and chemical properties[5]. By using the objective for both excitation and observation of the sample, epifluorescence offers some significant advantages over other illumination techniques. First, because only the area currently observed by the objective is being illuminated, photobleaching of the rest of the sample is avoided. Second, because only backscattered light needs to be removed by the emission filter, the background is reduced compared to other excitation geometries. However, fluorophores that are out of the focal plane are also excited and their emitted light can contribute significantly to background fluorescence.

TIRF microscopy. Snell's law dictates that light that reaches a boundary of two transparent media with two separate refractive indices, a portion of the light will be refracted and a portion will be reflected. Beyond a certain critical angle shown below, the light will be totally reflected.

$$\theta = sin^{-1}\left(\frac{\eta_2}{\eta_1}\right)$$

Where η_1 is the refractive index of the first transparent medium (usually a glass coverslip), η_2 is the refractive index of the second transparent medium (usually water or the sample attached to the coverslip), and θ is the critical angle for total internal reflection. At the interface between the two media, an evanescent wave is generated whose intensity decreases exponentially. The depth of this illumination, where illumination intensity decreases to 1/e times the intensity at the surface, is determined by the equation below.

$$d = \frac{\lambda}{4\pi}(\eta_1^2 sin^2\theta - \eta_2^2)$$

Where η_1 is the refractive index of glass, η_2 is the refractive index of the sample, λ is the wavelength of light, and θ is the light's angle of incidence. This penetration depth is normally up to 100 nm. Use of this evanescent wave to excite a fluorescent sample was first utilized by Daniel Axelrod in 1981[6], and this technique became known as Total Internal Reflection Fluorescence microscopy (TIRFm). If the fluorophore of interest is found within the evanescent wave's penetration depth, then it will be excited by the evanescent wave.

TIRF can offer significant advantages. Fluorophores and other objects beyond this thin layer are not illuminated using TIRFm, so contrast is high and the fluorescent background is significantly reduced. The limited penetration depth of exciting light also increases spatial resolution along the z-axis, but limits observations to fluorophores within 100 nm of the coverslip. Confocal microscopy can also improve resolution along the z axis and can make three dimensional images, but for low concentrations of fluorophores, confocal microscopy's method of scanning over a sample pixel by pixel makes it sensitive to blinking events. Normally, a very high numerical aperture (NA) objective is required for objective type TIRF illumination. Because image brightness scales with NA^2 and TIRFm has low background fluorescence, TIRFm is sensitive enough to detect single fluorescent molecules.

Fluorescence Anisotropy. In 1926, Jean Perrin was the first to observe that a fluorescent molecule excited with plane polarized light will emit fluorescent light that is

also polarized if that molecule remains relatively stationary. The extent to which the emitted light is polarized can be described by its anisotropy, r:

$$r = \frac{I_{\parallel} - I_{\perp}}{I_{\parallel} + 2I_{\perp}}$$

Where $I_{\parallel}$ is the measured intensity of light polarized parallel to the exciting light and $I_{\perp}$ is the measured intensity of light polarized perpendicular to the exciting light[7]. An example schematic of how these measurements are taken in a homogeneous bulk solution is shown in figure 1.4, although the same concept in the figure can apply to microscopy and single molecules.

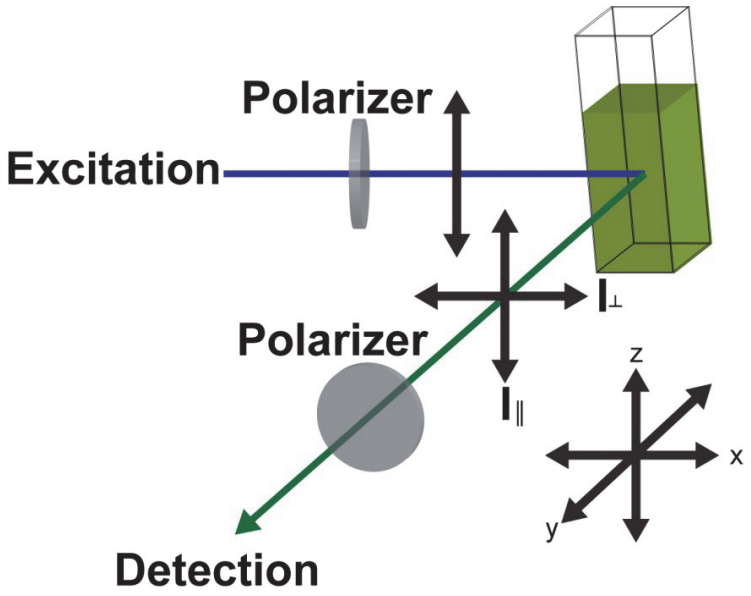

Figure 1.4. Schematic of a system for taking anisotropic measurements of a bulk homogeneous solution.

Because of the fluorophore's preferential absorption of light aligned with its absorption dipole and emission aligned with its emission dipole, fluorophores excited with polarized light can have polarized emission. This allows for the selective excitation of fluorophores in a solution even if they are randomly oriented. The emitted light can

become depolarized by several mechanisms. For single molecules in solution, the primary means of depolarization is through rotational diffusion of the molecule on a timescale faster than its fluorescence lifetime. This depolarization from rotational diffusion can be used to probe a fluorophore's environment, or to measure physical changes in the fluorophore such as binding to a ligand without direct contact with the sample. This is described using the Perrin equation:

$$\frac{r_0}{r} = 1 + \frac{\tau}{\theta}$$

Where r_0 is the anisotropy of a stationary fluorophore aligned with the excitation polarization, τ is the fluorophore's fluorescence lifetime, r is the measured anisotropy, which decays over time according to the equation:

$$r = r_0 e^{-\frac{\tau}{\theta}}$$

And θ is its rotational correlation time:

$$\theta = \frac{\eta V}{RT}$$

Where η is the rotational viscosity of the solvent, V is the hydrodynamic volume of the fluorophore, R is the gas constant, and T is the temperature. This equation for the rotational correlation time assumes that the fluorophore is a sphere, although single molecule studies have shown it works for other shapes[8]. Small molecules in low viscosity solutions exhibit almost no fluorescence anisotropy because their rotational motion is fast compared to their fluorescence lifetime. The viscosity of the solution and the size of the molecule must be selected carefully to find a useful range over which steady state

anisotropy measurements can be made. However, if the fluorescent probe and target are suitable, fluorescence anisotropy provides real-time, fast, sensitive, and non-destructive measurements, which makes it quite valuable.

A single immobilized fluorophore with a parallel absorption and emission dipoles that are aligned with the plane-polarized excitation light could, in theory, have an anisotropy of r=1. If a single fluorophore emitted every photon orthogonally to the plane polarized emission, then it could have a theoretical anisotropy of r=-1. However, fluorophores in homogeneous solution are not perfectly oriented with respect to the excitation polarization, and the likelihood of absorption is proportional to the angle between the absorption dipole and plane of polarization. Also, the direction emission is a probabilistic quantity and this further limits anisotropy. For immobile fluorophores in homogeneous solution where absorption and emission dipoles are the same, the maximum anisotropy value is 0.4 and the minimum is -0.2. If there is a difference between the absorption and emission dipoles the maximum possible anisotropy is further reduced to:

$$r_0 = \frac{2}{5}\left(\frac{3cos^2\beta - 1}{2}\right)$$

Where β is the angle between the excitation and emission dipoles[7].

If a fluorophore is bound to a molecular motor with a well characterized geometry, fluorescence polarization anisotropy can be used to make inferences into changes in the position of the molecular motor. As the position and orientation of the motor change, so does the fluorophore. This can provide information beyond the spatial

measurements attained through typical fluorescence microscopy. If the orientations of the excitation and emission dipoles are known as well as the orientation of the fluorophore upon the target, then direct angular measurements of conformational changes are possible. Examples of useful positional changes would be the F_0 motor of ATPase, myosin movement along actin[9], kinesin movement along microtubules (see Chapter 3), DNA winding or unwinding, or the orientation of nuclear pores[10].

Optical Trapping. Optical trapping is a technique first reported by Arthur Ashkin in 1986[11] that relies on the ability of a high power laser focused through a high NA objective to produce radiation pressure by transferring momentum from the light to the object[12]. This pressure, on the order of piconewtons, is enough to trap or steer objects on the size scale of nanometers to a few microns as long as their refractive index is higher than the surrounding medium. The radiation pressure originates from the refraction of light as it goes from the lower refractive index media to the higher refractive index particle. Upon refraction the direction of the light is changed, and the change in the light's momentum applies two forces on the particle, a scattering force which pushes the object in the direction of the motion of the photons and a gradient force which pulls the object in the direction of highest light intensity. Because of this pull in the direction of highest intensity, if a laser with a Gaussian beam profile is used then the net force upon the object will direct it towards the focal point of the laser beam where it will be "trapped" in three dimensions. It is also possible to make multiple optical traps simultaneously using a "time sharing"[13] approach, multiple overlapping Gaussian

beams[14], or through the use of a spatial light modulator[15]. Optical traps using non-Gaussian beam profiles can also be made using optical vortices[16] or Bessel beams[17].

Optical trapping has the advantage of non-invasively interacting with the object, so it can be used like a pair of "optical tweezers" to manipulate a sample with a high degree of precision and without direct interference. The object that is trapped is manipulated by moving the trap location, which is accomplished using a mechanical mirror in the trapping laser's beam path at a conjugate image plane before the microscope objective. The force applied to the trapped object varies predictably depending on the parameters of the trap used, and force that displaces the object from the center of the trap follows Hooke's Law. The force generated by optical trapping is measurable, reproducible, and well suited to force measurements on many microscopic biological samples like molecular motors, DNA binding, or protein folding. Measurements can be made thousands of times per second, with spatial accuracy at the sub-nanometer level[18]. These force measurements are often facilitated by binding the biological molecule of interest to a large bead whose displacement within the optical trap can be more easily observed.

Laser Ablation. The use of a focused pulse of laser light can apply a high light intensity to a small sample volume over a short period of time. Absorption of the light pulse can cause rapid heating of the sample volume over time periods faster than heat can be transferred. This results in the generation of thermal and mechanical transients, leading to ablation of the sample volume[19]. Laser ablation can also proceed through a non-thermal mechanism; in that case it is likely to be photochemical in nature.

Photochemical ablation is due to reactions precipitated by an interaction between a chemical bond and an individual photon, and are primarily caused by lasers in the deep UV part of the spectrum (λ<200 nm)[20]. The mechanistic description of the laser ablation varies greatly with the energy density applied to the sample volume, the wavelength, the pulse duration (typically 10^{-9} to 10^{-13} seconds), and the optical properties of the sample[21]. The volume of ablated sample varies with the mechanism, but can be used with biological samples with a wide variety of uses from the large scale, such as tissue sculpting in refractive surgery[22], to the cellular level in ablating synapses[23], to targeting sub-cellular components such as single chromosomes[24] or mitochondria[25].

Because laser ablation is useful in a similar size regime and uses similar optics, laser ablation is a technique complimentary with optical trapping. A single cell may have its cellular membrane ablated using a pulsed laser, while an organelle of interest is removed using an optical trap[26]. Although the ideal laser for each technique may be different, both optical trapping and laser ablation require a tightly focused Gaussian beam, and so both have similar considerations in the construction and use of the necessary optical components. Optical trapping is sometimes referred to as "laser tweezers" and laser ablation is referred to as "laser scissors", and the two of them combined are "laser surgery"[27].

1.3 CONSIDERATIONS FOR QUANTITATIVE FLUORESCENCE MICROSCOPY

The optical system design employed for a particular application needs to be carefully considered to balance the inherent trade-offs associated with optical microscopy which will be briefly covered here. The most important parameter to optimize depends on the application, but generally it is the signal-to-noise ratio of the system. Fluorescence experiments inevitably require sacrifices when considering the trade-offs between maximizing the signal, spatial, temporal, and spectral resolution.

Assuming the detector is not being saturated, it is important to collect as many photons from a given sample as possible. One reason for this is that by maximizing the number of photons, it is possible to improve localization of the fluorophore beyond the diffraction limit. By fitting the emission of the collected photons to a two dimensional Gaussian function and increasing the signal to noise ratio, one can localize the center to a nearly arbitrarily small area[28]. In order to reach this level of resolution, it is important to have high enough magnification and small enough camera pixels such that the Nyquist limit is overcome and under-sampling the image does not lead to misinterpretation. However, intensity is inversely proportional to the magnification squared, so empty magnification after the Nyquist limit is satisfied will reduce signal without benefit. The Nyquist limit for resolution in the x-y axis is roughly $\lambda/4NA$, or roughly double the diffraction limit of resolution.

Typical single organic fluorophores emit roughly 10^4-10^6 photons before they enter a permanent dark state due to photobleaching. Inorganic semiconducting

nanocrystals, or quantum dots, can emit roughly 10^9 photons before photobleaching, but they are prone to sporadic non-emissive states known as blinking that last 10^{-3}-10^2 seconds. Collapsed fluorescent polymer chains contain many conjugated chromophores, and can emit anywhere from 10^7-10^{10} photons before irreversible photobleaching and blink less frequently than quantum dots[29].

For each fluorophore, there is a wide range of labeling strategies available. Click chemistry allows for highly specific "bio-orthogonal" labeling, which leads to little interference in biological function. Other fluorophore chemical linkages include binding to primary amines using isothiocyanate and succinimidyl esters, or maleimide functionalized fluorophores for binding to sulfhudryl groups like those found in cysteine. Non-covalent linkage can be obtained using antibodies or biotin/streptavidin linkages. Size restrictions can inhibit fluorescent labeling of intracellular targets, so one can use small organic fluorophores or endogenously express fluorophores through transfection and expression of fluorescent proteins such as GFP.

Through the use of reagents that stabilize emitters or reduce oxidative damage to chromophores, it is possible to increase the total number of photons emitted before photobleaching occurs. Glucose oxidase and catalase are used together to remove oxygen from solution, which leads to nonfluorescent triplet states or irreversible chemical reactions between oxygen and the fluorophore. Other emission stabilizers, such as β-mercaptoethanol, dithiothreitol, or selectively oxidizing/reducing systems, are fluorophore specific and can decrease the time before photobleaching if the wrong chemicals are used.

Signal can also be improved through the use of electron-multiplying charge-coupled device (EMCCD) cameras, which use cooled CCDs and high voltage gain to reduce thermal noise while efficiently collecting photons. New EMCCD are capable of a quantum efficiency of greater than 0.9 across the visible spectrum, and are generally preferable to cameras using complimentary metal-oxide semiconductor sensors (CMOS). EMCCD acquisition rates are lower than devices such as avalanche photodiodes (APD), but each APD is limited to a single point instead of a 2-D array and have a reduced dynamic range compared to EMCCDs. EMCCDs may have pixels that register higher intensities than others, leading to "hot pixels." This can be corrected after the acquisition through subtraction of a dark background image. Other post-acquisition image correction techniques are commonly employed in order to "flatten" the brightness of an image, de-convolve point spread functions, or test for co-localization of multicolor fluorescent labels.

REFERENCES

1. Stokes, G. G. On the Change of Refrangibility of Light. *Philosophical Transactions of the Royal Society of London* **1852**, *142*, 462–562.
2. Atkins, P.; Paula, J. de *Physical Chemistry*; 9th ed.; Oxford University Press, 2009.
3. Grievenkamp, J. E. *Field Guide to Geometrical Optics*; SPIE Press: Bellingham, WA USA, 2004; Vol. FG01.
4. Huang, B.; Bates, M.; Zhuang, X. Super Resolution Fluorescence Microscopy. *Annu Rev Biochem* **2009**, *78*, 993–1016.
5. *Molecular Probes Handbook, A Guide to Fluorescent Probes and Labeling Technologies*; Johnson, I.; Spence, M. T. Z., Eds.; 11th ed.; Life Technologies, 2010.
6. Axelrod, D. Cell-substrate Contacts Illuminated by Total Internal Reflection Fluorescence. *JCB* **1981**, *89*, 141–145.
7. Lakowicz, J. R. *Principles of Fluorescence Spectroscopy*; 3rd ed.; Springer, 2006.
8. Adhikari, S.; Selmke, M.; Cichos, F. Temperature Dependent Single Molecule Rotational Dynamics in PMA. *Phys. Chem. Chem. Phys.* **2011**, *13*, 1849–1856.
9. Forkey, J. N.; Quinlan, M. E.; Shaw, M. A.; Corrie, J. E. T.; Goldman, Y. E. Three-dimensional Structural Dynamics of Myosin V by Single-molecule Fluorescence Polarization. *Nature* **2003**, *422*, 399–404.
10. Kampmann M; Atkinson C.E; Mattheyses A.L; Simon S.M Mapping the orientation of nuclear pore proteins in living cells with polarized fluorescence microscopy. *Nat. Struct. Mol. Biol. Nature Structural and Molecular Biology* **2011**, *18*, 643–649.
11. Ashkin, A.; Dziedzic, J. M.; Bjorkholm, J. E.; Chu, S. Observation of a Single-beam Gradient Force Optical Trap for Dielectric Particles. *Optics Letters* **1986**, *11*, 288–290.
12. Block, S. M. Making Light Work with Optical Tweezers. *Nature* **1992**, *360*, 493–495.
13. Moffitt, J. R.; Chemla, Y. R.; Smith, S. B.; Bustamante, C. Recent Advances in Optical Tweezers. *Annual Reviews of Biochemistry* **2008**, *77*, 205–228.
14. Dholakia, K.; Spalding, G.; MacDonald, M. Optical Tweezers: The Next Generation.

15. Reicherter M; Haist T; Wagemann EU; Tiziani HJ Optical particle trapping with computer-generated holograms written on a liquid-crystal display. *Optics letters* **1999**, *24*, 608–10.
16. Ng, J.; Lin, Z.; Chan, C. T. Theory of Optical Trapping by an Optical Vortex Beam. *Phys. Rev. Lett.* **2010**, *104*, 103601.
17. Arlt, J.; Garces-Chavez, V.; Sibbett, W.; Dholakia, K. Optical Micromanipulation Using a Bessel Light Beam. *Optics Communications* **2001**, *197*, 239–245.
18. Denk, W.; Webb, W. W. Optical Measurement of Picometer Displacements of Transparent Microscopic Objects. *Appl. Opt.* **1990**, *29*, 2382–2391.
19. Vogel, A.; Venugopalan, V. Mechanisms of Pulsed Laser Ablation of Biological Tissues. *Chemical Reviews* **2003**, *103*, 577–644.
20. Yingling, Y. G.; Garrison, B. J. Photochemical Ablation of Organic Solids. *Nuclear Instruments and Methods in Physics Research B* **2003**, *202*, 188–194.
21. Niemz, M. H. *Laser-Tissue Interactions: Funamentals and Applications*; Springer: Heidelberg, Germany, 2004.
22. Cr, M.; Sj, K.; J, M. Photorefractive keratectomy: a technique for laser refractive surgery. *J Cataract Refract Surg* **1988**, *14*, 46–52.
23. Allen, P. B.; Sgro, A. E.; Chao, D. L.; Doepker, B. E.; Scott Edgar, J.; Shen, K.; Chiu, D. T. Single-synapse Ablation and Long-term Imaging in Live C. Elegans. *Journal of Neuroscience Methods* **2008**, *173*, 20–26.
24. Fukui, K.; Minezawa, M.; Kamisugi, Y.; Ishikawa, M.; Ohmido, N.; Yanagisawa, T.; Fujishita, M.; Sakai, F. Microdissection of Plant Chromosomes by Argon-ion Laser Beam. *Theoret. Appl. Genetics* **1992**, *84*, 787–791.
25. Allen, P. B.; Doepker, B. R.; Chiu, D. T. High-Throughput Capillary-Electrophoresis Analysis of the Contents of a Single Mitochondria. *Analytical Chemistry* **2009**, *81*, 3784–3791.
26. Shelby, J. P.; Edgar, J. S.; Chiu, D. T. Monitoring Cell Survival After Extraction of a Single Subcellular Organelle Using Optical Trapping and Pulsed-nitrogen Laser Ablation. *Photochem. Photobiol.* **2005**, *81*, 994–1001.
27. Berns, M. W.; Tadir, Y.; Liang, H.; Tromberg, B. Laser Scissors and Tweezers. *Methods Cell Biol.* **1998**, *55*, 71–98.
28. Yildiz, A.; Selvin, P. R. Fluorescence Imaging with One Nanometer Accuracy: Application to Molecular Motors. *Accoun* **2005**, *38*, 574–582.
29. Wu, C.; Chiu, D. T. Highly Fluorescent Semiconducting Polymer Dots for Biology and Medicine. *Angewandte Chemie International Edition* **2013**, n/a–n/a.

Chapter 2: Probing Rotational Viscosity in Synaptic Vesicles

2.1 INTRODUCTION

The fusion of neurotransmitter-containing synaptic vesicles (SVs) is the primary signaling event between neurons. Work over the last decade has identified most of the proteins associated with SVs and studies aimed at determining where these proteins act in the cycle of vesicle formation, filling, targeting, fusion, and recycling are elucidating the molecular pathway that underlies synaptic transmission (1-3). As the next stage in understanding the functioning of SVs, we are interested in applying sensitive optical techniques for studying individual SVs with single-molecule resolution. We believe the small size (only ~ 40nm in diameter) of SVs makes them potentially amenable to high-resolution single-molecule experimentations and thorough biophysical studies. This paper reports measurements of the rotational viscosity inside individual SVs.

It has been suggested that the interior of SVs may be gel-like, with a proteoglycan matrix that changes size upon neurotransmitter loading (4, 5). Furthermore, it is thought that the synaptic vesicle protein SV2 (6), which is a twelve trans-membrane domain protein with heavily glycosylated intra-vesicular domains, is largely responsible for the gel-like interior of synaptic vesicles. SV2 comes in 3 isoforms; A, B, and C, of which A and B are the most numerous. SV2A and SV2B are critical for proper synaptic vesicle function and mice that lack these SV2 proteins, SV2A and SV2B double knockouts (SV2 DKO), die within 3 weeks (7). SV2 resembles several well-known membrane transport

proteins (1), is the binding target of the anti-epileptic drug levetiracetam (8, 9), and is the route of entry for botulinum toxin (10). By measuring the rotational diffusion rates of the small fluorescent molecule Oregon Green (OG (11)) within both wild type and SV2 DKO synaptic vesicles, we report SV2 is indeed an important determinant of viscosity in SVs.

We have recently reported that the hydrodynamic diameters of synaptic vesicles increase by as much as 25%, which corresponds to a doubling of the volume, when the vesicles are loaded with glutamate (5). Given the large change in vesicle size upon loading with glutamate, we also decided to gain a better understanding on how the luminal viscosity might change between vesicles that are empty versus those filled with glutamate. In our studies, we focused on the neurotransmitter glutamate because we estimated that ~80% of SVs in the brain are glutamatergic (5). By measuring the rotational viscosity in empty and glutamate-filled vesicles, we report that the presence of glutamate results in a decrease in the luminal viscosity of SVs.

Through these two sets of studies, we aim to gain a better understanding of the local environment inside the synaptic vesicle, how tightly organized is the internal matrix of the vesicle, whether SV2 is indeed the key determinant of the luminal viscosity, and also how the internal matrix might change as the vesicle becomes filled with neurotransmitters. Our study provides biophysical insight into the luminal environment of the synaptic vesicle, and represents the smallest sub-cellular organelle in which rotational viscosity has been probed.

2.2 EXPERIMENTAL

Synaptic vesicle isolation and purification. Wild type SVs were collected from commercially stripped mouse brains (Pel-Freeze, Rogers, AR) or from SV2 DKO mouse brains graciously provided by the Bajjalieh lab. The mouse brains were grounded with liquid nitrogen in a Waring blender and homogenized in 50 mM HEPES, 2mM EGTA, and 0.3 M sucrose at pH 7.4 with 20 strokes in a glass-Teflon homogenizer. The homogenate was spun in an ultracentrifuge (Beckman Coulter, Fullerton, CA) at 100,000× g for 28 min to pellet cell debris. The supernatant containing SVs was removed and the pellet was discarded. The supernatant was further purified by layering onto a 1.5/0.6 M sucrose step gradient and spun at 260,000× g for 72 min. The SVs were subsequently removed from the interface of the step sucrose gradients. The vesicles were separated into aliquots and flash frozen in liquid nitrogen and stored at -80℃ until use. All of the buffered solutions were made using Milli-Q water (Millipore, Billerica, MA).

Loading of synaptic vesicles with Oregon Green. The details of loading Oregon Green 488 (OG) (Invitrogen, Carlsbad, CA) into SVs have been described elsewhere (11). Briefly, SVs were loaded with OG by first using a syringe to load the SVs into a microfluidic chip. SVs in solution adsorbed onto the coverslip glass surface (which formed the floor of the microchannel), at which point their media was replaced with a pH 5.1 citrate buffered solution containing 290 mM glycine, 10 mM citrate, and 5 μM OG ("load buffer") for 5 minutes to load OG into the vesicles. The buffered OG solution was then flushed out using a pH 7.2 solution containing 10 mM HEPES and 290 mM glycine ("clear buffer").

For the 2-color overlay experiment, wild type mouse SVs were labeled with anti-SV65 monoclonal primary antibody for 15 min at 20℃ and then labeled with secondary antibody conjugated with the fluorescent probe Alexa Fluor 633 (Invitrogen) for an additional 15 min at 20℃. Excess antibody was removed using IgG conjugated agarose beads specific to the primary and secondary antibody in two steps. SVs were incubated for 45 min at 20 ℃ with the IgG beads, and then the beads were separated via centrifugation at 1000× g for 2 min. The supernatant containing fluorescently labeled SVs was removed and the SVs were imaged in a PDMS well, which was sealed to a glass coverslip after exposure to oxygen plasma.

Glutamate loading assay. Loading glutamate into SVs was verified by a NADPH fluorescence assay. SVs were loaded with glutamate by adding a solution of 10 mM HEPES, 4 mM KCl, 4 mM $MgSO_4$, 0.3 M sucrose, 1.0 mM Glutamate, and 1 mM ATP. After loading for 10 min, the SVs were pelleted by centrifugation at 125,000× g for 30 min. The supernatant was removed and the pellet was repeatedly rinsed with "clear" buffer and then re-suspended in 10 mM HEPES, 150 mM KCl, 0.30 M glucose, 1 mM $NADP^+$, and 1.4 mg/mL L-glutamic dehydrogenase (Sigma Aldrich, St. Louis, MO). The SVs were ruptured in a sonication bath, and the presence of NADPH was detected by a Fluorolog 3 (Horiba, Edison, NJ) with excitation set to 360 nm.

Microscope setup. Imaging was carried out using an inverted TE-2000 microscope (Nikon, Melville, NY) equipped with a 100× magnification and 1.3 numerical aperture (NA) objective. The samples were illuminated using a Sapphire 488 nm laser (Coherent, Santa Clara, CA), directed through a polarizing beam splitter cube;

polarization was adjusted using a zero order λ/2 waveplate. The microscope was also equipped with a 500 long-pass (LP) emission filter and a 355/488/633/1064 polychroic beam splitter. The emitted light was separated by polarization using a home-built setup and imaged onto a Cascade 512b EMCCD camera (Photometrics, Tuscon, AZ). For two-color imaging, a 633 nm HeNe (Coherent) was also used, and TIRF illumination was employed using a 60× magnification 1.45 NA objective (Nikon). Red fluorescence was collected using a 695/100 band-pass filter. All optics and opto-mechanics used were purchased from either Thorlabs (Newton, NJ) or Newport (Irvine, CA). All experiments were carried out at a temperature of 17-18 ℃.

Optical corrections. The G-factor, a term used to correct for the instrument's sensitivity difference between $I_{\parallel}$ compared to $I_{\perp}$, was re-evaluated regularly, but no measurable changes were detected. Subtraction of the background and instrumental bias from the fluorescence images of SVs was carried out using Metamorph (Molecular Devices, Sunnyvale, CA) software.

Microfluidic chip. All anisotropy measurements were carried out in a microchannel with a dimension of 1 mm wide × 100 μm tall × 25 mm long. The microchannel was created by first making a chrome mask of the features desired and aligning the mask above a silicon wafer with a 100 μm layer of the negative photoresist SU-8 spin-coated onto its surface. The wafer was exposed to UV light, and after washing and development steps, a silicon master with the desired features was left. A polydimethylsiloxane (PDMS)/catalyst mixture was then poured onto the master and allowed to harden in a 60℃ oven for several hours. The PDMS mold was removed from

the silicon master and bonded to a glass coverslip after exposure to oxygen plasma. Solutions and SVs were injected into the microchannel via a syringe. Prior to plasma bonding, the glass coverslips used were cleaned by placing them in a boiling solution of 1 : 1 : 1 of water : ammonium hydroxide : 30% hydrogen peroxide for 2 hours followed by thorough rinsing with milli-Q water.

Measurements of fluorescence lifetime. The fluorescence lifetime of Oregon Green inside of SVs was measured using a 470 nm picosecond laser coupled to a Picoharp 300 TCSPC (PicoQuant, Berlin, Germany). SVs were loaded with Oregon Green and glutamate, and then pelleted via centrifugation at 125,000× g for 30 min. The supernatant was removed; the pellet was thoroughly rinsed, then re-suspended in a cuvette with "clear" buffer. The presence of intact SVs following this process was verified by microscopy. We observed re-suspended synaptic vesicles under epi-illumination prepared in this manner and did not observe noticeable OG leakage from the vesicles within our timescale of measurement.

2.3 RESULTS AND DISCUSSION

Because of the extremely small volume enclosed within a synaptic vesicle (~ 40nm in diameter, which corresponds to a volume of ~ 2×10^{-20} L within the SV membrane), it is difficult to probe its internal environment by following a molecule's translational motion within this tightly confined space. As a result, we decided to follow the rotational diffusion of molecules within this intra-vesicular volume using fluorescence polarization anisotropy (12). Here, a fluorophore's anisotropy, *r*, is a

comparison of the difference between the intensity of light emitted that is parallel to the polarization of the excitation light ($I_{||}$) and the intensity of emission perpendicular to the excitation polarization ($I_{\perp}$) divided by the total light intensity. Specifically,

$$r = (I_{||} - I_{\perp} \times G) / (I_{||} + 2 \times I_{\perp} \times G)$$

where G is a correction factor for instrumental bias. The ratio between measured anisotropy and the theoretical maximum anisotropy can be used to find a fluorophore's rotational correlation via the Perrin Equation,

$$(r_0 / r) = 1 + \tau / \theta$$

where r_0 is the maximum anisotropy of a stationary fluorophore, τ is the fluorescence lifetime, and θ is the rotational correlation time. The rotational correlation time is proportional to the viscosity of the medium as shown by the equation,

$$\theta = (\eta V) / (kT)$$

where η is the solvent viscosity, V is the hydrodynamic volume of the rotating unit, k is Boltzmann's constant, and T is temperature (13).

Loading of synaptic vesicles with Oregon Green. To measure the rotational viscosity inside SVs using fluorescence polarization anisotropy, we must be able to introduce fluorophores into the interior volume of the vesicles. Here, we take advantage of an observation we made previously (11), where when the pH of the solution around vesicles was lowered to ~ 5.1, OG could be loaded. OG could be loaded only in this specific pH range and it leaks out slowly at physiological pH. The mechanism of OG uptake into synaptic vesicles is not clear, but several lines of evidence show they are not non-specifically adsorbed on the surface of the vesicles.

To verify that we were observing SVs and that they were indeed loaded with OG, we labeled SVs with primary monoclonal antibody against the membrane protein SV65 and a red fluorescent secondary antibody (Alexa633), which was spectrally distinct from the green emission of OG. The antibody-labeled SVs were then loaded with OG, after which we used two-color TIRF (total-internal-reflection fluorescence) microscopy to image the antibody-labeled (red) and the OG loaded (green) SVs, and to ensure OG were indeed loaded selectively into the SVs as identified with the SV-specific antibody. Figure 2.1 A shows representative two-color images, in which it is evident there is good overlay between the antibody-labeled (red) and the OG-loaded (green) SVs, which indicates high specificity of OG loading into SVs. Given the photostability and relative insensitivity to pH, OG is a robust fluorescence probe for the lumen of SVs.

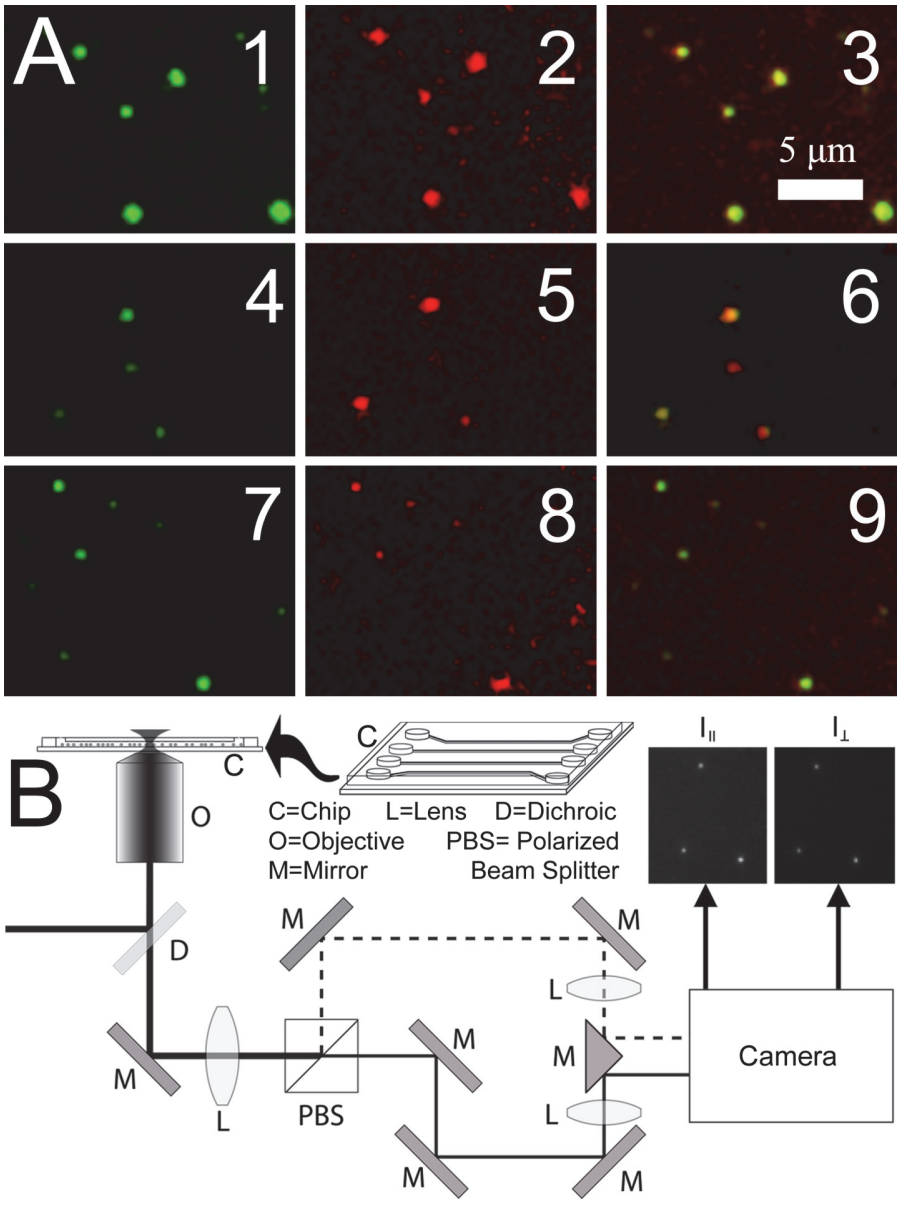

Figure 2.1. Two-color fluorescence imaging of synaptic vesicles and optical setup for measuring fluorescence polarization anisotropy of individual vesicles. (A) Two-color imaging of synaptic vesicles (SVs): left column (panels 1, 4, 7) are SVs with green fluorescence from loaded Oregon Green; middle column (panels 2, 5, 8) are SVs labeled with red fluorescent antibodies specific to the SV protein SV65; right column (panels 3, 6, 9) are overlays of the green and red images. (B) Schematic of microscope setup used to determine the steady-state anisotropy of individual SVs; the fluorescent spots in the inset are individual SVs loaded with Oregon Green.

Fluorescence anisotropy measurements. Figure 2.1 B shows the microscope setup we used to measure the fluorescence anisotropy of OG in SVs. Fig. 2.2 shows the measured anisotropy of OG in 752 SVs empty of neurotransmitters from wild-type (WT) mice (A), 794 empty SVs from SV2 DKO mice (B), and 781 SVs from WT mice loaded with the neurotransmitter glutamate (C). The mean anisotropies of the SVs were 0.146 ± 0.074, 0.115 ± 0.066, and 0.119 ± 0.051 for empty WT, empty SV2 DKO, and glutamate-loaded WT SVs, respectively; the uncertainties represent the standard deviation. The broad distribution of measured anisotropies is likely caused by a combination of factors, such as the heterogeneity inherently present in the SVs, which came from a whole mouse brain preparation, or nanoscopic imperfections in the glass surface that would lead to local changes in the polarization of the light around each SV. However, there is still a statistically significant difference between the WT anisotropy and the anisotropy of DKO or glutamate loaded SVs ($p<0.05$). When comparing SV2 DKO and glutamate loaded SVs, the difference was not found to be statistically significant. Another concern is that the use of high numerical aperture objective (NA = 1.3) can lead to uneven polarization across the field of view and also cause polarization mixing; however, we have studied this and did not find this potential issue to be a problem (see next section).

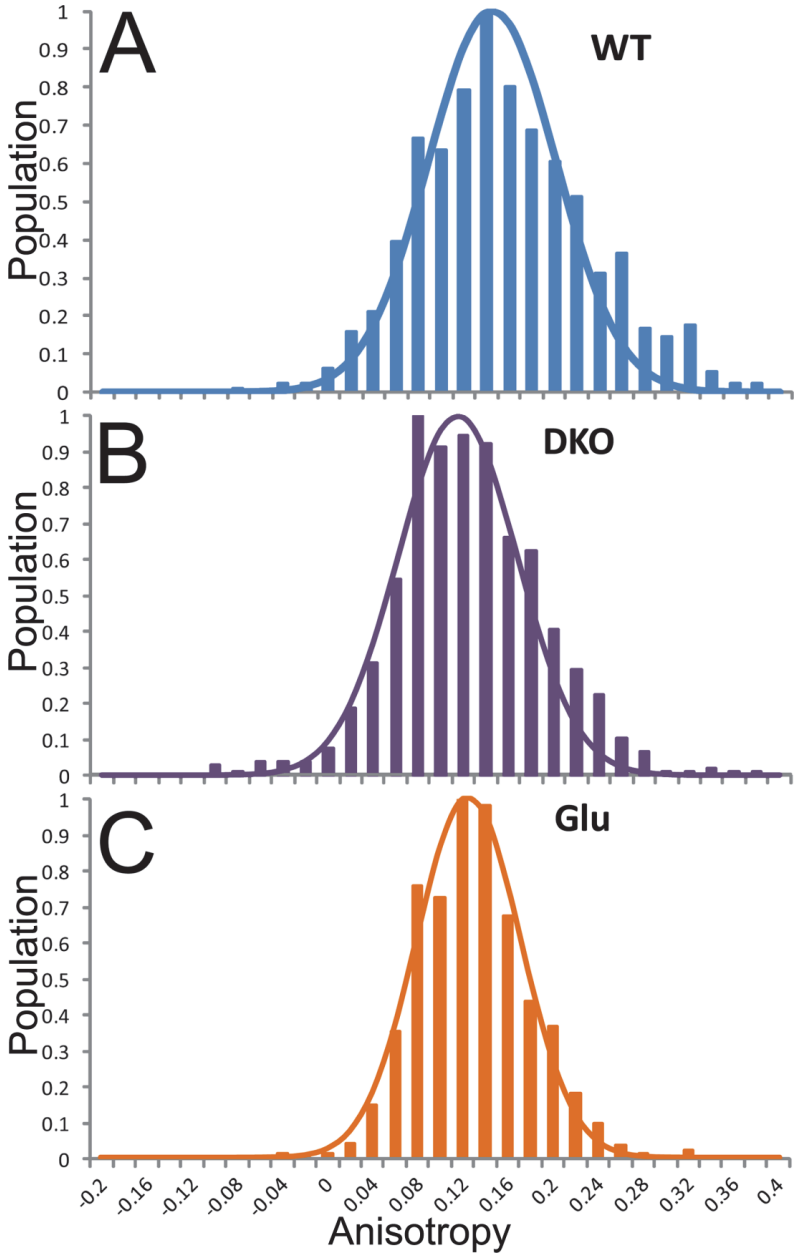

Figure 2.2. Histograms of the measured anisotropies of three different sets of synaptic vesicles (SVs). (A) Empty SVs from wild type (WT) SVs have a mean anisotropy of 0.146 (n=752). (B) Empty SVs from SV2 double knock-out (DKO) mice have a mean anisotropy of 0.115 (n=794). (C) WT SVs loaded with the neurotransmitter glutamate (Glu) have a mean anisotropy of 0.119 (n=781).

Effect of high NA on polarization. Out of concern for the effect of high NA upon fluorescence polarization measurements (14), we investigated the possible effect that this would have on our results by comparing the measured anisotropy of OG in various glycerol/water solutions obtained with a 0.40 NA (20× magnification) objective and the 1.3 NA (100 × magnification) objective used for measuring the anisotropy of SVs. The measured anisotropy between the two objectives was not significantly different (data not shown), so the effect of NA on polarization anisotropy was assumed to be small.

Assay for verifying loading of glutamate into synaptic vesicles. In the absence of ATP, glutamate leaks out of SVs (5). As a result, the SVs we isolated and purified from whole brain were empty and devoid of glutamate. However, incubating SVs in a loading buffer that contains ATP and glutamate will refill the SVs with glutamate (5). To verify that the glutamate loaded SVs were indeed refilled with neurotransmitter we used a fluorescence assay for glutamate:

$$\text{Glutamate} + \text{NADP}^+ \xrightarrow{\text{L-GDH}} \text{2-oxoglutarate} + \text{NH}_4^+ + \text{NADPH}$$

Here, glutamate dehydrogenase (GDH) converts glutamate and $NADP^+$ to 2-oxoglutarate and NADPH. Therefore, the presence of glutamate could be verified by the conversion of $NADP^+$ to NADPH, because fluorescence of $NADP^+$ peaks at λ_{em} 400 nm while NADPH has a fluorescence peak at 460 nm.

Glutamate was loaded into SVs by incubating purified SVs with glutamate in the buffer described in methods. Figure 2.3 shows the result of our fluorescence assay for glutamate loaded SVs. Without ATP, glutamate does not load into SVs, so SVs

incubated in glutamate loading buffer without ATP was used for the negative control. The reduced NADPH peak in the negative control shows there was little glutamate present in the vesicle without active transport. However, there seems to be a very small amount of NADPH fluorescence, likely because some extra-vesicular glutamate that was present in high concentrations in the loading solution was not removed or adsorbed to the SVs. The positive control contained glutamate diluted to a final concentration of 5 μM in a SV-free solution. When the glutamate loaded SVs were disrupted through sonication to test for the presence of glutamate, their contents were diluted by several orders of magnitude by the extravesicular assay buffer. Because of this large dilution the detected NADPH fluorescence was weak, although it still clearly demonstrated glutamate loading into SVs.

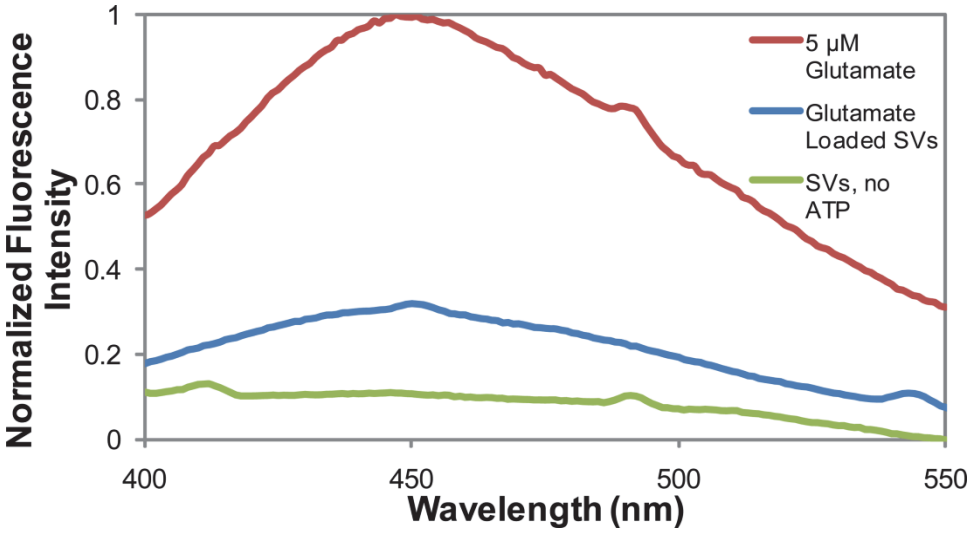

Figure 2.3. Fluorescence assay for verifying loading of glutamate into synaptic vesicles. In the presence of glutamate, glutamate dehydrogenase converts $NADP^+$ into NADPH, which has a broad fluorescent peak with a center wavelength of ~ 450 nm. In this assay, the amount of glutamate present in the sample is correlated with the intensity of the NADPH fluorescence. Red curve is the positive control, which had 5 µM of glutamate in solution. Blue curve shows the presence of glutamate in SVs loaded with glutamate using a loading buffer that contained glutamate and ATP. Because of the extremely small volume of SVs, there was a large dilution of glutamate when the intra-vesicular glutamate was released into solution following the lysis of SVs. Green curve is the negative control, which was identical to the procedure and solution used for the blue curve, but without ATP, which is needed for active transport of glutamate from the extra-vesicular solution into the vesicles during loading.

Measurements of fluorescence lifetime of OG in synaptic vesicles. To quantify the rotational viscosity of the vesicle lumen based on the fluorescence polarization anisotropy of OG and the Perrin equation, the fluorescence lifetime of OG must also be determined. Because fluorescence lifetime can change depending on the immediate environment experienced by the dye molecules, it was necessary to measure the fluorescence lifetime of OG after it had been loaded into the SVs. We carried out this

experiment by loading the SVs with OG, as described previously, and then separating the SVs from the free OG in solution by pelleting the SVs via centrifugation. The OG loaded SV pellet was thoroughly rinsed and then re-suspended in a buffered solution prior to measurement. For glutamate loaded SVs, an additional glutamate loading step followed the loading of SVs with OG.

Figure 2.4 shows our measured fluorescence lifetime of OG in WT empty SVs, SV2 DKO empty SVs, and WT glutamate loaded SVs. The fluorescence lifetime of OG did not vary greatly between each of the samples, which indicated there was not a significant amount of self-quenching or fluorescence depolarization due to effects like HOMO-FRET (Förster resonance energy transfer) after OG was loaded into SVs. Additionally, the fits to the fluorescence lifetimes were not improved by including additional lifetime components. This fact suggests that the OG loaded within the SVs was homogeneous, as OG molecules adsorbed to the membrane surface of SVs or stacked on top of one another should have quite different fluorescence lifetimes. The presence of only one resolved fluorescence lifetime, along with experiments conducted in (11) and the specificity of OG loading at pH 5.1 all indicate that the OG is freely rotating in the SV lumen instead of being absorbed to the SV membrane.

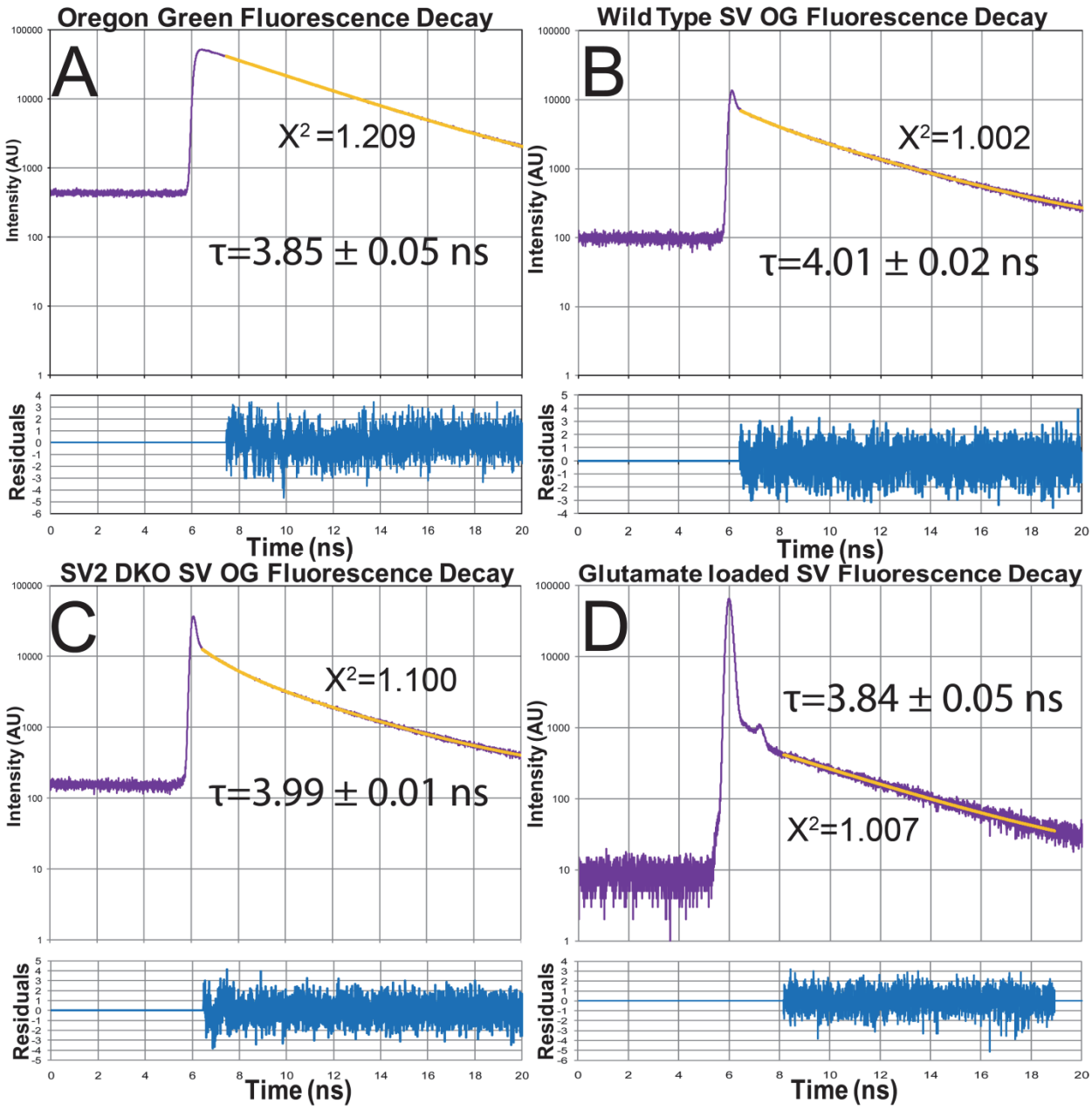

Figure 2.4. Fluorescence lifetimes of Oregon Green (OG). Fluorescence decay curve of (A) free OG in solution, (B) OG in empty wild type synaptic vesicles, (C) OG in empty SV2 double knock-out (DKO) synaptic vesicles, and (D) OG in wild-type synaptic vesicles that have been filled with glutamate. The additional peaks in panels C and D are from the instrument response function of the detector. They are more prominent here than in the other panels because of low fluorescence signal from OG. Each graph also displays the chi-squared values for the single exponential lifetime fittings and below each

of the decay curves is a plot of the residuals from fitting the curves to a single exponential decay function.

Rotational viscosity in synaptic vesicles. To determine the rotational viscosity within synaptic vesicles, we first had to obtain a calibration curve using the anisotropies and lifetimes of OG. For this, we added OG to solutions containing progressive ratios of glycerol:water, and their anisotropies were measured in order to extrapolate to the anisotropy of OG in a solution with infinite viscosity, that is, the equivalent of a stationary OG molecule as shown in the inset graph in figure 2.5. We found the maximum anisotropy of OG, r_0, to be 0.346 ± 0.003, which is close to previous measurements for different adducts of OG (15). Figure 2.5 plots the theoretically calculated rotational viscosities and the experimentally measured values, which match well with the theoretically calculated viscosities as determined using a method developed by Cheng et al. (16).

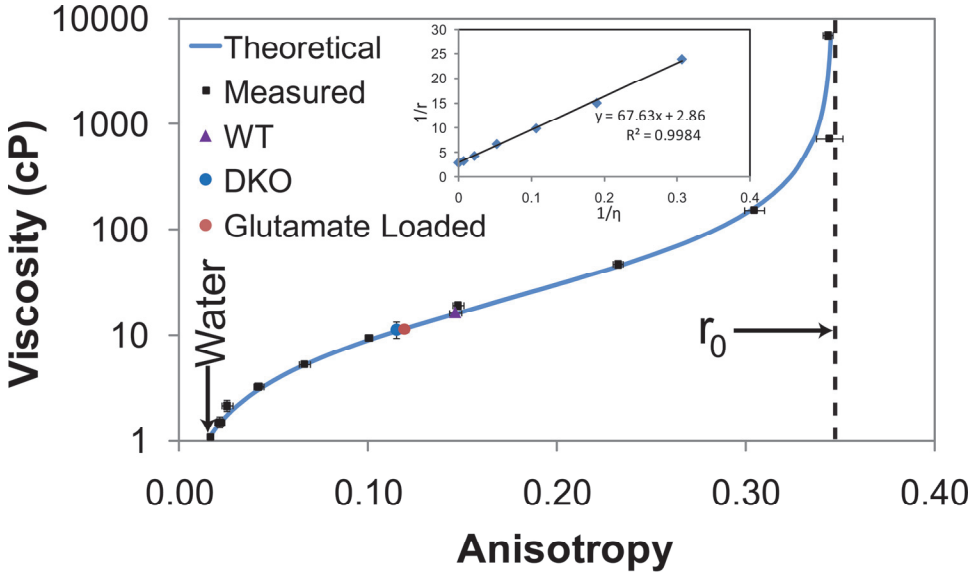

Figure 2.5. Measurements of rotational viscosity. The blue line represents theoretically calculated rotational viscosities; the dots with error bars are experimental values we measured using our setup for OG in aqueous solution containing varying amounts of glycerol. Wild Type (WT) empty vesicles, SV2 double knock-out (DKO) empty vesicles, and wild-type glutamate loaded vesicles were placed on their respective positions on the curve based on their average anisotropies and measured fluorescence lifetimes. Inset is the Perrin plot used to extrapolate r_0, the absolute anisotropy of OG.

With this calibration curve, we were able to determine the mean viscosity within each of the three types of synaptic vesicles that we prepared. Empty SVs from wild-type mice had the highest viscosity, while both empty SV2 DKO vesicles and wild type SVs filled with glutamate had significantly lower viscosities. Table 1 summarizes the data.

	WT	SV2 DKO	Glutamate Loaded	OG in Water
Mean Anisotropy	**0.146 ± 0.003**	**0.115 ± 0.002**	**0.119 ± 0.002**	**0.0162 ± 0.0009**
OG Fluorescence Lifetime (ns)	**4.01 ± 0.02 (χ^2=1.002)**	**3.99 ± 0.01 (χ^2=1.100)**	**3.84 ± 0.05 (χ^2=1.007)**	**3.85 ± 0.05 (χ^2=1.209)**
Viscosity (cP)	**16.49 ± 0.12**	**11.21 ± 0.12**	**11.40 ± 0.65**	**1.08 ± 0.06**
Rotational Correlation Time (ns)	**2.93 ± 0.02**	**1.99 ± 0.02**	**2.01 ± 0.11**	**0.19 ± 0.01**

Table 2.1. Data of merit WT: empty synaptic vesicles from wild-type mice (n=752); SV2 DKO: empty synaptic vesicles from SV2 Double Knock Out mice (n=794); Glutamate Loaded: synaptic vesicles from wild-type mice filled with glutamate (n=781); OG in Water: Oregon Green in water (n=3). The SV anisotropy values reported in the table are the calculated standard error of the mean for each SV population. The standard deviations for WT, SV2 DKO, and glutamate loaded SVs are ±0.074, ±0.066, and ±0.051, respectively. Despite the large variations in each SV sample, there is a highly statistically significant difference between the measured viscosities of WT SVs and SV2 DKO SVs ($t=8.69$, $p<0.0001$) and between WT SVs and glutamate loaded SVs ($t=8.28$, $p<0.0001$).

The high viscosity (16.5 cP) measured inside wild-type empty vesicles reflects both the minuteness of the enclosed volume (~ 2×10^{-20} L) as well as the tight packing of the intra-vesicular volume by the luminal domains of SV proteins. In particular, the heavily glycosylated luminal domains of SV2 is an important contributor to the viscous environment in SVs. Takamori et al. (2) estimated that on average, each SV contains 600 transmembrane domains; we recently counted each SV contains exactly 5 copies of SV2 (17), which represents a relatively small fraction of proteins present on SVs. Yet, SVs lacking SV2 have a significantly lower viscosity of 11.2 cP, which confirms SV2 is an important determinant of intra-vesicular viscosity.

We also found empty vesicles had higher viscosity on average than vesicles filled with glutamate. This finding, although may seem unexpected at first because the intra-vesicular space should be more packed with molecules while filled with glutamate, is actually quite consistent with our recent report that SVs loaded with glutamate double their volume in comparison with empty SVs (5).

2.4 CONCLUSIONS

In conclusion, we note a significant difference in rotational viscosity between empty wild type and DKO synaptic vesicles as well as between wild-type empty versus glutamate-loaded vesicles. Our result indicates that the heavily glycosylated intravesicular domains of SV2 is a significant determinant of the rotational viscosity and local environment within the vesicle lumen. Additionally, our finding that empty vesicles are actually more viscous than glutamate-filled vesicles supports our previous report that synaptic vesicles do greatly expand in volume upon loading with neurotransmitters. Despite the small size (~ 40nm in diameter) and volume (~ ~ 2×10^{-20} L) defined by single synaptic vesicles, this paper shows it is possible to determine the rotational viscosity within this tiny volume and thus represents the smallest enclosed volume in which rotational measurement has been measured thus far.

REFERENCES

1. Südhof, T. C. 2004. The Synaptic Vesicle Cycle. *Annu. Rev. Neurosci*. 27:509-547.
2. Takamori, S., M. Holt, K. Stenius, E. A. Lemke, M. Grønborg, D. Riedel, H. Urlaub, S. Schenck, B. Brügger, P. Ringler, S. A. Müller, B. Rammner, F. Gräter, J. S. Hub, B. L. De Groot, G. Mieskes, Y. Moriyama, J. Klingauf, H. Grubmüller, J. Heuser, F. Wieland, and R. Jahn. 2006. Molecular Anatomy of a Trafficking Organelle. *Cell*. 127:831-846.
3. Liu, Y., and R. H. Edwards. 1997. The Role of Vesicular Transport Proteins in Synaptic Transmission and Neural Degeneration. *Annu. Rev. Neurosci*. 20:125-156.
4. Reigada, D., I. Díez-Pérez, P. Gorostiza, A. Verdaguer, I. Gómez de Aranda, O. Pineda, J. Vilarrasa, J. Marsal, J. Blasi, J. Aleu, and C. Solsona. 2003. Control of neurotransmitter release by an internal gel matrix in synaptic vesicles. *Proc. Natl. Acad. Sci. USA*. 100:3485-3490.
5. Budzinski, K. L., R. W. Allen, B. S. Fujimoto, P. Kensel-Hammes, D. M. Belnap, S. M. Bajjalieh, and D. T. Chiu. 2009. Large Structural Change in Isolated Synaptic Vesicles upon Loading with Neuro-transmitter. *Biophys. J.* 97:2577-2584.
6. Buckley, K., and R. B. Kelly. 1985. Identification of a Transmembrane Glycoprotein Specific for Secretory Vesicles of Neural and Endocrine Cells. *J. Cell Biol*.100:1284-1294.
7. Crowder, K. M., J. M. Gunther, T. A. Jones, B. D. Hale, H. Z. Zhang, M. R. Peterson, R. H. Scheller, C. Chavkin, and S. M. Bajjalieh. 1999. Abnormal neurotransmission in mice lacking synaptic vesicle protein 2A. *Proc. Natl. Acad. Sci. USA*. 96:15268-15273.
8. Xu, T., and S. M. Bajjalieh. 2001. SV2 modulates the size of the readily releasable pool of secretory vesicles. *Nat. Cell Biol.* 3:691-698.
9. Lynch, B. A., N. Lambeng, K. Nocka, P. Kensel-Hammes, S. M. Bajjalieh, A. Matagne, and B. Fuks. 2004. The synapticvesicle protein SV2A is the binding site for the antiepileptic drug levetiracetam. *Proc. Natl. Acad. Sci. USA*. 101:9861-9866.
10. Dong, M., F. Yeh, W. H. Tepp, C. Dean, E. A. Johnson, R. Janz, and E. R. Chapman. 2006. SV2 Is the Protein Receptor for Botulinum Neurotoxin A. *Science*. 312:592-596.
11. Allen, P. B., and D. T. Chiu. 2008. Alzheimer's disease protein Aβ1-42 does not disrupt isolated synaptic vesicles. *Biochim. Biophys. Acta*. 1782:326-334.
12. Jameson, D. M., and J. A. Ross. 2010. Fluorescence Polarization/Anisotropy in Diagnostics and Imaging. *Chem. Rev*. 110:2685-2708.
13. Lakowicz, J. R. 2008. Principles of Fluorescence Spectroscopy. Springer Science & Business Media, NY.
14. Axelrod, D. 1979. Carbocyanine Dye Orientation in Red Cell Membrane Studied by Microscopic Fluorescence Polarization. *Biophys. J.* 26:557-574.
15. Rusinova, E., V. Tretyachenko-Ladokhina, O. E. Vele, D. F. Senear, and J. B. Alexander Ross. 2002. Alexa and Oregon Green dyes as fluorescence anisotropy probes for measuring protein-protein and protein-nucleic acid interactions. *Anal. Biochem.* 308:18-25.
16. Cheng, N-S. 2008. Formula for the Viscosity of a Glycerol-Water Mixture. *Ind. Eng. Chem. Res.* 47:3285-3288.
17. Mutch, S. A., P. Kensel-Hammes, J. C. Gadd, B. S. Fujimoto, R. W. Allen, P. G. Schiro, R. M. Lorenz, C. L. Kuyper, J. S. Kuo, S. M. Bajjalieh, and D. T. Chiu. 2011. Protein Quantification at the Single Vesicle Level Reveals a Subset of Synaptic Vesicle Proteins Are Trafficked with High Precision. *J. Neurosci* 31:1461-1470.

Chapter 3: Semiconducting Polymer Nanoparticles as Polarization-sensitive Fluorescent Probes for the Measurement of the Orientation and Movement of Proteins

3.1 INTRODUCTION

Semiconducting polymer nanoparticles offer many advantages as fluorescent tags.[1] They are bright[2], emitting enough photons to be tracked with nanometer accuracy.[3] They can be made easily using the nanoprecipitation method from a wide range of fluorescent polymers[4,5], so that the absorption and emission spectra can be tailored to the specific application.[6] The small size and close packing of polymers allow for efficient energy transfer to doped dyes. [7] The nanoparticles can possess flexible surface chemistry and are easily functionalized with antibodies and other proteins[7–10] to bind a wide array of targets with a high degree of specificity. They can also be incorporated with other nanoparticles, such as quantum dots or gold or iron nanoparticles.[11] A variety of the polymers used in semiconducting nanoparticle formation have been shown to be biocompatible.[12]

Electronically excited conjugated polymers in nanoparticles undergo excited energy transfer (EET) along the backbone[13] and transfer absorbed energy to segments where light emission takes place.[14] EET happens from local regions of higher excitation energy to regions of lower energy where emission is preferred.[15-17] By blending fluorescent conjugated polymers at very low mass ratios with matrix polymers, we describe in this communication fluorescent nanoparticles that take advantage of the EET

within conjugated polymers. The fast EET along a short conjugated polymer backbone results in polymer nanoparticles that have high fluorescence polarization anisotropy. By monitoring the changes in a nanoparticle's polarized fluorescence intensity, changes in nanoparticle position can be inferred. By attaching the polymer nanoparticles to a protein of interest and observing the change in intensity of polarized light as a polymer nanoparticle moves, change in protein orientation as well as spatial information can be obtained simultaneously using the same fluorescent probe. We demonstrate the practical application of our bright, polarization-sensitive protein probes by monitoring the rotation of microtubules as they precess across a kinesin-coated surface.

We have used the nanoprecipitation method to generate conjugated polymer nanoparticles that were bright and showed intensity variation based on their orientation and the polarization of exciting light. The polymer nanoparticles' biocompatibility, chemical composition flexibility, and small size (7.46 nm) can make them useful as chemical probes for monitoring changes in protein orientation without significantly interfering in their function.

3.2 EXPERIMENTAL

Materials. Poly[(9,9-dioctylfluorenyl-2,7-diyl)-alt-co-(1,4-benzo-(2,1',3)-thiadiazole)] (PFBT, 10 kDa MW, polydispersity index (PDI) 2.3) was purchased from American Dye Source, Inc. (Quebec, Canada). Polystyrene-graft-poly(ethylene oxide) functionalized with carboxyl groups (PS-PEG-COOH, main chain MW 8,500, graft chain MW 1,200, total chain MW 21,700, PDI 1.25) was purchased from Polymer Source Inc

(Quebec, Canada). Dimethyl sulfoxide (DMSO), casein, adenosine 5'-triphosphate magnesium salt (MgATP), 4-(2-Hydroxyethyl)piperazine-1-ethanesulfonic acid, N-(2-Hydroxyethyl)piperazine-N′-(2-ethanesulfonic acid) (HEPES), (3-aminopropyl) triethoxysilane (APTES), poly(ethylene glycol) (PEG), and tetrahydrofuran (THF) were purchased from Sigma-Aldrich (St. Louis, MO). 1-ethyl-3-(3-dimethylaminopropyl)carbodiimide) was purchased from Invitrogen (Carlsbad, CA). 30% Hydrogen peroxide was purchased from JT Baker (Mansfield, MA). Ultrapure water (Milli-Q) was produced by a Milli-Q water production unit; this production unit and ammonium hydroxide were purchased from EMD Millipore (Billerica, MA). Tubulin protein, biotinylated tubulin, fluorescent HiLyte 488 tubulin, paclitaxel ("Taxol"), guanosine-5'- triphosphate (GTP), and General Tubulin Buffer (GTB) were purchased from Cytoskeleton Inc. (Denver, CO). Full length kinesin motor proteins of two varieties, fruit fly kinesin and *Escherichia coli*, were kindly provided by the Wordeman lab at the University of Washington department of physiology and biophysics. All chemicals were used as-is unless stated otherwise.

P70 Polymer synthesis. The copolymer was synthesized by grafting hydrophobic dodecylamine onto the hydrophilic poly(isobutylene-alt-maleic anhydride) (Mw~6,000) backbone through spontaneous amide linkage, which converts one maleic anhydride into one corresponding amide and one free carboxylic acid. Typically, 0.5 g (0.083 mmol) of poly(isobutylene-alt-maleic anhydride) was dispersed in 20 mL of anhydrous THF in a 100-mL round flask. 0.43 g (2.32 mmol) dodecylamine dissolved in 40 mL of anhydrous THF was quickly injected to the polymer solution and kept at 60 °C

with vigorous stirring. After 3 hours, the reaction mixture was concentrated to one third of the original volume under a reduced pressure. The concentrated solution was further refluxed overnight at 60 °C. The solvent was then slowly evaporated until the polymer was completely dry to obtain a pale yellow solid. The final product yield is ~0.88 g, 95%. ^{1}H NMR (500 MHz, $CDCl_3$): δ = 4.368-4.339 (br s, 2H), 3.74 (s, 2H), 2.516-2.483 (br s, 2H), 2.282-2.251 (br s, 2H), 1.848 (s, 2H), 1.264 (s, 22H), 0.879 (s, 9H).

Semiconducting Polymer Nanoparticle Formation. Polymer nanoparticles were formed by a nanoprecipitation technique. THF solutions with 20 μL of 10 mg/mL P70, 25 μL of 10 mg/mL PS-PEG-COOH, and 1 μL of 10 mg/mL PFBT were mixed with 5 mL of THF and the resulting solution was sonicated for 1 minute. Following sonication, the THF solution was quickly added to 10 mL of Milli-Q water under high sonication power. The polymer is insoluble in water and quickly formed polymer nanoparticles. The THF was then removed by heating the solution to 85 °C and bubbling nitrogen gas through the solution for 2 hours. Following removal of THF, the polymer dots were filtered through a 0.2-μm filter.

Polymer Dot Bioconjugation. Polymer nanoparticles were covalently bound to streptavidin in order to provide a convenient way to link nanoparticles with other biomolecules or structures of interest. 4 mL of nanoparticle solution with 0.1% PEG was mixed with 240 μL of streptavidin solution (1 mg/mL), and then 80 μL of freshly prepared EDC (5 mg/mL) was added to the solution. This was mixed for 4 hours by magnetic stirring at room temperature. After 4 hours, amine-terminated PEG was added along with an additional 80 μL of EDC in order to cap any remaining carboxylic acid

groups on the surface of the polymer dots and to reduce nonspecific binding. The reaction was allowed to continue for another 2 hours and then quenched with 80 μL of a 10 wt% BSA solution. The polymer dots were then concentrated using a 100,000 MW cut-off centrifuge tube and purified on a size-exclusion column. The resulting streptavidin-and-PEG-functionalized polymer dots are stable for several months if refrigerated at 4 °C.

Microtubule Preparation. Microtubules were polymerized from tubulin by mixing 10 μL GTB with 9 μL of 10 mg/mL tubulin, 1 μL 10 mg/mL biotinylated tubulin, 2 μL anhydrous DMSO, and 0.5 μL GTP. The solution was placed in a 37 °C water bath and taxol was added to a final concentration of 2 μM, 20 μM, and 200 μM at 0, 10, and 20 minutes, respectively. Polymerization was continued for 60 minutes and the microtubules were shortened by pipetting the microtubule repeatedly before use. Fluorescently labeled microtubules, used as a control, were prepared by replacing the biotinylated tubulin with HiLyte 488 tubulin and polymerizing the tubulin as described above.

Microtubule Gliding Assay. All glass coverslips were cleaned by sonication for 30 minutes in a 2% Micro-90 solution, followed by thorough rinsing in Milli-Q waterand sonication for 30 minutes in Milli-Q water. The glass was then boiled in a 3:2:1 solution of Milli-Q:NH_4OH:H_2O_2 for 60 minutes, followed by thorough rinsing with Milli-Q water before use. A channel with the approximate dimensions of 2.5 cm × 1 cm × 1 μm, was created using a clean glass slide attached to a 1” coverslip using double-sided sticky tape. Gliding microtubules with attached polymer dots were visualized using a slightly modified technique previously described by Wang et al.[25] A series of five solutions, 10

μL each, were introduced to the channel and allowed to sit for 5 minutes after their introduction. Solution 1 contained GTB with 0.5 mg/mL casein. Solution 2 contained GTB with 0.2 mg/mL casein, 0.3 mM MgATP, and kinesin. Solution 3 contained GTB with 0.5 mg/mL casein, 0.3 mM MgATP, 10 μM Taxol, and 0.05 μL of the microtubule solution. Solution 4 contained GTB with 0.5 mg/mL casein, 0.3 mM MgATP, 10 μM Taxol, and 50 pM functionalized polymer dots. Solution 5 contained GTB with 0.5 mg/mL casein, 1.5 mM MgATP, 10 μM Taxol, and an oxygen scavenging system (50 μg/mL glucose oxidase, 4μg/mL catalase, 1% glucose, and 0.1% β-mercaptoethanol). The final solution was introduced three times to flush out the free polymer nanoparticles.

Optical Setup. Polarized wide field illumination was accomplished using best form spherical singlet lenses, 488 nm λ/2 waveplates, and polarizers (Thorlabs, Newton, NJ). Through careful placement of polarization optics, we achieved an $I_{\parallel}$:$I_{\perp}$ ratio of 100:1.The 488-nm dichroic mirror we used was chosen for its insensitivity to polarization for reflection and transmission. Fluorescence excitation came from a Sapphire 488-nm laser (Coherent, Santa Clara, CA). Excitation light was filtered out using a 500-nm longpass filter. Imaging was carried out using a TE-2000 microscope (Nikon, Melville, NY) and a 100× 1.3 numerical aperture objective. A home-built setup described previously (Zeigler et al)[19] was used to separate the orthogonally polarized fluorescence components, and the resulting pair of images were captured on two halves of the same Cascade 512b EMCCD camera (Photometrics, Tucson, AZ).

Observation of Individual Surface Bound Polymer Nanoparticles. Individual polymer nanoparticles were observed by applying very dilute (1 pM) solutions of polymer nanoparticles to (3-aminopropyl)triethoxysilane treated number 1 glass coverslips (Bellco, Vineland NJ). The coverslips were photoetched to assist in positioning the coverslip under bright-field illumination. After five minutes, the coverslips were rinsed with Milli-Q water, dried, and made in a channel as described previously. Polymer nanoparticles polarization sensitivity was demonstrated by filling the channel with water and inserting the channel into a rotating stage mounted on the microscope. The polymer nanoparticles were illuminated and stage was rotated manually to visualize the selectively polarized emission of individual polymer nanoparticles.

Characterization of Polymer Nanoparticles. All fluorescence spectra were taken in 20 mM HEPES buffer, pH 7.4, supplemented with 0.1% PEG. Quantum yield measurements were taken using a Hamamatsu absolute PL quantum yield measurement system (Hamamatsu, Shizuoka, Japan), excited at 450 nm with a xenon lamp. Fluorescence lifetime and time-resolved fluorescence anisotropy measurements were taken using a Pico Quant Fluo time 100 system and a 470 nm picosecond laser as per manufacturer's recommendation and analyzed using commercial Fluo Fit software (Picoquant GmbH, Berlin, Germany). Nanoparticle size and zeta potential were characterized using a Zetasizer Nano ZS (Malvern, Philadelphia, PA). Fluorescence spectra were taken using the Fluorolog-3 fluorospectrometer (HORIBA, JobinYvon, NJ). Fluorescence spectra were taken in 20 mM HEPES buffer, pH 7.4, with 0.1% PEG.

3.3 RESULTS AND DISCUSSION

Preparation of polymer nanoparticles. Figure 3.1 shows the strategy used for preparing polarization-sensitive fluorescent nanoparticles. Nanoprecipitation of the hydrophobic fluorescent polymer Poly[(9,9-dioctylfluorenyl-2,7-diyl)-alt-co-(1,4-benzo-(2,1',3)-thiadiazole)] (PFBT), along with matrix polymers P70 (see Scheme 1 for chemical formula) and polystyrene-graft-poly(ethylene oxide) functionalized with carboxyl groups (PS-PEG-COOH), formed small fluorescent nanoparticles with a mean diameter of 7.46 nm and a peak width of 1.46 nm. The polymers P70 and PS-PEG-COOH formed a hydrophilic shell and a hydrophobic core, which encapsulated the hydrophobic PFBT polymer. The absorption/emission spectra of the nanoparticles are shown in Figure 3.2A. The nanoparticles were functionalized with streptavidin in order to facilitate binding to biomolecules. Figure 3.2B shows the nanoparticles had a relatively low zeta potential of -28 mV in 20 mM HEPES buffer at pH 7.2. To prevent aggregation and nonspecific adsorption, they were also functionalized with polyethylene glycol (PEG). Dynamic light scattering (DLS) measurements show an increase in average polymer nanoparticle hydrodynamic diameter before and after bioconjugation from 7.46 nm to 12.07 nm with peak FWHM of 1.46 and 3.72 nm, respectively (Figure 3.2C and D**).** The resulting functionalized nanoparticles were found to be quite monodisperse and their size measurement remained stable for months at 4 °C. The size of polymer nanoparticles had been previously determined using transmission electron microscopy as well as DLS, and the results were shown to be comparable using either method.[7] The small size of polymer nanoparticles generated in this method is valuable for two reasons.

First, their small size allows them to bind to proteins with minimal influence on protein activity. Second, the small size improves labeling efficiency due to improved mass transfer properties compared to larger fluorescent tags like beads.

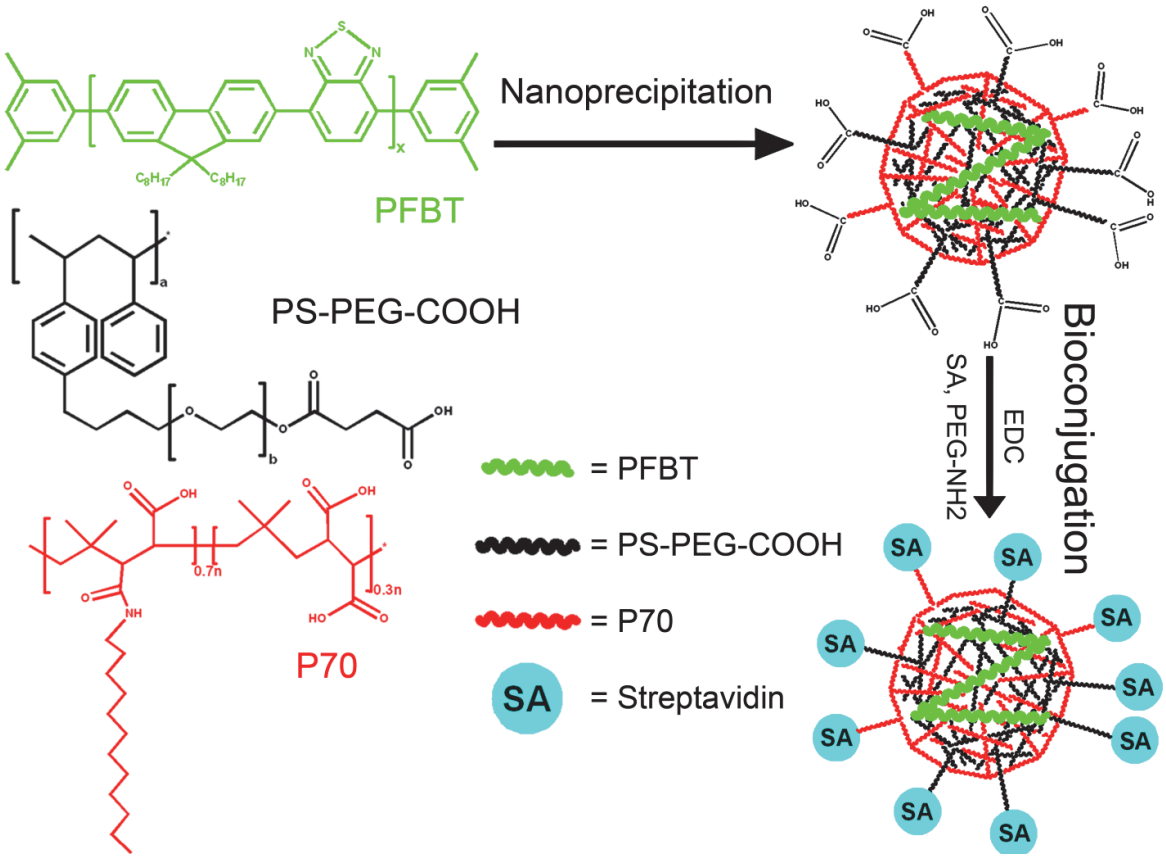

Figure 3.1. Schematic showing the preparation of polymer nanoparticle using nanoprecipitation and subsequent bioconjugation. Briefly, a THF solution of PFBT, the amphiphilic polymer PS-PEG-COOH and matrix polymer P70 is quickly injected into water under high sonication power to precipitate nanoparticles. The hydrophobic fluorescent PFBT is trapped within the core of the nanoparticle. The THF is removed by heating and bubbling with nitrogen. The nanoparticles are then bioconjugated to streptavidin and PEG.

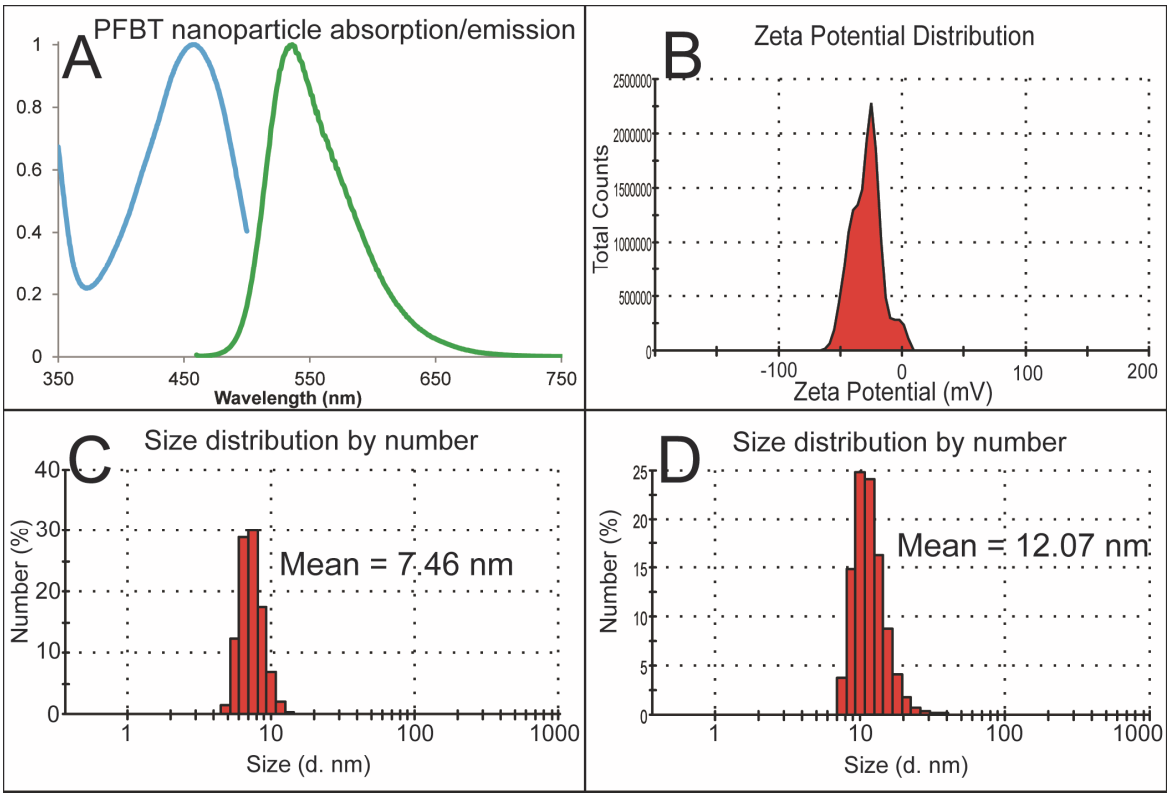

Figure 3.2. Bulk fluorescence and physical properties of polymer nanoparticles. (A) Absorption and emission spectra of polymer nanoparticles. (B) Zeta potential after bioconjugation and PEG functionalization. (C) Number-averaged nanoparticle hydrodynamic diameter before functionalization and (D) after functionalization with streptavidin and PEG. Despite the low zeta potential, polymer nanoparticle sizes remained stable for months and aggregation was not observed.

The mass of single polymer nanoparticles was estimated to be 200 kDA by differential centrifugation with a 1.5 M sucrose pillow. An 8-nm –diameter polymer nanoparticle with a density of 1.1 g/cm^3 would weigh approximately 200 kDa. With a mass ratio of fluorescent polymer of ~ 1-5% and a molecular weight of 10 kDa, each polymer nanoparticles contained around 1 PFBT chain per nanoparticle. This low mass ratio of fluorescent polymer differentiated these nanoparticles from previous work with Pdots, which generally contained at least 50% polymer by mass and often up to 100%. [1, 6]

Although the lower mass ratio of PFBT may decrease the brightness of the polymer nanoparticles in comparison to Pdots, it has other photophysical benefits. We have discussed previously the formation of PFBT Pdots, which contained 80% PFBT and exhibited a quantum yield of 0.3.[1, 2] In contrast, these polymer nanoparticles were found to have a quantum yield of 0.75 (Figure 3.3), which was even greater than the quantum yield of PFBT in THF solution. The high quantum yield was likely caused by the minimization of quenching by interchain aggregation [15,16] as well as reduced quenching of photoluminescence by oxygen[17] due to the presence of a polymer shell protecting the hydrophobic fluorescent polymer from the aqueous environment. The polymer nanoparticles were quite photostable, and their brightness was nearly identical to quantum dots when excited with 488-nm light (Figures 3.4 and 3.5). Also, these low mass ratio polymer nanoparticles had a high intensity dependence on the polarization of incident light.

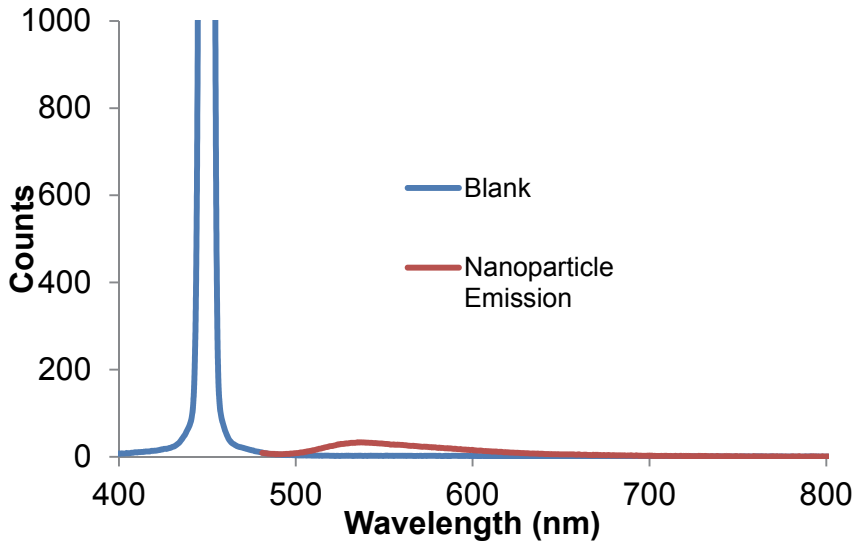

No.	Counts 439 - 460(nm)	Counts 483 - 868(nm)	QuantumYield
Blank	2.81×10^{7}	---	---
PFBT Nanoparticles	2.61×10^{7}	1.52×10^{6}	0.75

Figure 3.3. Quantum yield of polymer nanoparticles.

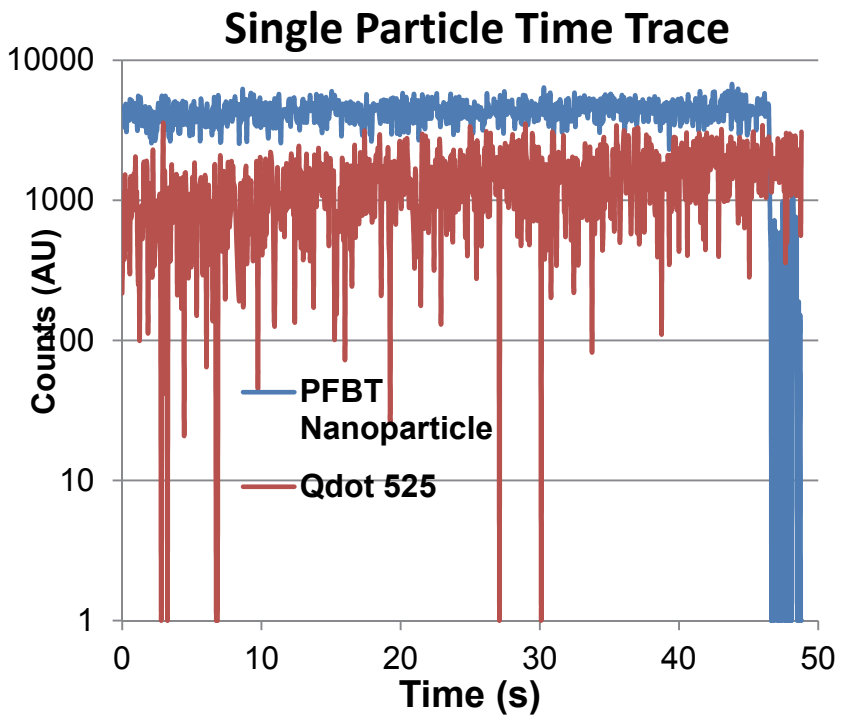

Figure 3.4. Intensity time trace of a single polymer nanoparticle and a single quantum dot. This PFBT nanoparticle was bound to a stationary microtubule and shows little blinking and a single photobleaching event. The nanoparticles used did show intermittent blinking when passively adsorbed to a glass coverslip, but this blinking was almost entirely extinguished when bioconjugated nanoparticles were bound to microtubules. The reason for this is not entirely clear. Although the brightness of this PFBT nanoparticle was higher than the quantum dot, single-particle brightness measurements show that they have comparable average brightness.

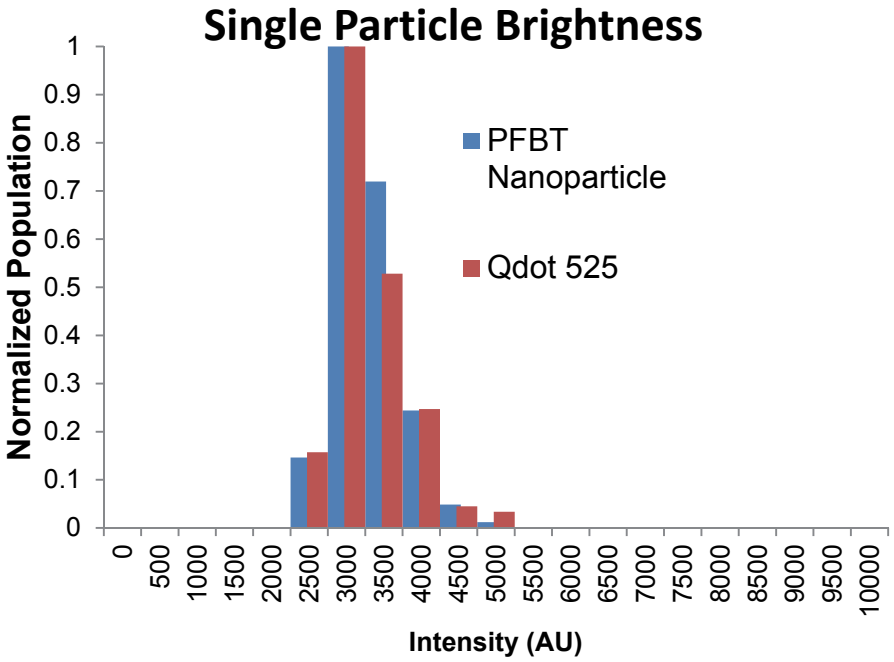

Figure 3.5. Single particle brightness histogram comparing polymer nanoparticles and Qdot 525. Mean brightness was 3035 ± 424 (n=178) and 3020 ± 492 (n=179) for polymer nanoparticles and 525 nm emission quantum dots, respectively.

Polarization sensitivity. The polymer nanoparticles showed a large intensity dependence on the polarization of light used for excitation. To demonstrate this, we used an optical setup with linearly polarized excitation. By using carefully positioned polarizers and λ/2 waveplates, we achieved $I_{\parallel}$:$I_{\perp}$ excitation polarization ratio of intensities of 100:1, measured after the objective. This polarized light selectively excites chromophores that have absorption dipoles aligned with the light; when the chromophores are confined to a specific orientation, the emitted light can also be polarized. [18] The emitted light was separated into its orthogonally polarized components, and the components were imaged onto an EMCCD camera. Information on the orientation changes of the polymer nanoparticles could be deduced from the change in intensity of the polarized components of the emitted light. The setup used for separating the emission into its orthogonal polarizations has been described previously. [19]

The fluorescence intensity dependence upon light polarization was monitored by two separate methods (Figure 3.6). In both methods, polymer nanoparticles were adsorbed to the surface of a cleaned, APTES-coated glass channel; then the channel was filled with Milli-Q water. In the first method, the excitation polarization remained fixed while the polymer nanoparticle sample was rotated manually using a rotation stage. The resulting anti-correlated intensity maxima and minima for the orthogonally polarized emitted light are shown in Figure 3.6B. The intensity of emission measured in $I_{\parallel}$ and $I_{\perp}$ channels as the stage rotated was not always anti-correlated; the relationship of the intensities of the two channels depended on the orientation at which the polymer nanoparticle adsorbed to the coverslip. The orientation of the emission dipole of each polymer nanoparticle was random, so the curves for $I_{\parallel}$ and $I_{\perp}$ could be correlated as in Figure 3.6C, anti-correlated, or in between correlated and anti-correlated. Although the maxima and minima were present, practical issues resulting from manual repositioning of the rotation stage somewhat distorted the curves. In the second method, a $\lambda/2$ waveplate placed in a rotating mount in the excitation path was moved while the sample remained stationary. The intensity of emitted light from a single polymer nanoparticle for $I_{\parallel}$ and $I_{\perp}$ is shown in Figure 3.6C. The emission from the polymer nanoparticle resembled what would be observed for a single, stationary fluorophore.

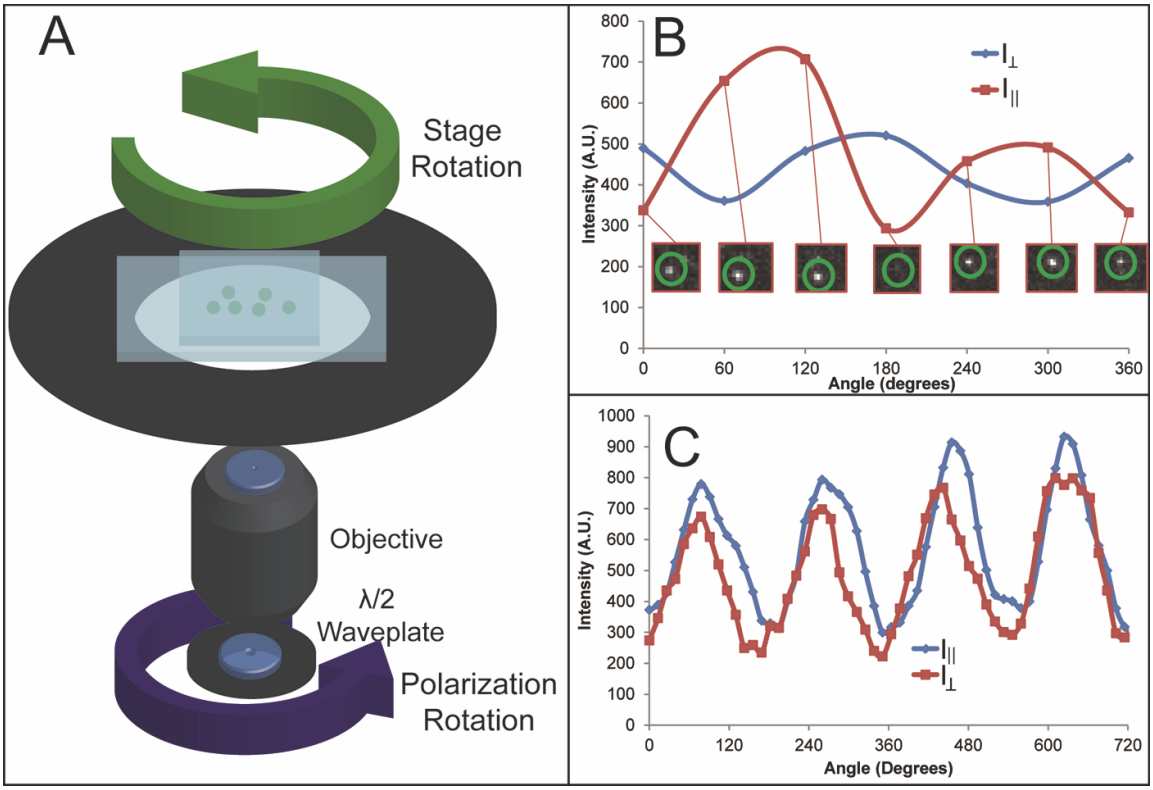

Figure 3.6. Polarization of individual polymer nanoparticles. (A) Schematic showing the microscope stage and polymer nanoparticles in a channel. The polarization excitation was changed by rotation of a λ/2 plate or the stage was rotated with constant polarization. (B) The plot shows the emitted light of a single polymer nanoparticle, separated into two channels of orthogonal polarization. The orientation of the polymer nanoparticle was changed with respect to excitation polarization by rotating the stage while the excitation polarization was held constant. The emission shows a strong dependence upon the orientation of the single polymer nanoparticle. Inset are images taken of a single nanoparticle upon stage rotation captured by the $I_{||}$ channel. (C) The plot shows the emitted light of a single polymer nanoparticle as the excitation polarization was rotated. The correlated intensity change in orthogonally polarized emission channels was what would be expected from a single emitting chromophore.

Figure 3.7A is a cartoon depicting EET within the polymer nanoparticle. The PFBT polymer absorbed photons aligned with its absorption dipole and the absorbed energy was quickly transferred to the lowest energy point on the chain. The chromophore that ultimately emitted a photon may or may not have had its dipole moment aligned with the absorption dipole. This means that for individual fluorescent

nanoparticles, the absorption and emission of the PFBT polymer can give information on changes in nanoparticle orientation. However, due to energy transfer, the excitation and emission polarizations may be random with respect to each other. Figure 3.7B is an overlay of the time-resolved anisotropy decay and the fluorescence lifetime decay of polymer nanoparticles in bulk aqueous solution. The high initial anisotropy of 0.36 may be due to emission from the initially excited chromophore, which was aligned with the polarized light and would be expected to be highly anisotropic. The subsequent decrease in bulk anisotropy would be caused by excitation energy transfer to a chromophore with a different emission dipole moment and no memory of the excitation polarization. Integration under the anisotropic decay curve revealed that 94% of photons were emitted after the lifetime of the anisotropic decay; presumably, a large majority of photons were emitted after excited energy transfer. Based on a hydrodynamic diameter of 12.07 nm, we estimated using the Perrin equation that the rotational correlation time of the polymer nanoparticles was 200 nanoseconds. The anisotropic decay lifetime of the polymer nanoparticles measured in bulk aqueous solution was 170 picoseconds, three orders of magnitude faster than the rotational correlation time and consistent with the timescale of EET.

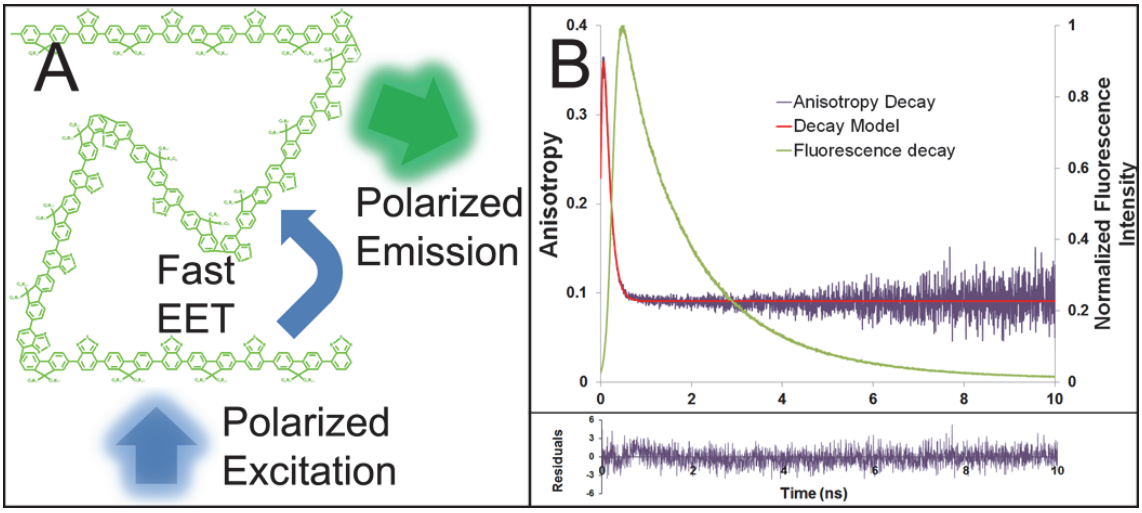

Figure 3.7. Energy transfer in polymer nanoparticles. The fluorescent PFBT polymer is held within the hydrophobic core of the polymer nanoparticle. Upon excitation with polarized light (A) intramolecular exciton transfer quickly directs fluorescence to chromophores within the polymer where fluorescent emission is favored, most likely due to a discontinuity in the polymer chain. In (B) a time-resolved fluorescence anisotropy decay (purple) is overlaid with the fluorescence lifetime decay of PFBT nanoparticles, showing that emission depolarization occurs more quickly than fluorescence decay. Depolarization also occurs much faster than the calculated rotational correlation time of a 10-nm-diameter particle in water. Although the emission is polarized, the direction of polarized emission is independent of excitation polarization and different for each nanoparticle.

Semiconducting polymer nanoparticles as detectors of microtubule orientation. The small size, optical stability, chemical flexibility, and polarization sensitivity of the polymer nanoparticles makes them good candidates for probes to detect orientation changes in proteins. Eukaryotic microtubules inside cells usually each contain 13 protofilaments comprised of repeating units of α and β tubulin; microtubules polymerized *in vitro* have been shown to consist of varying numbers of protofilaments. Variation away from 13 protofilaments per microtubule can create a periodic twist in the cylinder of the microtubule. [23–25] The motor protein kinesin precesses along the protofilaments axis in the microtubule, following along with any potential periodic twist

in the microtubule axis. In a microtubule gliding assay, we passively adsorbed kinesin onto a glass surface to drive microtubules labeled with polymer nanoparticles through a channel. As the microtubules were directed by kinesin, the periodicity of the microtubule twist could be visualized using fluorescence microscopy (Figure 3.8A).

The heavy chain of kinesin is approximately 70 nm long and the gliding assay was not inhibited by the presence of the 12-nm-diameter polymer nanoparticles. The periodicity of the microtubule twists was measured in this gliding assay using two different kinesin proteins: one fruit fly kinesin with a precession rate of 0.8 μm/s and *E. coli* kinesin with a precession rate of 1.2 μm/s. We measured the rate of precession of polymer-nanoparticle-labeled microtubules and microtubules containing fluorescent tubulin protein. The rates were the same for the fluorescently labeled and polymer-nanoparticle-labeled microtubules. The polymer nanoparticles did not appear to inhibit kinesin function. The histogram of the measured microtubule twist lengths are shown in Figure 3.8B, and the measured distributions in twist length remained consistent between the slower fruit fly and faster *E. coli* kinesin proteins. The twists were determined by the distance between local intensity maxima of polymer nanoparticle emission, and were not counted unless at least two consecutive periods of the same length were recorded between three local intensity maxima. Also, local intensity maxima and minima had to vary by at least 50%, representing a change in nanoparticle absorption/emission dipole orientation of approximately 0.75 radians over the course of the rotation. The observed numbers of rotating microtubules bound to fruit fly and *E. coli* kinesins were 131 and 62, respectively. Along with polymer nanoparticles that periodically showed bright and dark

emission, a significant number of nanoparticles showed continuous emission while bound to precessing microtubules. This could be due to the observation of microtubules made of 13 protofilaments which did not have a twist or the absorption/emission dipole of the nanoparticle aligned with the microtubule. The latter case was considered unlikely, as often times several polymer nanoparticles labeled a single microtubule and each microtubule with multiple labels either exhibited periodic or constant emission from all bound nanoparticles. We observed 171 nonrotating microtubules bound to the fruit fly kinesin and 69 nonrotating microtubules bound to E. coli kinesin. Figure 3.8C is a trace of a microtubule labeled with a single polymer nanoparticle, showing alternating bright and dark spots as the microtubule rotates.

The microtubules were polymerized with 10% biotinylated tubulin, which allowed strong binding between streptavidin-functionalized polymer nanoparticles and the microtubules. Because of the high density of biotinylated tubulin and the size of the polymer nanoparticles and tubulin units, it was likely that each polymer nanoparticle was bound to the microtubule by more than one biotin/streptavidin linkage. Virtually no fast, sporadic intensity fluctuations were visible that would be evidence for single biotin/streptavidin linkages or “the propeller effect” of polymer nanoparticles with flexible attachments to microtubules.

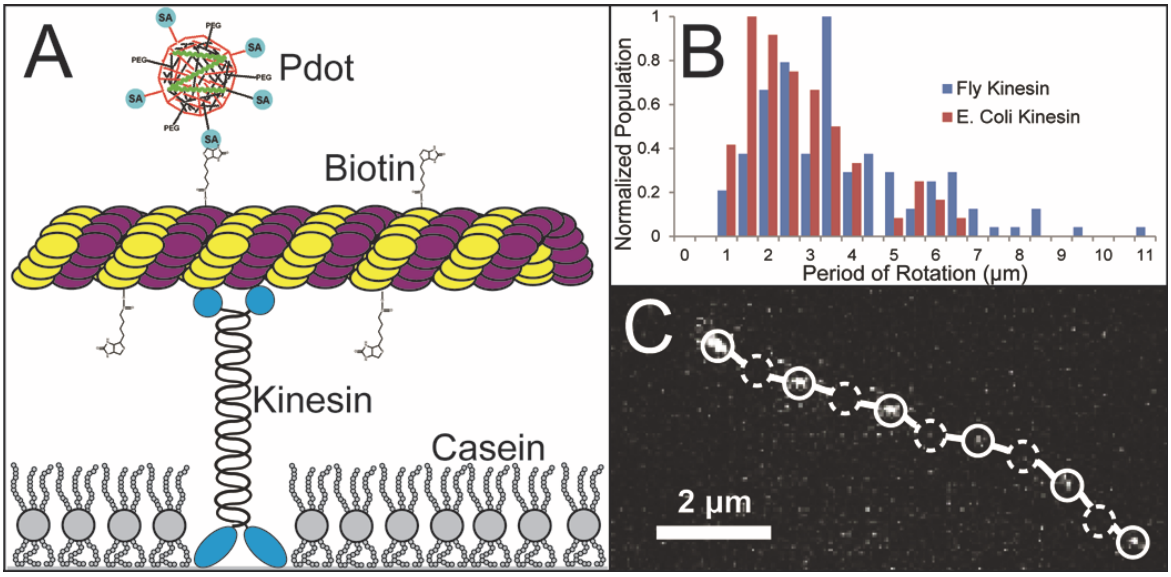

Figure 3.8. Polarization sensitive polymer nanoparticles used to detect microtubule rotation. (A) scheme showing a gliding microtubule moved by kinesin bound to a glass substrate. The polymer nanoparticles link to biotinylated tubulin within the microtubule. (B) measured microtubule periods of rotation when the microtubules are transported by two different forms of kinesin. There were 62 microtubules measured using *E. coli* kinesin and 131 measured using *Drosophilia* kinesin along with 64 and 148 nonrotating microtubules, respectively. (C) track of a single microtubule with a single bound polymer nanoparticle (open circles) show local intensity maxima while dashed circles indicate the location of local intensity minima.

3.4 CONCLUSION

We have made small semiconducting polymer nanoparticles with a low mass ratio of fluorescent polymer that have a strong sensitivity to polarization. EET from the chromophore that absorbs light to the energy minima of the chain was responsible for the high degree of emission polarization. This interchain energy transfer was highly efficient for two main reasons: First, the fluorescent polymer was a relatively short chain containing on average 20 monomers and made up a small mass percentage of the polymer nanoparticle, so the remaining polymer shell protected the excitation energy from FRET or quenching by oxygen. Second, the short chain length reduced the chances of multiple

excitations of chromophores within a polymer and subsequent singlet-singlet annihilation. We anticipate the bright and polarization sensitive probe described here will provide a useful tool for studying the rotational motions of biomolecules.

REFERENCES

1. Wu, C.; Chiu, D. T. Highly Fluorescent Semiconducting Polymer Dots for Biology and Medicine. Angewandte Chemie International Edition 2013, n/a–n/a.

2. Wu, C.; Schneider, T.; Zeigler, M.; Yu, J.; Schiro, P. G.; Burnham, D. R.; McNeill, J.; Chiu, D. T. Bioconjugation of Ultrabright Semiconducting Polymer Dots for Specific Cellular Targeting. J. Am. Chem. Soc. 2010, 132, 15410–15417.

3. Yu, J.; Wu, C.; Sahu, S. P.; Fernando, L. P.; Szymanski, C.; McNeill, J. Nanoscale 3D Tracking with Conjugated Polymer Nanoparticles. Journal of the American Chemical Society 2009, 131, 18410–18414.

4. Hashim, Z.; Howes, P.; Green, M. Luminescent Quantum-dot-sized Conjugated Polymer Nanoparticles-nanoparticle Formation in a Miniemulsion System. Journal of Materials Chemistry 2011, 21, 1797–1803.

5. Zhang, X.; Yu, J.; Wu, C.; Jin, Y.; Rong, Y.; Ye, F.; Chiu, D. T. Importance of Having Low-Density Functional Groups for Generating High-Performance Semiconducting Polymer Dots. ACS Nano 2012, 6, 5429–5439.

6. Rong, Y.; Wu, C.; Yu, J.; Zhang, X.; Ye, F.; Zeigler, M.; Gallina, M. E.; Wu, I.-C.; Zhang, Y.; Chan, Y.-H. et al. Multicolor Fluorescent Semiconducting Polymer Dots with Narrow Emissions and High Brightness. ACS Nano 2013, 7, 376–384.

7. Jin, Y.; Ye, F.; Zeigler, M.; Wu, C.; Chiu, D. T. Near-Infrared Fluorescent Dye-Doped Semiconducting Polymer Dots. ACS Nano 2011, 5, 1468–1475.

8. Wu, C.; Jin, Y.; Schneider, T.; Burnham, D. R.; Smith, P. B.; Chiu, D. T. Ultrabright and Bioorthogonal Labeling of Cellular Targets Using Semiconducting Polymer Dots and Click Chemistry. Angewandte Chemie International 2010, 49, 9346–9440.

9. Wu, C.; Hansen, S. J.; Hou, Q.; Yu, J.; Zeigler, M.; Jin, Y.; Burnham, D. R.; Mcneill, J. D.; Olson, J. M.; Chiu, D. T. Design of Highly Emissive Polymer Dot Bioconjugates for In Vivo Tumor Targeting. Angewandte Chemie 2011, 50, 3430–3434.

10. Petkau, K.; Kaeser, A.; Fischer, I.; Brunsveld, L.; Schenning, A. P. H. J. Pre- and Postfunctionalized Self-assembled Π-conjugated Fluorescent Organic Nanoparticles for Dual Targeting. J. Am. Chem. Soc. 2011, 133, 17063–17071.

11. Chan, Y.-H.; Ye, F.; Gallina, M. E.; Zhang, X.; Jin, Y.; Wu, I.-C.; Chiu, D. T. Hybrid Semiconducting Polymer Dot–Quantum Dot with Narrow-Band Emission, Near-Infrared Fluorescence, and High Brightness. J. Am. Chem. Soc. 2012, 134, 7309–7312.

12. Medina, C.; Santos-Martinez, M. J.; Radomski, A.; Corrigan, O. I.; Radomski, M. W. Nanoparticles: Pharmacological and Toxicological Significance. Br J Pharmacol 2007, 150, 552–558.

13. Zhou, Q.; Swager, T. M. Fluorescent Chemosensors Based on Energy Migration in Conjugated Polymers: The Molecular Wire Approach to Increased Sensitivity. Journal of the American Chemical Society 1995, 117, 12593–12602.

14. Klärner, G.; Lee, J.-I.; Davey, M. H.; Miller, R. D. Exciton Migration and Trapping in Copolymers Based on Dialkylfluorenes. Advanced Materials 1999, 11, 115–119.

15. Nguyen, T.-Q.; Doan, V.; Schwartz, B. J. Conjugated Polymer Aggregates in Solution: Control of Interchain Interactions. Journal of Chemical Physics 1999, 110, 4068–4078.

16. Jakubiak, R.; Collison, C. J.; Wan, W. C.; Rothberg, L. J. Aggregation Quenching of Luminescence in Electroluminescent Conjugated Polymers. Journal of Physical Chemistry A 1999, 103, 2394–2398.

17. Yu, J.; Hu, D.; Barbara, P. F. Unmasking Electronic Energy Transfer of Conjugated Polymers by Suppression of O2 Quenching. Science 2000, 289, 1327 –1330.

18. Lakowicz, J. R. Principles of Fluorescence Spectroscopy; 3rd ed.; Springer, 2006.

19. Zeigler, M. B.; Allen, P. B.; Chiu, D. T. Probing Rotational Visocsity in Synaptic Vesicles. Biophysical Journal 2011, 100, 2846–2851.

20. Lee, J.-I.; Zyung, T.; Miller, R. D.; Kim, Y. H.; Jeoung, S. C.; Kim, D. Photoluminescence Study on Exciton Migration and Trapping in a Copolymer Based on Poly(fluorene). Journal of Materials Chemistry 2000, 10, 1547–1550.

21. Huser, T.; Yan, M.; Rothberg, L. J. Single Chain Spectroscopy of Conformational Dependence of Conjugated Polymer Photophysics. Proc Natl Acad Sci USA 2000, 97, 11187–11191.

22. Schwartz, B. J.; Nguyen, T.-Q.; Wu, J.; Tolbert, S. H. Interchain and Intrachain Exciton Transport in Conjugated Polymers: Ultrafast Studies of Energy Migration in Aligned MEG-PPV/mesoporous Silica Composites. Synthetic Metals 2001, 116, 35–40.

23. Chrétien, D.; Wade, R. R. New Data on the Microtubule Surface Lattice. Biol Cell 1991, 71, 161–174.

24. Sanghamitra, R.; Meyerhöfer, E.; Milligan, R. A.; Howard, J. Kinesin Follows the Microtubule's Protofilament Axis. The Journal of Cell Biology 1993, 121, 1083–1093.

25. Wang, G.; Sun, W.; Luo, Y.; Fang, N. Resolving Rotational Motions of Nano-objects in Engineered Environments and Live Cells with Gold Nanorods and Differential Interference Contrast Microscopy. Journal of the American Chemical Society 2010, 132, 16417–16422.

Chapter 4: Laser Selection Significantly Affects Cell Viability Following Single-Cell Nanosurgery

4.1 INTRODUCTION

Lasers have long been used as tools for the manipulation of single cells. A laser with a Gaussian intensity profile, for example, will form a single-beam gradient trap (or optical tweezer) when focused through a high numerical aperture objective (1); optical tweezers have been used extensively for the manipulation of single cells, organelles, and micro/nanoparticles. Any cellular structure that is resolvable by light microscopy can be altered by laser ablation, allowing for improved spatial and temporal resolution over previous methods like micromanipulation (e.g. with micropipettes or microneedles) for altering cellular compositions. Optical manipulation also offers other benefits such as: high throughput, high reproducibility, and no direct physical contact with the cells which allows for a sterile environment. Laser ablation can cause disruption of the cell's cytoskeleton or organelles (2), facilitate *in vitro* fertilization by weakening of the oocyte's zona pellucida (3), ablation of plant cell walls for transfection (4), or to assist in patch clamping (5). Cellular membrane disruption also allows optical trapping of sub-cellular compartments for removal from the cell (6), or transient cell permeabilization for introduction of exogenous molecules into the cell (7-9). Visualization and surgery of subcellular components can be improved by the addition of photosensitizing dyes or GFP tagging (10). Addition of material can take place via plasma-mediated or mechanical delivery to multiple cells (11-13), or transient membrane disruption of a single cell (14-

17). Laser surgery has also been used on a larger scale for a variety of medical procedures or lysis of entire cells for single-cell characterization (18), the study of insect embryonic development (19), or for ablating single synapses to modify neural networks in C. *elegans* (20).

In the past years, we have been working to develop and apply optical techniques for single-cell nanosurgery, in which subcellular structures either are removed or introduced into a living mammalian cell in culture (6, 20, 21). In this procedure, a small portion of the cell membrane is disrupted; this disruption can occur via a variety of different laser-membrane interaction mechanisms that are determined primarily by the irradiance within the focal volume (22). The laser-membrane interaction can occur over a wide range of timescales and use a variety of lasers from fs to cw. The mechanism of optical disruption has been well studied in the literature (23-25), and can occur due to photothermal interaction, photoablation, or plasma-induced ablation (22). Photoablation occurs when absorption of a single photon by an electron promotes the electron from a bonding to a non-bonding orbital, resulting in dissociation of the molecule. Photoablation also results in a mechanical pressure wave radiating from the focal volume, a mechanism also known as cavitation. Plasma-induced ablation is due to a multi-photon absorption process resulting in quasi-free electrons and ionization within the focal volume (23). Like photoablation, plasma-induced ablation may also lead to formation of a cavitation bubble. Plasma-induced ablation is also associated with plasma formation, which can minimize excess damage in nearby tissues (26). These different mechanisms of laser-cell interaction can lead to significantly different outcomes for the targeted cell.

The critical factors that determine which of these mechanisms dominate in membrane disruption are the duration of the laser pulse and its irradiance. Although there is a large body of literature that discusses the relationship between pulse duration and ablative mechanism, there are few functional studies on single-cell viability post laser ablation (21). Here, we compare the effect of a nanosecond laser pulse (at 337nm) and femtosecond laser pulses (at 770nm) on single-cell viability post membrane disruption.

In single-cell nanosurgery, we first optically trap – either with optical tweezer (21) or with polarization-shaped optical vortex trap (6) – the sub-cellular organelle of interest, and then ablate a small opening (~ 1μm) in the membrane so we can remove the organelle from the cell. In this paper, we focus on the effect of membrane disruption on cell viability because our previous study established that cell viability in this procedure is not affected by organelle removal or irradiation by optical tweezers but due to the disruption of the plasma membrane (21). In this previous study, cellular damage was shown to lead quickly to either recovery or necrosis, and that cells would go through a period where they exhibited morphological stress responses like membrane blebbing before recovering. This prior study, however, only monitored cell viability post-surgery over a short timescale (4 hrs), while cell apoptosis has been known to occur over a longer timescale (27, 28). In our current study, we have followed the effect of membrane disruption on single cells over a 12 hour period using a combination of live/dead stain, apoptosis assay, and morphological observations, and compare the effect of one-photon (nanosecond UV pulse) and two-photon (femtosecond near IR pulses) membrane disruption of cell viability and apoptosis. In total, we have followed over 700 cells and

determined that a significant fraction of cells undergo apoptosis and that 2-photon membrane disruption offers the best result in enhancing cell viability.

4.2 EXPERIMENTAL

Cell Culture. NG108-15 cells (ATCC) were cultured in 75 cm^2 culture flasks in an incubator kept at 37 °C with 5% atmospheric CO_2. Cells were grown in DMEM (Gibco #11965) with 8% fetal bovine serum (Hyclone) and 1% penicillin/streptomycin (Gibco). Cells were split into home-made poly-(dimethylsiloxane) (PDMS) wells bonded to a photoetched glass coverslip (Bellco Glass) by bringing the pieces together after oxidation in oxygen plasma for 1 minute. Cells were split into the PDMS wells 24 hours before surgery and the surgery was conducted in the cell's native media. All surgery was conducted and all images were taken of cells that had been split into the PDMS wells. Cells were split at a low density to aid in identification during surgery and subsequent observation.

Cell Surgery. Two home-built optical setups were used for the cell surgery procedures. The schematic shown in figure 1 is a combination of the two optical setups which were on separate tables. The schematics were combined to economize figure space. The 1 Photon setup can be described as follows: a pulsed 337nm N_2 laser with a 3ns pulse width (Laser Sciences Inc.) was spatially filtered using an aspheric lens pair and a 100 μm pinhole to improve beam profile. Pulse duration is reported as the full width at half maximum intensity. The intensity of the pulsed laser was modulated using a neutral density filter. The beam was passed into a TE300 microscope (Nikon Instruments) with a 100× 1.3 NA Super Fluor objective (Nikon Instruments) with

improved UV transmission. Laser power was 750 nJ per pulse before the objective with 10% pulse-to-pulse variability and ~30% objective transmission at 337 nm. The focal spot size of the laser was determined by measuring the area of ablation of a thin layer of PMMA spin-coated onto a glass coverslip. Spot size for the UV laser was ~1.3 μm in diameter. The power level was chosen by finding the minimum pulse power necessary to disrupt the NG108 cellular membrane 50% of the time.

For the 2-photon surgery, a Ti:Sapphire tuned to 770 nm with a 110 fs pulse width and 80 MHz pulse frequency (Newport Tsunami) was directed through a neutral density filter (Thorlabs Inc.) and a 5 ms mechanical shutter (Uniblitz) with a home-built controller. The beam was passed into a TE2000 inverted microscope (Nikon Instruments) with a 100× 1.3 NA Super Fluor objective. Laser power was 0.150 W before the objective and the spot size was ~1.3 μm in diameter, measured by the same technique described above. The focal spot size of the Ti:Sapphire laser was increased to more closely resemble the spot size of the UV laser. The primary descriptive characteristics of the two lasers are shown in the table inset in figure 4.1.

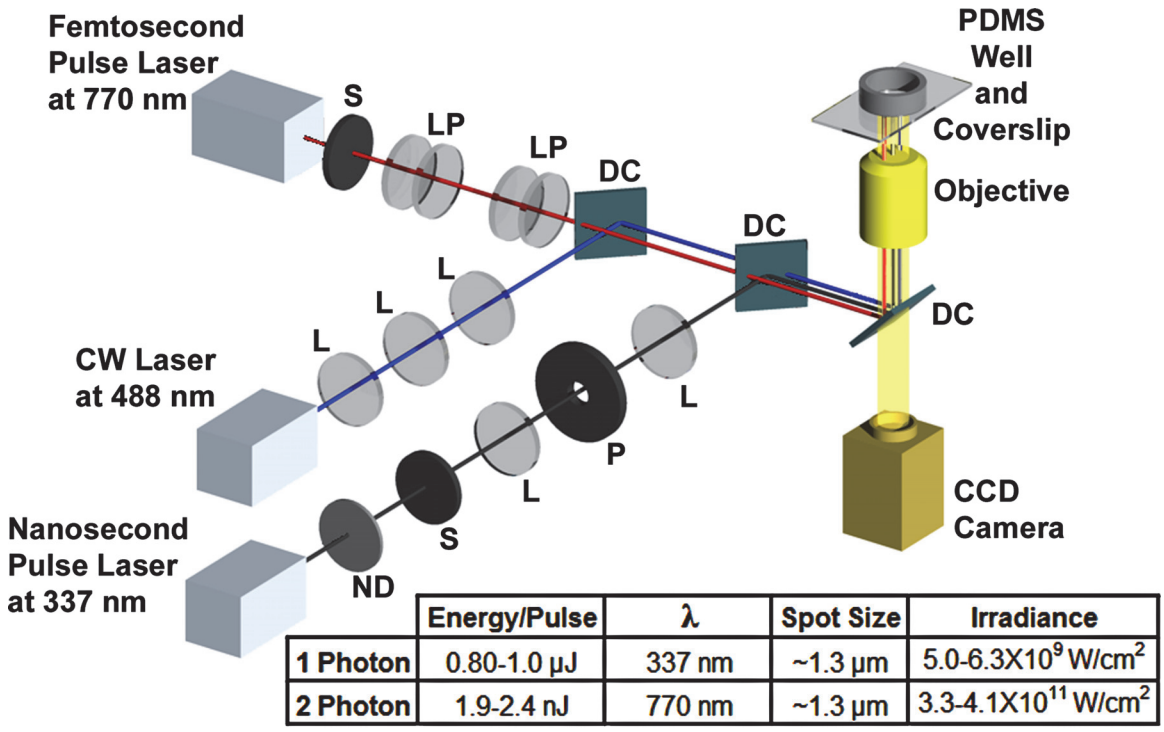

	Energy/Pulse	λ	Spot Size	Irradiance
1 Photon	0.80-1.0 μJ	337 nm	~1.3 μm	5.0-6.3X10^{9} W/cm^{2}
2 Photon	1.9-2.4 nJ	770 nm	~1.3 μm	3.3-4.1X10^{11} W/cm^{2}

Figure 4.1. Schematic depicting the optical setup used for 1-photon and 2-photon membrane disruption and subsequent cell observations. For 1-photon surgery, a 100 μm pinhole was used to spatially filter laser pulses and to improve beam profile. For 2-photon cell surgery, a second lens pair was added to adjust the size of the beam and to match the focal spot size to the spot size of the 1-photon laser. The 1 photon and 2 photon treatments were done on different optical tables, but the two laser schematics have been combined to economize space. L=lens, LP= lens pair, D=dichroic, M=mirror, ND=neutral density filter, P=pinhole, S=shutter. Inset: table listing the primary characteristics of consideration between the two lasers.

Cell Viability. For the time-sequenced cell viability assay, ethidium homodimer (Invitrogen) and calcein AM (Invitrogen) were used to assay cell viability over the course of 12 hours. The cells were stained with 4 μM calcein AM and 2 μM ethidium homodimer every hour for 12 hours. After each assay the cells were rinsed and returned to their native media.

Cell viability and apoptosis was monitored by a combination of fluorogenic dyes ethidium homodimer, MitoTracker Red, and the fluorescently labeled antibody Annexin V Alexa88 (Invitrogen). Cells were stained 11.25 hours after surgery with 200 nM MitoTracker Red and 2 μM ethidium homodimer and incubated for 30 minutes; they were rinsed and then stained with Annexin V Alexa488 for 15 minutes. Cells were viewed using epifluorescent illumination in a TE300 inverted microscope, a 20× 0.4 NA Plan objective (Nikon), and epi-illuminated by a 488nm sapphire laser (Coherent). Cells were imaged using a CCD camera (Cohu 4912). Color images were taken using DIC with de Sénarmont compensator and a color SLR CCD camera (Olympus E-300).

4.3 RESULTS AND DISCUSSION

Choice of cell line. We have shown in our previous study that cell viability post-surgery is widely variable depending on the cell line (21). In this prior work, we used a single 3ns pulse at 337nm for membrane disruption and a 1064nm YAG laser for optical trapping and removal of subcellular organelles. Of the three cell lines we studied (CHO: Chinese Hamster Ovary cells; NG108: a neuroblastoma fused with glioma cell line; ESD3: murine embryonic stem cells), we observed their 4-hrs post-surgery viability varied from ~80% (CHO), to ~30% (NG108), and ~10% (ESD3). The largest effect on cell viability was shown to be due to membrane disruption by the UV laser. To form a useful comparison between the one-photon disruption with 337nm nanosecond laser and the two-photon disruption with 770nm femtosecond laser, we decided the NG108 cells would offer the most information: if two-photon offers better cell viability than the one-photon process, we might not see the

improvement with CHO cells because of their already high viability at 80%; on the other hand, if two-photon offers less cell viability than one-photon disruption, then we might not see the decrease in cell viability with ES-D3 cells because of their already low viability at 10%.

Membrane disruption with nanosecond UV laser leads to apoptosis. As mentioned above, previous characterizations of cell viability did not encompass a sufficient duration to observe surgery-induced apoptosis. Figure 4.2 shows apoptosis induced in NG108 cells after single-pulse membrane disruption with the nanosecond UV laser. Here, we compared cell viability over 12 hours between cells that have undergone surgery and those that have not (control). All cells were stained with ethidium homodimer (ethidium) and calcein AM and then washed before counting the number of live and dead cells. Ethidium and calcein AM are common live/dead stains. When a cell is no longer viable its membrane becomes permeable to large molecules such as ethidium, which intercalates with the cell's DNA and exhibits strongly orange fluorescence. Calcein AM is a membrane permeable substrate that becomes fluorescent after it is cleaved by a cell's esterases, thus causing the cytoplasm of viable cells to fluoresce green. Therefore, cells were determined to be viable if they show green fluorescence in the cytoplasm and dead if they exhibit orange fluorescence in the nucleus. Figure 4.2A shows a flowchart that summarizes our procedure, in which we used ethidium and calcein AM to check the viability of both control cells and cells that underwent surgery every hour for 12 hours.

Figure 4.2B shows our results, in which the difference in survival rates between hours 1 and 12 of the two groups (control versus post-surgery cells) is clear. Between surgery and hour 1, 39% of the NG108 cells survived after their membranes had been disrupted compared to 95% survival in the control group. We attribute cell death between 0 and 1 hour mostly to cell necrosis. Between hours 1 and 12, of the 39% post-surgery cells that survived after hour 1, only 39% of the remaining cells survived to hour 12. In contrast, of the 95% control cells that are alive after hour 1, 80% of the remaining cells are still viable at hour 12. Overall, 16% of the UV laser treated group was viable after 12 hours compared to 76% in the control. The right side of figure 2B summarizes the percent of cells that died between hours 1 and 12, which we attribute to apoptosis. The ratio of cells that died from hours 1 to 12 between of laser disrupted cells to control cells is ~3:1. This result suggests laser ablation of cell membrane affects not only short-term cell viability but also can lead to apoptotic cell death later.

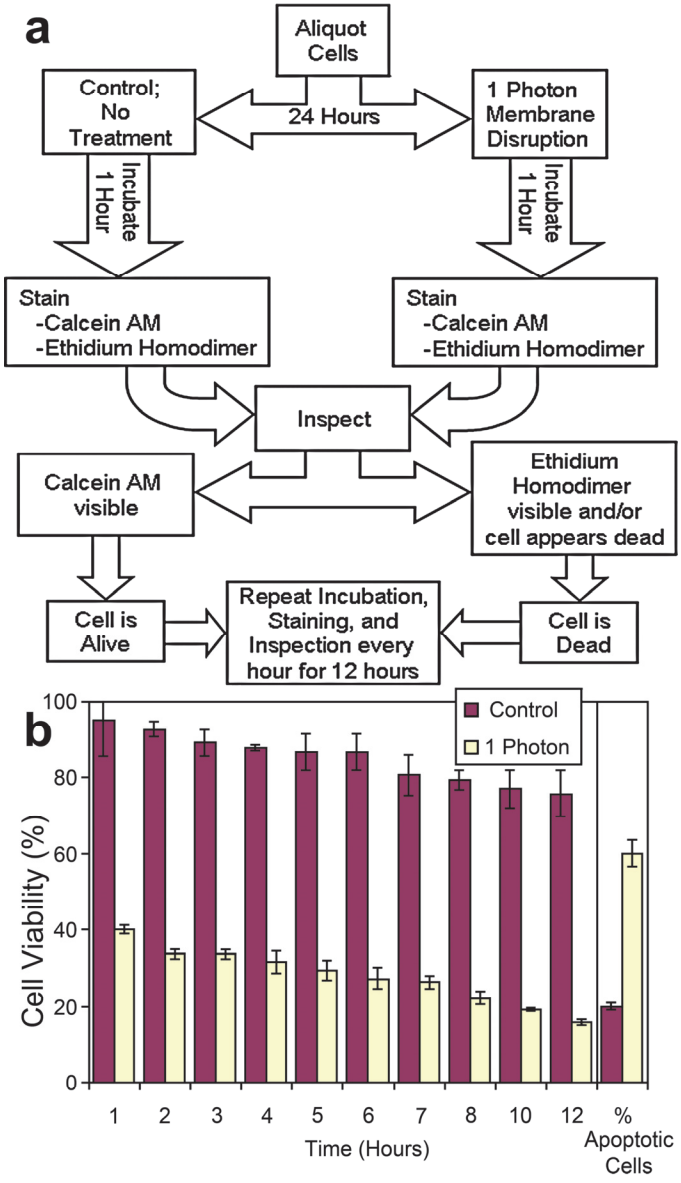

Figure 4.2. (a) A flow chart summarizing the procedure we used to monitor cell viability over 12 hours with live/dead stains (ethidium and calcein AM). (b) A histogram showing the viability of NG108 control cells and cells that underwent surgery. Each bar gives the number of cells alive at the given time. The data points labeled "% Apoptotic Cells" shows the percentage of cells that were viable after the first hour, but were not viable at hour 12, and thus are presumed to have undergone apoptosis. Cells that were exposed to a UV pulse were much more likely to undergo apoptosis (i.e. died between hours 1 and 12) than the control group. The error bars represent the 95% confidence intervals.

Morphological effects of cell surgery. In addition to fluorescent live/dead stains, the morphology of cells also provides valuable information in determining necrotic and apoptotic cells. Non-viable cells often develop large membrane blebs, lose adherence to the surface, develop granular appearance of cytoplasm, have condensation of the nucleus, and conform to a more spherical shape. In figure 4.3, one cell was viewed for 30 minutes (a1-a8) after it underwent surgery (a1); here, the cell increased in granularity (a2-a8) and formed a large membrane bleb and died (a5-a8). Another cell was viewed after surgery for a period of 12 hours (b1-b12); this cell formed blebs (b3-b5), then recovered (b6-b11), but ultimately underwent apoptosis (b12). It is important to note that although the cell appeared healthy and recovered after 10 minutes, cell apoptosis was verified visually after 12 hours.

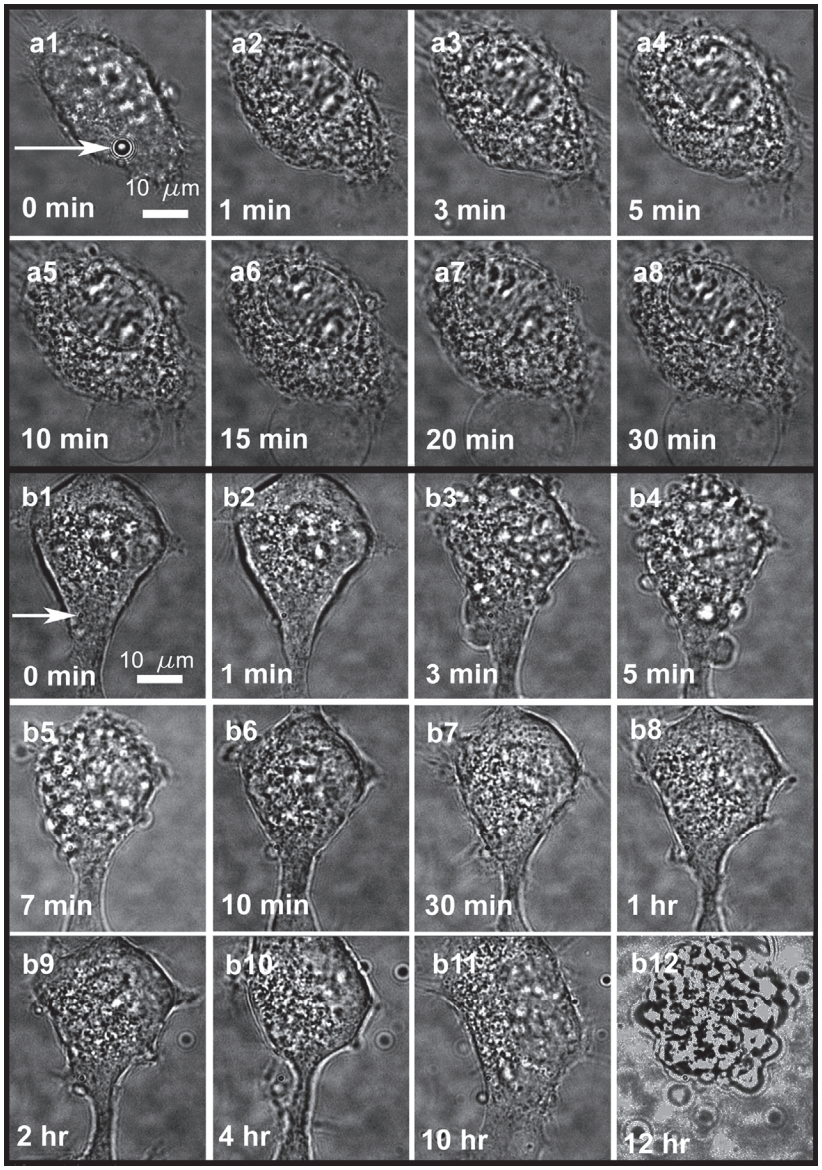

Figure 4.3. Monitoring of morphological changes after membrane disruption with a single nanosecond UV laser pulse. Panels a1-a8 follow an NG108 cell as it was ablated (a1), formed a large bleb and died (a3-a8). Panels b1-b12 follow an NG108 cell as it was ablated (b1), formed blebs (b3-b5), and recovered (b6-b11) before the cell ultimately underwent apoptosis (b12). Arrows in panels a1 and b1 show sites of UV irradiation. A cavitation bubble is visible in panel a1. Cells were kept at 37 °C in an integrated incubator on the microscope for long-term observation.

Apoptosis assay. Given the presence of apoptosis, in our comparison between one-photon and two-photon membrane disruption, we chose to monitor the cells after 12 hours using three assays: MitoTracker Red, ethidium, and the fluorescent antibody conjugate Annexin V Alexa488. MitoTracker Red was used to monitor mitochondrial membrane potential; it is strongly fluorescent in the membranes of mitochondria that are able to maintain a potential gradient and fluorescence decreases sharply as mitochondria lose function and are unable to maintain a potential gradient. Annexin V Alexa488 (AVA488) is a membrane impermeable antibody conjugated to a fluorophore (Alexa488) that binds to phosphatidylserine (PS). AVA488 can be used to detect apoptosis because PS is localized to the inner leaflet of the lipid bilayer of a healthy cell but becomes present on the outer leaflet and allows AVA488 to bind to it as the cell undergoes apoptosis. It is quite beneficial to use AVA488 combined with MitoTracker Red because the two in conjunction can be used to visualize early stages of apoptosis before more obvious morphological changes become visible.

Figure 4.4 shows the appearance of a healthy (a1-a2) and apoptotic (b1-b2) cell as visualized with these three assays. Compared to the healthy cell in a2, the apoptotic cell in b2 shows increased granularity in the cytoplasm, decreased MitoTracker Red fluorescence, and visible fluorescence from both AVA488 and ethidium. In all subsequent experiments using these three assays, the viability of each cell was only counted once at the end (~ 12 hours) of the experiment, which was done to maximize cell viability by limiting cell exposure to cytotoxic membrane stains and repeated rinsing.

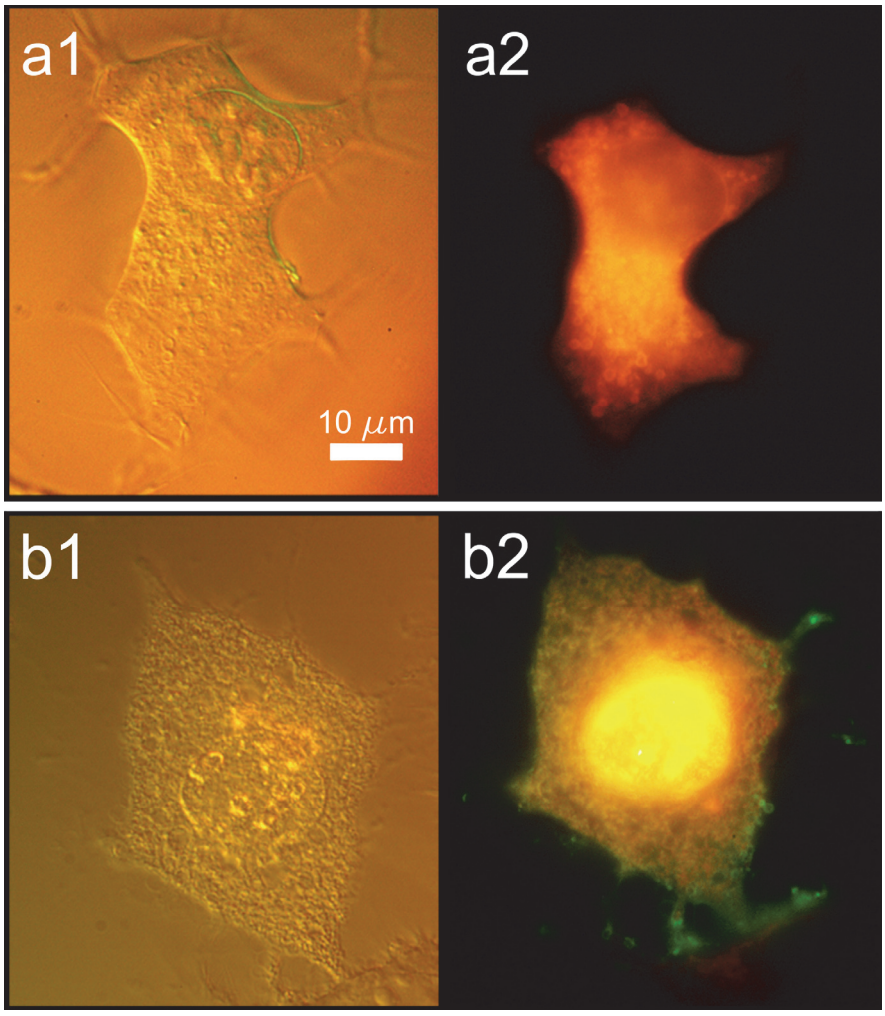

Figure 4.4. Apoptosis assay. Panels a1 and a2 are images of the same healthy cell observed using DIC in a1 and then with epi-fluorescence in a2. Panels b1 and b2 are images of a second cell undergoing apoptosis, also observed using DIC (b1) and epi-fluorescence (b2). In a2 the intense fluorescence from MitoTracker Red signifies that the mitochondria are able to maintain a potential gradient. In panel b2, the cell is undergoing apoptosis: MitoTracker Red fluorescence is decreased, ethidium has penetrated the cell's membrane and intercalated with the cell's DNA, and Annexin V Alexa488 has bound to the cell's membrane.

Viability of cells after one- and two-photon membrane disruption. We disrupted the membranes of over 600 cells and then monitored their viability after 12 hours to better understand the effect of membrane disruption using one-photon versus

two-photon ablation. NG108 cells were treated with two different lasers, each at two different powers. For each laser, we chose two power levels, one at which corresponded to a 50% Probability of Membrane Disruption (PMD), and another that corresponds to a 90% PMD. To determine whether the membrane was disrupted, we used single laser pulses (1 photon surgery) or pulse trains (2 photon surgery) and visually verified the formation of transient membrane holes.

For the N_2 laser the energy required was 800 nJ and 1.0 μJ for 50% and 90% PMD, respectively; here, we used a single pulse to ablate the membrane. For the fs laser, we used a 5 ms train of pulses at 80 MHz and at powers of 150 mW and 190 mW for 50% and 90% PMD, respectively. If a hole was not visible after one pulse or pulse train, the cell was excluded from further observation. Again, the focal spot size for both lasers was ~ 1.3 μm in diameter, and all powers were measured before the objective. The viability of each cell was determined by observing cell morphology concurrently with the three assays shown in figure 4.4.

Figure 4.5 is a histogram of cell survival that shows our results. There is a large difference in cell viability between the control and UV-ablated cells after 12 hours, consistent with our previous findings[21]. The control group remained 80% viable after 12 hours, while 36% of the cells disrupted by a UV pulse at both 50% and 90% PMD were viable after 12 hours. The cells disrupted by the femtosecond pulse train were ~80% viable in both the 50% PMD and 90% PMD groups, which is identical, within error, to the viability rate of the control group.

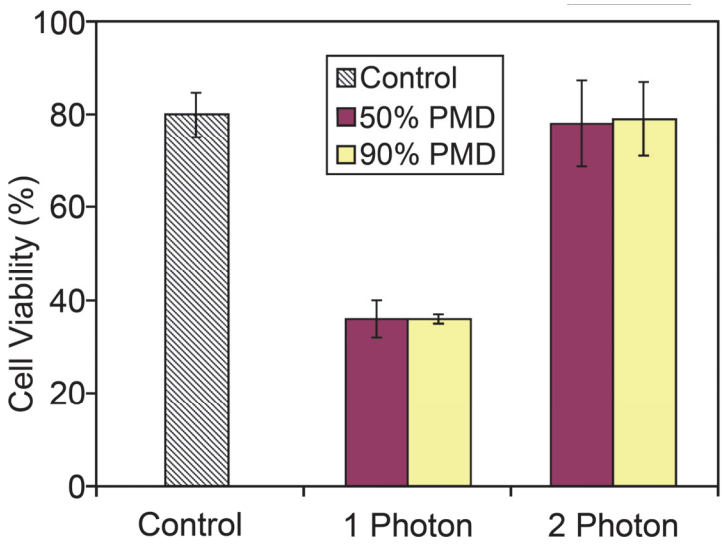

Figure 4.5. Histogram showing overall cell viability after 12 hours for 50% and 90% Probability of Membrane Disruption (PMD). The error bars represent 95% confidence interval.

4.4 CONCLUSIONS

The experiments presented here constitute a functional study of the end effect of laser ablation on cell viability. Our biological results agree well with the physical studies on the mechanism of one-photon and two-photon ablation reported in the literature, which shows one-photon ablation usually results in the formation of larger cavitation bubbles that lead to more extensive damage than two-photon ablation. From the results of our study, we can draw three conclusions: (1) Although most cell death occurs immediately (within 1 hr) after laser surgery, a significant portion of cells die because of laser-surgery induced apoptosis, (2) Two-photon ablation offers significant enhancements in cell viability compared with one-photon ablation and should be used whenever possible, and (3) The difference in energy required to increase PMD to 90% from 50% is not large enough to affect cell viability, thus power levels that correspond to >90% PMD

can be used in most cell-surgery experiments. The drawback of two-photon ablation is the significant increase in cost of instrumentation, as femtosecond lasers currently are about an order of magnitude more expensive than nanosecond pulsed lasers. Nevertheless, this added cost might be worthwhile for applications that require high cell viability post laser surgery.

REFERENCES

1. Neuman, K.C. and S.M. Block (2004). Optical trapping. *Rev Sci Instr*. **75**, 2787-2809.
2. Heisterkamp, A., I.Z. Maxwell, J.M. Underwood, J.A. Nickerson, S. Kumar, and D.E. Ingber (2005). Pulse energy dependence of subcellular dissection by femtosecond laser pulses. *Opt Express*. **13**, 3690-3696.
3. Blake, D.A., A.S. Forsberg, B.R. Johansson, and M. Wikland (2001). Laser zona pellucida thinning-an alternative approach to assisted hatching. *Hum Reprod*. **16**, 1959-1964.
4. Tirlapur, U.K. and K. Konig (2002). Femtosecond near-infrared laser pulses as a versatile non-invasive tool for intra-tissue nanoprocessing in plants without compromising viability. *Plant J.* **31**, 365-374.
5. Henriksen, H., A.R. Taylor, C. Brownlee, and S.M. Assmann (1996). Laser Microsurgery of Higher Plant Cell Walls Permits Patch-Clamp Access. *Plant Physiol*. **110**, 1063-1068.
6. Jeffries, G.D.M., J.S. Edgar, Y. Zhao, J.P. Shelby, C. Fong, and D.T. Chiu (2007). Using Polarization-Shaped Optical Vortex Traps for Single-Cell Nanosurgery. *Nano Lett*. **7**, 415-420.
7. Kohli, V., J.P. Acker, and A.Y. Elezzabi (2005). Reversible Permeabilization Using High-Intensity Femtosecond Laser Pulses: Applications to Biopreservation. *Biotech Bioeng*. **92**, 889-899.
8. Mehier-Humbert, S. and R.H. Guy (2005). Physical methods for gene transfer: Improving the kinetics of gene delivery into cells. *Adv Drug Del Rev.* **57**, 733-753.
9. Stevenson, D., B. Agate, X. Tsampoula, P. Fischer, C.T.A. Brown, W. Sibbett, A. Riches, F. Gunn-Moore, and K. Dholakia (2006). Femtosecond optical transfection of cells: viability and efficiency. *Opt Express*. **14**, 7125-7133.
10. Khodjakov, A., R.W. Cole, and C.L. Rieder (1997). A Synergy of Technologies: Combining Laser Microsurgery With Green Fluorescent Protein Tagging. *Cell Motil Cytoskeleton*. **38**, 311-317.
11. Krasieva, T.B., C.F. Chapman, V.J. LaMorte, B. Venugopalan, M.W. Berns, and B.J. Tromberg (1998). Cell permeabilization and molecular transport by laser microirradiation. *SPIE Proceedings.* **3260**, 38-44.
12. Palumbo, G., M. Caruso, E. Crescenzi, M.F. Tecce, G. Roerti, and A. Colasanti (1996). Targeted gene transfer in eukaryotic cells by dye-assisted laser optoporation. *J Photochem Photobiol B.* **36**, 41-46.
13. Soughayer, J.S., T. Krasieva, S.C. Jacobson, J.M. Ramsey, B.J. Tromberg, and N.L. Albritton (2000). Characterization of Cellular Optoporation with Distance. *Anal Chem*. **72**, 1342-1347.
14. Tao, W., J. Wilkinson, E.J. Stanbridge, and M.W. Berns (1987). Direct gene transfer into human cultured cells facilitated by laser micropuncture of the cell membrane. *Proc Natl Acad Sci*. **84**, 4180-4184.
15. Tirlapur, U.K. and K. Konig (2002). Targeted transfection by femtosecond laser. *Nature.* **418**, 290-291.
16. Paterson, L., B. Agate, M. Comrie, R. Ferguson, T.K. Lake, J.E. Morris, A.E. Carruthers, C.T.A. Brown, W. Sibbett, P.E. Bryant, F. Gunn-Moore, A.C. Riches, and K. Dholakia (2005). Photoporation and cell transfection using a violet diode laser. *Opt Express.* **13**, 595-600.
17. Schneckenburger, H., A. Hendinger, R. Sailer, W.S.L. Strauss, and M. Schmitt (2002). Laser-assisted optoporation of single cells. *J Biomed Opt.* **7**, 410-416.
18. Quinto-Su, P.A., L. Hsuan-Hong, H.H. Yoon, C.E. Sims, N.L. Albritton, and V. Venugopalan (2008). Examination of laser microbeam cell lysis in a PDMS microfluidic channel using time-resolved imaging. *Lab Chip*. **8**, 408-414.
19. Supatto, W., D. Debarre, B. Moulia, E. Brouzes, J.L. Martin, and E. Farge (2004). In vivo modulation of morphogenetic movements in Drosophila embryos with femtosecond laser pulses. *Proc Natl Acad Sci.* **102**, 1047-1052.
20. Allen, P.B., A.E. Sgro, D.L. Chao, B.E. Doepker, J. Scott Edgar, K. Shen, and D.T. Chiu (2008). Single-synase ablation and long-term imaging in live C. elegans. *J Neurosci Methods.* **173**, 20-26.
21. Shelby, J.P., J.S. Edgar, and D.T. Chiu(2005). Monitoring Cell Survial After Extraction of a Single Subcellular Organelle Using Optical Trapping and Pulsed-Nitrogen Laser Ablation. *Photochem Photobiol.* **81**, 994-1001.
22. Niemz, M.H. (2004). Interaction Mechanisms. In *Laser-Tissue Interactions: Funamentals and Applications* pp. 45-149. Springer, Heidelberg, Germany.
23. Vogel, A., J. Noack, G. Huttman, and G. Paltauf (2005). Mechanisms of femtosecond laser nanosurgery of cells and tissues. *Appl Phys B*. **81**, 1015-1047.

24. Vogel, A., J. Noack, K. Nahen, D. Theisen, S. Busch, U. Parlitz, D.X. Hammer, G.D. Noojin, B.A. Rockwell, and R. Birnbruber (1999). Energy balance of optical breakdown in water at nanosecond to femtosecond time scales. *Appl Phys B*. **68**, 271-280.
25. Venugopalan, V., A. Guerra, K. Nahen, and A. Vogel (2002). Role of Laser-Induced Plasma Formation in Pulsed Cellular Microsurgery and Micromanipulation. Phys Rev Lett. **88**, 078103.
26. Hammer, D.X., D.E. Jansen, M. Frenz, and G.D. Noojin (1997). Shielding properties of laser-induced breakdown in water for pulse durations from 5 ns to 125 fs. *Appl Opt.* **36**, 5630-5640.
27. Jessel, R., S. Haertel, C. Socaciu, S. Tykhonova, and H.A. Diehl (2002). Kinetics of apoptotic markers in exogeneously induced apoptosis of EL4 cells. *J Cell Mol Med*. **6**, 82-92.
28. Lizard, G., S. Fournel, L. Genestier, N. Dhedin, C. Chaput, M. Flacher, M. Mutin, G. Panaye, and J.P. Revillard (1995). Kinetics of Plasma Membrane and Mitochondrial Alterations in Cells Undergoing Apoptosis. *Cytometry*. **21**, 275-283.

Chapter 5: Single-Cell Nanosurgery

5.1 INTRODUCTION

The effects of focused laser light on living bodies, ranging from single cells to entire organisms, have been thoroughly researched[1-3]. At the scale of entire organisms, lasers have been used in neuroscience applications, like the ablation of individual synapses in *Caenorhabditis elegans*[4,5], or in developmental biology with model organisms such as *Drosophila melanogaster*[6] or zebrafish[7]. Laser surgery is also particularly advantageous for single cell or sub-cellular studies because mammalian cells are highly heterogeneous and segregated into biologically relevant units[8], such as organelles, which are comparable in size to the diffraction-limited focal spot of a laser.

High numerical aperture (NA) objective lenses can focus laser light down to spots on the order of hundreds of nanometers, which provide excellent spatial resolution without the need to physically manipulate the sample. When these diffraction-limited spots for spatially localized ablation are paired with a single-beam gradient optical trap, also known as optical tweezers, cell surgery can add exogenous material[9] or remove organelles from individual cells[1]. Optical tweezers are not limited to biological samples and can be used to trap any object with a higher refractive index than its surroundings, assuming it is of an appropriate size and the trapping laser has sufficient power. A set-up with optical tweezers and an ablation laser is amenable to a wide array of complementary biophysical laboratory techniques, such as fluorescence microscopy, and they have generated great interest for some time[10,11].

Post-surgery, the cell may do one of three things: it may recover and remain a viable cell; it may undergo laser-induced necrosis, known as "opticution"; or it may undergo apoptosis over a period of many hours. Our area of interest has been in the viability of different cell lines following cell surgery[1] and the effect of different membrane disruption techniques on cell survival[3]. The method described here explains how to monitor the long-term viability of a single cell after the removal of an organelle by laser nanosurgery.

5.2 MATERIALS

5.2.1 Polydimethylsiloxane (PDMS) wells used for cell surgery and staining

1. Sylgard elastomer kit (Dow Corning, Midland, MI)
2. Photoetched glass coverslips (Bellco, Vineland, NJ)
3. Scientific oven.
4. Plasma cleaner (Harrick Plasma, Ithica, NY)
5. Vacuum pump.
6. Vacuum chamber.

5.2.2 Cell culture equipment and reagents

1. All cell types were grown in 75-cm^2 culture flasks and stored in an incubator with 5% CO_2 atmosphere at 37 °C.
    a. NG108-15 cells (ATCC, Manassas, VA) grown in Dulbecco's modified Eagle's medium (DMEM), supplemented with 8% fetal bovine serum, (FBS), and 1% penicillin/streptomycin.
    b. CHO-M1 cells (ATCC) grown in DMEM with 10% FBS and 1% penicillin/streptomycin.

c. ES-D3 (ATCC) grown in DMEM with 10% FBS and leukocyte inhibitory factor to prevent differentiation.

2. 0.25% trypsin-EDTA solution.
3. PDMS wells for cell surgery
4. Milli-Q water.

5.2.3 Optical Setup

1. Microscope: TE2000 microscope (Nikon, Mellville, NY) with epi-illumination port, camera port, turret for optical filter cubes, bright field light source and condenser.
2. Objective: 100× magnification 1.3 NA S Fluor oil immersion objective (Nikon, Mellville, NY).
3. Differential Interference Contrast (DIC) with de Sentamount optics for bright field imaging to improve contrast.
4. Video capture: CCD camera (Cohu, San Diego, CA)
5. Ablation laser: nanosecond pulse 337-nm N_2 Ultraviolet laser (Laser Sciences, Inc., Franklin, MA)
6. Laser for optical tweezers: continuous wave (CW) Nd:YAG laser with a TEM_{00} Gaussian beam profile (Spectra Physics, Mountain View, CA)
7. Laser power meter (Ophir Optronics, Jerusalem, Israel)
8. Assorted neutral density (ND) filters, dichroics, lenses, optical filters, mirrors, and optomechanics (Omega Optical, Burlington, VT, Thorlabs, Newton, NJ, and Chroma Tech Corp, Rockingham, VT)

5.2.4 Cell Viability Assay

1. 2 μM ethidium homodimer.
2. 200 nM MitoTracker Red (Invitrogen, Grand Island, NY)
3. Annexin V Alexa fluor 488 (Invitrogen, Grand Island, NY)
4. 488-nm CW sapphire laser (Coherent, Santa Clara, CA)

5.3 METHODS

5.3.1 Making PDMS Wells

1. Mix the Sylgard elastomer kit base and catalyst thoroughly in a 10:1 ratio in a disposable cup; 100 grams of base and 10 grams of catalyst are enough to make ~12 wells.
2. Place the un-cured silicone mixture in the vacuum chamber and pump air out of the chamber to remove air bubbles.
3. Pour the PDMS into a large petri dish. We have found that placing evenly spaced glass vials with a diameter slightly smaller than the 1" photoetched coverslips make suitable molds to shape the PDMS as it cures. To ensure that the vials do not move through the PDMS before it hardens, keep the vials in place using a petri dish lid with holes drilled such that the vials go through the holes and thus are held in place by the holes in the lid.
4. Bake at 60 °C for at least 1 hour to cure.
5. Pull out the glass vials from the PDMS, remove the PDMS from the petri dish, and cut out the individual wells.
6. Expose PDMS and photoetched glass coverslips to oxygen plasma for 60 seconds.

7. Seal the PDMS to the coverslip by bringing both together; apply light pressure to expunge any air pockets between the glass and PDMS.

5.3.2 Membrane Disruption

1. Split cells into a PDMS well 24 h before surgery using the cell's native media. The cells should be split at a low density to aid in identification during surgery and subsequent observation (see Note 1). Just prior to surgery, supplement the media in the PDMS well with ~25% Milli-Q water to induce cell swelling and help organelle extraction.
2. For the pulsed N_2 laser to disrupt the membrane, use a beam expander or lens pair to collimate and expand the beam to fill the back aperture of the microscope objective. This will produce a sub-micron focal spot size. We would recommend mounting at least one lens base on a rail to facilitate alignment of the focal spot in the axial direction.
3. Each laser pulse needs ~800 nJ of energy per pulse when measured before the objective. Our particular laser has a 10% pulse-to-pulse variability in pulse energy at 2 Hz at a 3-ns duration, and the objective has a roughly 30% transmission efficiency. This power is sufficient to disrupt the plasma membrane of a NG-108 cell with a single pulse to allow organelle extraction 50% of the time. Greater laser powers could lead to excessive cell damage and large cavitation bubbles; lower powers would have no visible effect. We modulate the pulsed laser's power using a neutral density filter and select the laser pulses using a shutter controlled by a transistor-transistor logic (TTL) switch.

4. Laser pulses should target the cell's plasma membrane to maximize membrane disruption and minimize cell damage (see Note 2). Focusing on the coverslip leads to ablation of the coverslip and immediate cell lysis; focusing on the cell cytoplasm creates large cavitation bubbles and excessive cell damage. Regardless of where the laser focus is directed, morphological changes will be evident for all cells following surgery.
5. If post-surgery cell viability is important and the cell line is particularly susceptible to death after surgery, a femtosecond near-IR pulse laser, instead of a nanosecond UV pulse laser, may improve cell viability. The mechanism of membrane disruption greatly affects cell viability after surgery ***(3)***. Membrane disruption by multi-photon absorption from a femtosecond laser produces a smaller focal volume, smaller cavitation bubbles, and other effects that help cell viability ***(2)***. The drawbacks of using a femtosecond laser for surgery are added cost and complexity.

5.3.3 Optical Trap Construction

This section provides brief guidance on the construction of a simple, robust, single-beam, gradient-force, three dimensional optical trap with commercially available components. If more detail or explanation of optical alignment is needed, more comprehensive guides are available[12]. With additional modification, trap position sensing[13], vortex-shaped optical traps[14], multiple traps[15,16], force measurements[17,18], and a myriad of other techniques are possible[19] but are beyond the scope of this chapter.

1. An inverted microscope is a stable and flexible platform for optical trapping. The back epifluorescence port is convenient for directing the trapping beam into the

objective. Most research-grade inverted microscopes also come with a turret where multiple beamsplitter cubes may be installed, which makes it convenient to switch between cell surgery and epifluorescence imaging modes. It is possible to build a platform for optical trapping without a microscope, but this requires a high degree of expertise in microscopy.

2. The objective lens is probably the most critical element of the optical trapping setup. For stable trapping, a high NA objective lens is necessary to generate the tight focus ***(20)***, such as the Nikon S Fluor 1.3 NA 100× oil immersion objective lens.
3. CW lasers emitting in the NIR, like the Nd:YAG laser, are used for optical trapping because they produce sufficient power at a wavelength that is relatively transparent to cells. Wavelengths shorter than ~700 nm are more readily absorbed by cells and should be avoided if possible because the high intensity in the focal volume results in excessive photodamage. Also, the laser should have an M^2 <1.1 and emit the TEM_{00} mode to produce a light gradient steep enough to form a stable optical trap. For the sake of safety, a shutter should be installed at the point immediately after the beam exits the laser (see Note 3).
4. Place a dichroic mirror in the microscope's laser filter cube so that it will reflect IR and UV light but allow visible light to pass through. After alignment of the IR laser, an emission filter used should also block back-reflected IR and UV light from the optical tweezers and the ablation laser (see Note 4).
5. The power of the trapping beam should be minimized, but still be great enough to stably trap the organelle of interest. Most Nd:YAG lasers emit significantly more

power than is necessary. The power is best modulated by using a λ/2 waveplate installed in a rotating mount followed by a polarizing beamsplitter and a beam block that absorbs the excess laser power. With this configuration, the laser's power can be attenuated by rotating the waveplate. Controlling the laser power by external means instead of adjusting the drive current of the laser improves the laser power stability.

6. After the power attenuator, insert a pair of lenses into the beam path that expand the beam to fill or slightly overfill the back aperture of the objective. Beam expanders are commercially available for this purpose.

7. The most convenient way to steer the optical trap is by using a combination lens pair and a mirror to create a 4f system. Mount the lens nearest the microscope on a x, y, z movable lens mount and arrange the lens pair so that each lens is the same distance from the central focal spot as its focal length. The lenses closest to the objective can be used to fine-tune the alignment of the optical tweezers. The movement of the final lens along the optical axis can be used to adjust the height of the optical trap above the objective. This adjustment will ensure that the plane of the optical trap and the image are parfocalized (see Note 5). The mirror is installed in a kinematic mirror mount at the conjugate focal plane of the objective and can be used to steer the optical trap (figure 5.1).

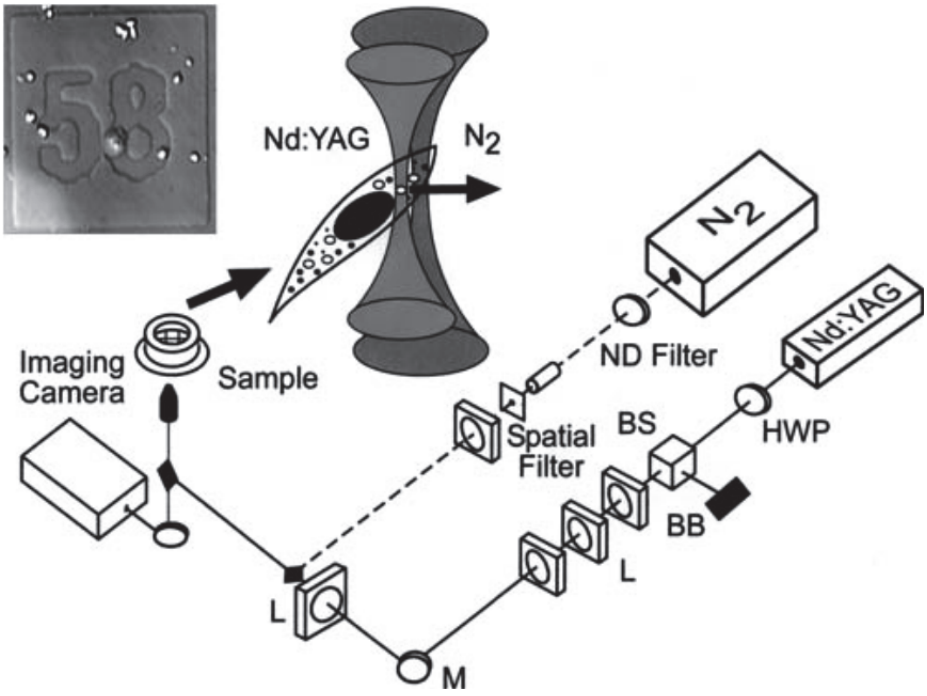

Reprinted with permission from (1)

Figure 5.1. Schematic of optical set-up. The outputs of a pulsed-N_2 laser (337 nm; 3-ns pulse width) and a CW Nd:YAG laser (1064 nm) were aligned collinearly and sent into the microscope. The two beams were directed into the objective (N.A.=1.3) by a dichroic mirror and focused onto the cell by the objective lens. The microscope was equipped with Nomarski optics but the components are omitted in the schematic for clarity. The pulsed N_2 laser (~0.7 μJ) was used to ablate a small hole (~1–3 μm) in the cell membrane and the YAG trapping laser (200 mW) was employed to extract a subcellular organelle (arrow pointing away from focal volume). To track individual cells post-surgery, we cultured cells in PDMS wells formed by sealing PDMS to photoetched coverslips (upper left inset). HWP=half wave plate, BS=polarizing beam splitter, BB=beam blocker, ND=neutral-density filter, M=mirror, L=lens.

5.3.4 Organelle Trapping

1. Organelle trapping is performed using the optical tweezers described in the previous section. For our set-up, a power of ~200 mW at the nosepiece of the microscope generates a sufficient gradient force to trap individual organelles. The power transmitted through the microscope's objective will vary depending on the %

transmission through the objective and whether or not the trapping beam is larger than the back aperture of the objective[13].

2. Organelles near the spot of membrane disruption can be extracted from the cell after steering of the trapping beam (see Note 6). Adding Milli-Q water to the media improves the ease of organelle extraction without significantly reducing cell viability, but a small amount of cytoplasm is still often extracted with the targeted organelle (figure 2). The extracted organelles are often lysosomes or mitochondria. These organelles can be differentiated with the appropriate fluorescent stain.
3. We have observed that the high fluence of the IR laser leads to fast photobleaching of organelle stains and possible photo-damage to the organelle. If the extracted organelle is intended for further analysis, such as single mitochondria capillary electrophoresis[21], photobleaching and photo-damage to the organelle can be reduced by using an optical vortex trap (14) instead of the Gaussian optical trap described above.

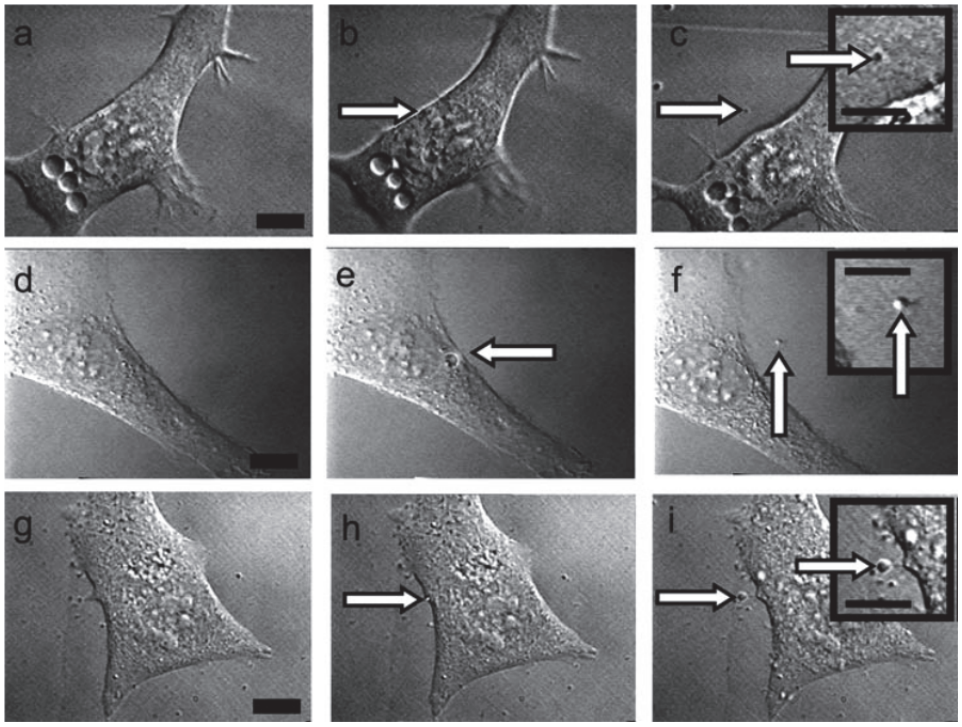

Reprinted with permission from (1)

Figure 5.2. Organelle extraction in successful surgeries. An NG108-15 cell (a) before, (b) during and (c) after surgery; the arrows point to the organelle that was extracted. A similar sequence showing a CHO cell (d) before, (e) during and (f) after surgery. A small cavitation bubble is visible in (e); (f) shows the organelle (arrow) that was completely removed from the cell. An ES-D3 stem cell (g) before, (h) during and (i) after surgery. Scale bars=10 μm.

5.3.5 Cell Viability Monitoring

1. After surgery, incubate the cells at regular intervals in pre-warmed media for 10 minutes containing the viability reagents (see **section 5.2.4**). The particular dyes are chosen to determine cell viability because (a) they can all be excited with a single 488 nm laser, (b) their fluorescence is spatially and spectrally distinct so they are easily resolved, and (c) in addition to cell necrosis, they also suggest apoptosis prior to the morphological signs of apoptosis, which may take many hours to become apparent. Ethidium homodimer is a membrane-impermeable dye that will brightly

stain the cell nucleus if the membrane loses integrity. MitoTracker Red is a mitochondrial stain that will have a significant decrease in brightness if the mitochondria lose the ability to maintain a proton gradient across their membrane. Annexin V Alexa fluor 488 is a membrane-impermeable antibody that binds to phosphatidylserine, a phospholipid that can be found on the external leaflet of a cell's lipid bilayer only during apoptosis.

2. After 10 minutes, remove the cells from the incubator and wash with fresh pre-warmed media. Cell viability can be determined by observing the fluorescent stains and cell morphology. Some morphological indicators that a cell is dying, such as membrane blebs, a granular appearance in their cytoplasm, more spherical shape, and loss of adherence to the coverslip, can be viewed under bright field microscopy.

3. Cell apoptosis can be differentiated with bright field DIC and epifluorescence illumination. The viable cell (a1, a2) has a normal morphology under bright field and displays bright orange fluorescence under epifluorescent illumination from the MitoTracker stain. The cell undergoing apoptosis (b1, b2) has a more granular appearance under bright field. Under epifluorescence, it has decreased emission intensity from MitoTracker but a brightly fluorescent nucleus from the ethidium homodimer and a green fluorescent plasma membrane as Annexin V Alexa 488 binds to the lipid bilayer.

5.4. NOTES

1. Cells are known to migrate over time, a property dependent on the cell line. If long-term observation is necessary, be sure to either split the cells at a lower density or take images regularly to track cell movement. Photoetched glass coverslips also help to track individual cells.
2. When performing cell surgery, watch the surgery with a CCD camera. Do not use the microscope's oculars. IR light can leak through the microscope's oculars so place a light blocker over them when appropriate to prevent accidental exposure.
3. Proper laser safety is crucial and should include the appropriate laser goggles, beam blocks, shut-off keys, IR laser display cards, and so on. Safety measures are especially important in cell laser surgery because both the trapping and ablative lasers are outside the visible range and scattered light from either laser may be intense enough to cause eye damage.
4. Back reflection from optical tweezers can be intense enough to damage the camera so make sure its power is minimized during alignment and that the proper IR emission filter is in place.
5. The distance from the focal spot where an object is trapped by the optical tweezers can change with the object's size and composition. Some tweaking of the trap's focal spot may be necessary when trapping different samples to keep the objects in the same plane as the imaging plane.
6. If the emission filter blocks 100% of the back-reflected IR and UV light, then the trapping beam and ablation laser are invisible to the camera. Organelle extraction is

easier if you find a method for tracking the position of the trapping beam and the ablative pulsed laser so that they do not get lost between experiments or are steered outside the field of view of the camera. There are many ways to track the beams depending on the application: It can be as complex as building a trapping positioning system or as simple as marking the laser beam focal points on the monitor with a dry-erase marker.

REFERENCES

1. Shelby JP, Edgar JS, Chiu DT (2005) Monitoring Cell Survival After Extraction of a Single Subcellular Organelle Using Optical Trapping and Pulsed-Nitrogen Laser Ablation. Photochem Photobiol 81(4):994-1001
2. Niemz, MH (2004) Laser-Tissue Interactions. Springer, Heidelberg
3. Zeigler MB, Chiu DT (2009) Laser Selection Significantly Affects Cell Viability Following Single-Cell Nanosurgery. Photochem Photobiol 85(5):1218-1224
4. Allen PB, Sgro AE, Chao DL et al (2008) Single-synapse ablation and long-term imaging in live C. elegans. J Neurosci 173(1):20-26
5. Chung SH, Mazur E (2009) Femtosecond laser ablation of neurons in C. elegans for behavioral studies. Appl Phys A-Mater 96:335-341
6. Chang TN, Keshishian H (1996) Laser Ablation of Drosophilia Embryonic Motoneurons Causes Ectopic Innervation of Target Muscle Fibers. J Neurosci 16(18):5715-5726
7. Kohli V, Elezzabi AY (2008) Laser surgery of zebrafish (Danio rerio) embryos using femtosecond laser pulses: Optimal parameters for exogenous material delivery, and the laser's effect on short- and long-term development. BMC Biotechnol. doi:10.1186/1472-6750-8-7
8. Heilmann, I, Pidkowich MS (2004) Switching desaturase enzyme specificity by alternate subcellular targeting. Proc Natl Acad Sci USA 101(28):10266-10271
9. Stevenson DJ, Gunn-Moore FJ, Campbell P et al (2010) Single cell optical transfection. J R Soc Interface 7(47):863-871
10. Zhang H, Liu KK (2008) Optical tweezers for single cells. J R Soc Interface 5(24):671-690
11. Berns MW, Aist J, Edwards J et al (1981) Laser Microsurgery in Cell and Developmental Biology. Science 13(4507):505-513
12. Block SM (1998) Construction of Optical Tweezers. In: Cells: A Laboratory Manual, Volume 2, Cold Spring Harbor Laboratory Press, Woodbury
13. Lee WM, Reece PJ, Marchington RF et al (2007) Construction and calibration of an optical trap on a fluorescence optical microscope. Nat Protoc 2(12):3226-3238
14. Jeffries GDM, Edgar JS, Zhao Y et al (2007) Using Polarization-Shaped Optical Vortex Traps for Single-Cell Nanosurgery. Nano Lett 7(2):415-420
15. Curtis JE, Koss BA, Grier DG (2002) Dynamic holographic optical tweezers. Opt Commun 207:169-175
16. Martín-Badosa E, Montes-Usategui M, Carnicer A et al (2007) Design strategies for optimizing holographic optical tweezers set-ups. J Opt A-Pure Appl Op 9:S267-S277
17. Mejean CO, Schaefer AW, Millman EA et al (2009) Multiplexed force measurements on live cells with holographic optical tweezers. Opt Express 17(8):6209-6217
18. Rohrbach A, Tischer C, Neumayer D et al (2004) Trapping and tracking a local probe with a photonic force microscope. Rev Sci Instrum 75(6):2197-2210
19. Moffitt JR, Chemla YR, Smith SB et al (2008) Recent Advances in Optical Tweezers. Annu Rev Biochem 77:205-228
20. Ashkin A (1970) Acceleration and Trapping of Particles by Radiation Pressure. Phys Rev Lett 24(4):156-159
21. Allen PB, Doepker, BR, Chiu DT (2009) High-Throughput Capillary-Electrophoresis Analysis of the Contents of a Single Mitochondria. Anal Chem 81(10):3784-3791

List of References

1. Adhikari, S.; Selmke, M.; Cichos, F. Temperature Dependent Single Molecule Rotational Dynamics in PMA. *Phys. Chem. Chem. Phys.* **2011**, *13*, 1849–1856.
2. Ahmed, W. .; Leavesley, S. .; Rajwa, B.; Ayyaz, M. .; Ghafoor, A.; Robinson, J. . State of the Art in Information Extraction and Quantitative Analysis for Multimodality Biomolecular Imaging. *Proceedings of the IEEE* **2008**, *96*, 512–531.
3. Akbulut, M.; Ginart, P.; Gindy, M. E.; Theriault, C.; Chin, K. H.; Soboyejo, W.; Prud'homme, R. K. Generic Method of Preparing Multifunctional Fluorescent Nanoparticles Using Flash Nanoprecipitation. *Advanced Functional Materials* **2009**, *19*, 718–725.
4. Albertorio, F.; Daniel, S.; Cremer, P. S. Supported Lipopolymer Membranes as Nanoscale Filters: Simultaneous Protein Reconition and Size-Selection Assays. *J. Am. Chem. Soc.* **2006**, *128*, 7168–7169.
5. Alexandridis, P.; Holzwarth, J. F.; Hatton, T. A. Micellization of Poly(ethylene oxide)-Poly(propylene oxide)-Poly(ethylene Oxide) Triblock Copolymers in Aqueous Solutions: Thermodynamics of Copolymer Association. *Macromolecules* **1994**, *27*, 2414–2425.
6. Allen, P. B.; Sgro, A. E.; Chao, D. L.; Doepker, B. E.; Scott Edgar, J.; Shen, K.; Chiu, D. T. Single-synapse Ablation and Long-term Imaging in Live C. Elegans. *Journal of Neuroscience Methods* **2008**, *173*, 20–26.
7. Allen, P. B.; Doepker, B. R.; Chiu, D. T. Fourier Transform Capillary Electrophoresis with Laminar-Flow Gated Pressure Injection. *Anal. Chem.* **2007**, *79*, 6807–6815.
8. Allen, P. B.; Rodriguez, I.; Kuyper, C. L.; Lorenz, R. M.; Spicar-Mihalic, P.; Kuo, J. S.; Chiu, D. T. Selective Electroless and Electrolytic Deposition of Metal for Applications in Microfluidics: Fabrication of a Microthermocouple. *Anal. Chem.* **2003**, *75*, 1578–1583.
9. Allen, P. B.; Chiu, D. Alzheimer's Disease Protein Abeta1-42 Does Not Disrupt Isolated Synaptic Vesicles. *Biochimica et Biophysica Acta* **2008**, *1782*, 326–334.
10. Allen, P. B.; Doepker, B. R.; Chiu, D. T. High-Throughput Capillary-Electrophoresis Analysis of the Contents of a Single Mitochondria. *Analytical Chemistry* **2009**, *81*, 3784–3791.
11. Altman, R. B.; Terry, D. S.; Zhou, Z.; Zheng, Q.; Geggier, P.; Kolster, R. A.; Zhao, Y.; Javitch, J. A.; Warren, J. D.; Blanchard, S. C. Cyanine Fluorophore Derivatives with Enhanced Photostability. *Nat Meth* **2012**, *9*, 68–71.
12. Altman, R. B.; Zheng, Q.; Zhou, Z.; Terry, D. S.; Warren, J. D.; Blanchard, S. C. Enhanced Photostability of Cyanine Fluorophores Across the Visible Spectrum. *Nature Methods* **2012**, *9*, 428–429.
13. Anantharam, A.; Onoa, B.; Edwards, R. H.; Holz, R. W.; Axelrod, D. Localized Topological Changes of the Plasma Membrane Upon Exocytosis Visualized by Polarized TIRFM. *The Journal of Cell* **2010**, *188*, 415–428.

14. Andersson-Engels, S.; Klinteberg, C. af; Svanberg, K.; Svanberg, S. In Vivo Fluorescence Imaging for Tissue Diagnostics. *Phys. Med. Biol.* **1997**, *42*, 815–824.
15. Aran, K.; Sasso, L. A.; Kamdar, N.; Zahn, J. D. Irreversible, Direct Bonding of Nanoporous Polymer Membranes to PDMS or Glass Microdevices. *Lab on a Chip* **2009**, *10*, 548–552.
16. Arlt, J.; Garces-Chavez, V.; Sibbett, W.; Dholakia, K. Optical Micromanipulation Using a Bessel Light Beam. *Optics Communications* **2001**, *197*, 239–245.
17. Armendariz, K. P.; Huckabay, H. A.; Livanec, P. W.; Dunn, R. C. Single Molecule Probes of Membrane Structure: Orientation of BODIPY Probes in DPPC as a Function of Probe Structure. *Analyst* **2012**, *137*, 1402–1408.
18. Ashkin, A. Acceleration and Trapping of Particles by Radiation Pressure. *Physical Review Letters* **1970**, *24*, 156–159.
19. Ashkin, A.; Dziedzic, J. M.; Bjorkholm, J. E.; Chu, S. Observation of a Single-beam Gradient Force Optical Trap for Dielectric Particles. *Optics Letters* **1986**, *11*, 288–290.
20. Atkins, P.; Paula, J. de *Physical Chemistry*; 9th ed.; Oxford University Press, 2009.
21. Axelrod, D. Carbocyanine Dye Orientation in Red Cell Membrane Studied by Microscopic Fluorescence Polarization. *Biophysical Journal* **1979**, *26*, 557–574.
22. Axelrod, D. Cell-substrate Contacts Illuminated by Total Internal Reflection Fluorescence. *JCB* **1981**, *89*, 141–145.
23. Axelrod, D. Total Internal Reflection Fluorescence Microscopy in Cell Biology. *Traffic* **2001**, *2*, 764–774.
24. Bagshaw, C. R.; Cherny, D. Blinking Fluorophores: What Do They Tell Us About Protein Dynamics? *Biochemical Society Transactions* **2006**, *34*.
25. Bajjalieh, S. M.; Frantz, G. D.; Weimann, J. M.; McConnell, S. K.; Scheller, R. H. Differential Expression of Synaptic Vesicle Protein 2 (SV2) Isoforms. *The Journal of Neuroscience* **1994**, *14*, 5223–5235.
26. Bajjalieh, S. M.; Peterson, K.; Linial, M.; Scheller, R. H. Brain Contains Two Forms of Synaptic Vesicle Protein 2. *Proc. Natl. Acad. Sci. USA* **1993**, *90*, 2150–2154.
27. Bajzer, Ž.; Moncrieffe, M. C.; Penzar, I.; Prendergast, F. G. Complex Homogeneous and Heterogeneous Fluorescence Anisotropy Decays: Enhancing Analysis Accuracy. *Biophysical Journal* **2001**, *81*, 1765–1775.
28. Barandeh, F.; Nguyen, P.-L.; Kumar, R.; Iacobucci, G. J.; Kuznicki, M. L.; Kosterman, A.; Bergey, E. J.; Prasad, P. N.; Gunawardena, S. Organically Modified Silica Nanoparticles Are Biocompatible and Can Be Targeted to Neurons In Vivo. *PLoS ONE* **2012**, *7*, e29424.
29. Barbara, P. F.; Gesquiere, A. J.; Park, S.-J.; Lee, Y. J. Single-Molecule Spectroscopy of Conjugated Polymers. *Accounts of Chemical Research* **2005**, *38*, 602–610.
30. Barenholz, Y.; Clerc, S. A Quantitative Model for Using Acridine Orange as a Transmembrane pH Gradient Probe. *Analytical Biochemistry* **1997**, *259*, 104–111.

31. Bartko, A. B.; Dickson, R. M. Three-Dimensional Orientations of Polymer-Bound Single Molecules. *The Journal of Physical Chemistry B* **1999**, *103*, 3053–3056.
32. Beausang, J. F.; Schroeder 3rd, H. W.; Nelson, P. C.; Goldman, Y. E. Twirling of Actin by Myosins II and V Observed via Polarized TIRF in a Modified Gliding Assay. *Biophysical Journal 95*, 5820–5831.
33. Becer, R. C.; Babiuch, K.; Pilz, D.; Hornig, S.; Heinze, T.; Gottschaldt, M.; Schubert, U. S. Clicking Pentafluorostyrene Copolymers: Synthesis, Nanoprecipitation, and Glycosylation. *Macromolecules* **2009**, *42*, 2387–2394.
34. Beechem, J. M.; Brand, L. Time-Resolved Fluorescence of Proteins. *Annual Review of Biochemistry* **1985**, *54*, 43–71.
35. Beer, N. R.; Hindson, B. J.; Wheeler, E. K.; Hall, S. B.; Rose, K. A.; Kennedy, I. M.; Colston, B. W. On-Chip, Real-Time, Single-Copy Polymerase Chain Reaction in Picoliter Droplets. *Anal. Chem.* **2007**, *79*, 8471–8475.
36. Belcher, J. D.; Dyke, R. W. Van Acidification of Three Types of Liver Endocytic Vesicles: Similarities and Differences. *Am J Physiol Cell Physiol* **1994**, *266*, C81–C94.
37. Berliner, E.; Young, E. C.; Anderson, K.; Mahtani, H. K.; Gelles, J. Failure of a Single-headed Kinesin to Track Parallel to Microtubule Protofilaments. *Nature* **1995**, *373*, 718–721.
38. Berns, M. W.; Tadir, Y.; Liang, H.; Tromberg, B. Laser Scissors and Tweezers. *Methods Cell Biol.* **1998**, *55*, 71–98.
39. Berns, M. W.; Aist, J.; Edwards, J.; Strahs, K.; Griton, J.; McNeill, P.; Rattner, J. B.; Kitzes, M.; Peterson, S.; Brenner, S. *et al.* Laser Microsurgery in Cell and Developmental Biology. *Science* **1981**, *13*, 505–513.
40. Beyenbach, K. W.; Wieczorek, H. The V-type H+ ATPase: Molecular Structure and Function, Physiological Roles and Regulation. *The Journal of Experimental Biology* **2006**, *209*, 577–589.
41. Bilati, U.; Allemann, E.; Doelker, E. Nanoprecipitation Versus Emulsion-based Techniques for the Encapsulation of Proteins Into Biodegradable Nanoparticles and Process-related Stability Issues. *AAPS PharmSciTech* **2005**, *6*, E594–E604.
42. Blake, D. A.; Forsberg, A. S.; Johansson, B. R.; Wikland, M. Laser Zona Pellucida Thinning-an Alternative Approach to Assisted Hatching. *Human Reproduction* **2001**, *16*, 1959–1964.
43. Block, S. M. Construction of Optical Tweezers. *Cells: A Laboratory Manual* **1998**, *2*.
44. Block, S. M. Making Light Work with Optical Tweezers. *Nature* **1992**, *360*, 493–495.
45. Börsch, M.; Diez, M.; Zimmermann, B.; Reuter, R.; Gräber, P. Stepwise Rotation of the Γ-subunit of EF0F1-ATP Synthase Observed by Intramolecular Single-molecule Fluorescence Resonance Energy Transfer. *FEBS Letters* **2002**, *527*, 147–152.
46. Bos, M. A.; Kleijn, J. M. Determination of the Orientation Distribution of Adsorbed Fluorophores Using TIRF. I. Theory. *Biophysical Journal* **1995**, *68*, 2566–2572.

47. Bos, M. A.; Kleijn, J. M. Determination of the Orientation Distribution of Adsorbed Fluorophores Using TIRF. II. Measurements on Porphyrin and Cytochrome c. *Biophysical Journal* **1995**, *68*, 2573–2579.
48. Boyarsky, G.; Ganz, M. B.; Bernd Sterzel, R.; Boron, W. F. pH Regulation in Single Glomerular Mesangial Cells I. Acid Extrusion in Absence and Presence of HCO3-. *Am J Physiol Cell Physiol* **1988**, *24*, C844–C856.
49. Brasen, J. C.; Dewitt, S.; Hallett, M. B. A Reporter of UV Intensity Delivered to the Cytosol During Photolytic Uncaging. *Biophysical Journal* **2010**, *98*, L25–L27.
50. Brown, M. P.; Royer, C. Fluorescence Spectroscopy as a Tool to Investigate Protein Interactions. *Current Opinion in Biotechnology* **1997**, *8*, 45–49.
51. Buckley, K.; Kelly, R. B. Identification of a Transmembrane Glycoprotein Specific for Secretory Vesicles of Neural and Endocrine Cells. *Journal of Cell Biology* **1985**, *100*, 1284–1294.
52. Budzinski, K. L.; Allen, R. W.; Fujimoto, B. S.; Kensel-Hammes, P.; Belnap, D. M.; Bajjalieh, S. M.; Chiu, D. T. Large Structural Change in Isolated Synaptic Vesicles Upon Loading with Neurotransmitter. *Biophysical Journal* **2009**, *97*, 2577–2584.
53. Caplow, M.; Shanks, J.; Ruhlen, R. How Taxol Modulates Microtubule Disassembly. *The Journal of Biological Chemistry* **1994**, *269*, 23399–23402.
54. Castellana, E. T.; Cremer, P. S. Solid Supported Lipid Bilayers: From Biophysical Studies to Sensor Design. *Surface Science Reports* **2006**, *61*, 429–444.
55. Castorph, S.; Riedel, D.; Arleth, L.; Sztucki, M.; Jahn, R.; Holt, M.; Salditt, T. Structure Parameters of Synaptic Vesicles Quantified by Small-Angle X-Ray Scattering. *Biophysical Journal* **2010**, *98*, 1200–1208.
56. Center for History and New Media Zotero Quick Start Guide http://zotero.org/support/quick_start_guide.
57. Cerullo, G.; Graupner, W.; Lanzani, G.; Nisoli, M.; List, E. J. W.; Stagira, S.; Silvestri, S. D.; Leising, G. Ultrafast Excitation Energy Transfer in a Blend of Light-Emitting Conjugated Polymers. *Synthetic Metals 101*, 306–307.
58. Chan, Y.-H.; Jin, Y.; Wu, C.; Chiu, D. T. Copper(II) and iron(II) Ion Sensing with Semiconducting Polymer Dots. *Chemical Communications* **2011**, *47*, 2820–2822.
59. Chan, Y.-H.; Wu, C.; Ye, F.; Jin, Y.; Smith, P. B.; Chiu, D. T. Development of Ultrabright Semiconducting Polymer Dots for Ratiometric pH Sensing. *Analytical Chemistry* **2011**, *83*, 1448–1455.
60. Chang, T. N.; Keshishian, H. Laser Ablation of Drosophilia Embryonic Motoneurons Causes Ectopic Innervation of Target Muscle Fibers. *The Journal of Neuroscience* **1996**, *16*, 5715.5726.
61. Chang, W.-P.; Sudhof, T. C. SV2 Renders Primed Synaptic Vesicles Competent for Ca2+-induced Exocytosis. *The Journal of Neuroscience* **2009**, *29*, 883–897.
62. Cheng, N.-S. Formula for the Viscosity of a Glycerol-Water Mixture. *Ind. Eng. Chem. Res.* **2008**, *47*, 3285–3288.
63. Chiu, D. T. Micro- and Nano-scale Chemical Analysis of Individual Sub-cellular Compartments. *TrAC Trends in Analytical Chemistry* **2003**, *22*, 528–536.

64. Chiu, D. T. Aqueous Droplets as Single-Molecule Reaction Containers. In *Solid-State Sensors, Actuators and Microsystems Conference, 2007. TRANSDUCERS 2007. International*; 2007; pp. 465–468.
65. Cho, E. C.; Zhang, Q.; Xia, Y. The Effect of Sedimentation and Diffusion on Cellular Uptake of Gold Nanoparticles. *Nature Nanotechnology* **2011**, *6*, 385–391.
66. Chretien, D.; Metoz, F.; Verde, F.; Karsenti, E.; Wade, R. H. Lattice Defects in Microtubules: Protofilament Numbers Vary Within Individual Microtubules. *Journal of Cell Biology* **1992**, *117*, 1031–1040.
67. Chrétien, D.; Wade, R. R. New Data on the Microtubule Surface Lattice. *Biol Cell* **1991**, *71*, 161–174.
68. Chung, S. H.; Mazur, E. Femtosecond Laser Ablation of Neurons in C. Elegans for Behavioral Studies. *Applied Physics A* **2009**, *96*, 335–341.
69. Cognet, L.; Harms, G. S.; Blab, G. A.; Lommerse, P. H. M.; Schmidt, T. Simultaneous Dual-color and Dual-polarization Imaing of Single Molecules. *Applied Physics Letters* **2000**, *77*, 4052–4054.
70. Collini, E.; Scholes, G. D. Coherent Intrachain Energy Migration in a Conjugated Polymer at Room Temperature. *Science* **2009**, *323*, 369–373.
71. Cr, M.; Sj, K.; J, M. Photorefractive keratectomy: a technique for laser refractive surgery. *J Cataract Refract Surg* **1988**, *14*, 46–52.
72. Cremer, P. S.; Groves, J. T.; Kung, L. A.; Boxer, S. G. Writing and Erasing Barriers to Lateral Mobility into Fluid Phospholipid Bilayers. *Langmuir* **1999**, *15*, 3893–3896.
73. Cross, A. J.; Fleming, G. R. Analysis of Time-Resolved Fluorescence Anisotropy Decays. *Biophysical Journal* **1984**, *46*, 45–56.
74. Crowder, K. M.; Gunther, J. M.; Jones, T. A.; Hale, B. D.; Zhang, H. Z.; Peterson, M. R.; Scheller, R. H.; Chavkin, C.; Bajjalieh, S. M. Abnormal Neurotransmission in Mice Lacking Synaptic Vesicle Protein 2A. *PNAS* **1999**, *96*, 15268–15273.
75. Cumming, G.; Fidler, F.; Vaux, D. L. Error Bars in Experimental Biology. *Journal of Cell Biology* **2007**, *177*, 7–11.
76. Curtis, J. E.; Koss, B. A.; Grier, D. G. Dynamic Holographic Optical Tweezers. *Optics Communications* **2002**, *207*, 169–175.
77. Cusido, J.; Battal, M.; Deniz, E.; Yildiz, I.; Sortino, S.; Raymo, F. M. Fast Fluorescence Switching Within Hydrophilic Supramolecular Assemblies. *Chemistry - A European Journal* **2012**, *18*, 10399–10407.
78. Custer, K. L.; Austin, N. S.; Sullivan, J. M.; Bajjalieh, S. M. Synaptic Vesicle Protein 2 Enhances Release Probability at Quiescent Synapses. *The Journal of Neuroscience* **2006**, *26*, 1303–1313.
79. Daniels, R. W.; Collins, C. A.; Gelfand, M. V.; Dant, J.; Brooks, E. S.; Krantz, D. E.; DiAntonio, A. Increased Expression of the Drosophilia Vesicular Glutamate Transporter Leads to Excess Glutamate Release and a Compensatory Decrease in Quantal Content. *The Journal of Neuroscience* **2004**, *24*, 10466–10474.

80. Dave, R.; Terry, D. S.; Munro, J. B.; Blanchard, S. C. Mitigating Unwanted Photophysical Processes for Improved Single-Molecule Fluorescence Imaging. *Biop* **2009**, *96*, 2371–2381.
81. Denk, W.; Strickler, J. H.; Webb, W. W. Two-Photon Laser Scanning Fluorescence Microscopy. *Science* **1990**, *248*, 73–76.
82. Denk, W.; Webb, W. W. Optical Measurement of Picometer Displacements of Transparent Microscopic Objects. *Appl. Opt.* **1990**, *29*, 2382–2391.
83. Derfus, A. M.; Chan, W. C. W.; Bhatia, S. N. Probing the Cytotoxicity of Semiconductor Quantum Dots. *Nano Letters* **2004**, *4*, 11–18.
84. Dertinger, T.; Colyer, R.; Iyer, G.; Weiss, S.; Enderlein, J. Fast, Background-free, 3D Super-resolution Optical Fluctuation Imaging (SOFI). *Proceedings of the National Academy of Sciences of the United States of America* **2009**, *106*, 22287–22292.
85. Dholakia, K.; Spalding, G.; MacDonald, M. Optical Tweezers: The Next Generation.
86. Dı´az, J. F.; Valpuesta, J. M.; Chaco´ n, P.; Diakun, G.; Andreu, J. M. Changes in Microtubule Protofilament Number Induced by Taxol Binding to an Easily Accessible Site. *The Journal of Biological Chemistry* **1998**, *273*, 33803–33810.
87. Dickson, R. M.; Cubitt, A. B.; Tsien, R. Y.; Moerner, W. E. On/off Blinking and Switching Behavior of Single Molecules of Green Fluorescent Protein. *Nature* **1997**, *388*, 355–358.
88. Dickson, R. M.; Norris, D. J.; Moerner, W. E. Simultaneous Imaging of Individual Molecules Aligned Both Parallel and Perpendicular to the Optic Axis. *Physical Review Letters* **1998**, *81*, 5322–5325.
89. Dickson, R. M.; Norris, D. J.; Tzeng, Y.-L.; Moerner, W. E. Three-Dimensional Imaging of Single Molecules Solvated in Pores of Poly(acrylamide) Gels. *Science* **1996**, *274*, 966–969.
90. Diez, M.; Zimmermann, B.; Börsch, M.; König, M.; Schweinberger, E.; Steigmiller, S.; Reuter, R.; Felekyan, S.; Kudryavstev, V.; Seidel, C. A. M. *et al.* Proton-powered Subunit Rotation in Single Membrane-bound F0F1-ATP Synthase. *Nature Structural & Molecular Biology* **2004**, *11*, 135–141.
91. Dix, J. A.; Verkman, A. S. Mapping of Fluorescence Anisotropy in Living Cells by Ratio Imaging. *Biophysical Journal* **1990**, *57*, 231–240.
92. Docchio, F.; Avigo, A.; Palumbo, R. Characteristics of Optical Breakdown in Ultrapure Water Induced by Nanosecond Nd:YAG Laser Pulses. *Europhysics Letters* **1991**, *15*, 69–73.
93. Dodson, G. G.; Lane, D. P.; Verma, C. S. Molecular Simulations of Protein Dynamics: New Windows on Mechanisms in Biology. *EMBO reports* **2008**, *9*, 144–150.
94. Dong, M.; Yeh, F.; Tepp, W. H.; Dean, C.; Johnson, E. A.; Janz, R.; Chapman, E. R. SV2 Is the Protein Receptor for Botulinum Neurotoxin A. *Science* **2006**, *312*, 592–596.

95. Eastman, S. J.; Siegel, C.; Tousignant, J.; ASmith, A. E.; Cheng, S. H.; Scheule, R. K. Biophysical Characterization of Cationic lipid:DNA Complexes. *Biochemica et Biophysica Acta* **1997**, *1325*, 41–62.
96. Edgar, J. S.; Pabbati, C. P.; Lorenz, R. M.; He, M.; Fiorini, G. S.; Chiu, D. T. Capillary Electrophoresis Separation in the Presence of an Immiscible Boundary for Droplet Analysis. *Anal. Chem.* **2006**, *78*, 6948–6954.
97. Edidin, M. Rotational and Translational Diffusion in Membranes. *Annu. Rev. Biophys. Bioeng.* **1974**, 179–201.
98. Eisert, W. G.; Beisker, W. Epi-Illumination Optical Design for Fluorescence Polarization Measurements in Flow Systems. *Biophysical Journal* **1980**, *31*, 97–112.
99. Elbashir, S. M.; Lendeckel, W.; Tuschl, T. RNA Interference Is Mediated by 21- and 22-nucleotide RNAs 10.1101/gad.862301. *Genes Dev.* **2001**, *15*, 188–200.
100. Endow, S. A.; Kull, J.; Liu, H. Kinesins at a Glance. *Journal of Cell Science* **2010**, *123*, 3420–3424.
101. Farkas, B.; Geretovszky, Z. On Determining the Spot Size for Laser Fluence Measurements. *Applied Surface Science Proceedings of the European Materials Research society 2005 - Symposium-J: Advances in Laser and Lamp Processing of Functional Materials - EMRS 2005 Symposium J* **2006**, *252*, 4728–4732.
102. Feany, M. B.; Lee, S.; Edwards, R. H.; Buckley, K. M. The Synaptic Vesicle Protein SV2 Is a Novel Type of Transmembrane Transporter. *Cell* **1992**, *70*, 861–867.
103. Felgner, P. L.; Gadek, T. R.; Holm, M.; Roman, R.; Chan, H. W.; Wenz, M.; Northrop, J. P.; Ringold, G. M.; Danielsen, M. Lipofection: A highly efficient, lipid-mediated DNA-transfection procedure. In *Proc. Natl. Acad. Sci.*; 1987; pp. 7413–7417.
104. Fernandez-Busnadiego, R.; Zuber, B.; Maurer, U. E.; Cyrklaff, M.; Baumeister, W.; Lucic, C. Quantitative Analysis of the Native Presynaptic Cytomatrix by Cryoelectron Tomography. *Journal of Cell Biology* **2010**.
105. Fessi, H.; Puisieux, F.; Devissaguet, J. P.; Ammoury, N.; Benita, S. Nanocapsule Formation by Interfacial Polymer Deposition Following Solvent Displacement. *International Journal of Pharmaceutics* **1989**, *55*, R1–R4.
106. Fink, M. C.; Marcus, A. H. Simultaneous Measurement of Fluorescence Anisotropy and Translational Fluctuations by Polarization-modulated MFICS. *Philosophical Magazine* **2008**, *88*, 3947–3951.
107. Forkey, J. N.; Quinlan, M. E.; Shaw, M. A.; Corrie, J. E. T.; Goldman, Y. E. Three-dimensional Structural Dynamics of Myosin V by Single-molecule Fluorescence Polarization. *Nature* **2003**, *422*, 399–404.
108. Fourkas, J. T. Rapid Determination of the Three-dimensional Orientation of Single Molecules. *Optics Letters* **2001**, *26*, 211–213.
109. Frank, J.; Radermacher, M. SPIDER and WEB: Processing and Visualization of Images in 3D Electron Microscopy and Related Fields. *Journal of Structural Biology* **1996**, *116*, 190–199.

110. Fu, H.-B.; Yao, J.-N. Size Effects on the Optical Properties of Organic Nanoparticles. *J. Am* **2001**, *123*, 1434–1439.
111. Fukui, K.; Minezawa, M.; Kamisugi, Y.; Ishikawa, M.; Ohmido, N.; Yanagisawa, T.; Fujishita, M.; Sakai, F. Microdissection of Plant Chromosomes by Argon-ion Laser Beam. *Theoret. Appl. Genetics* **1992**, *84*, 787–791.
112. Fukui, K.; Minezawa, M.; Kamisugi, Y.; Ishikawa, M.; Ohmido, N.; Yanagisawa, T.; Fujishita, M.; Sakai, F. Microdissection of Plant Chromosomes by Argon-ion Laser Beam. *Theoret. Appl. Genetics* **1992**, *84*, 787–791.
113. Funatsu, T.; Harada, Y.; Tokunaga, M.; Saito, K.; Yanagida, T. Imaging of Single Fluorsecent Molecules and Individual ATP Turnovers by Single Myosin Molecules in Aqueous Solution. *Nature* **1995**, *374*, 555–559.
114. Gallindo-Rodriguez, S.; Allemann, E.; Fessi, H.; Doelker, E. Physiochemical Parameters Associated with Nanoparticle Formation in the Salting-out, Emulsification-Diffusion, and Nanoprecipitation Methods. *Pharmaceutical Research* **2004**, *21*, 1428–1438.
115. Gardner, M. K.; Charlebois, B. D.; Ja´ nosi,, I. M.; Howard, J.; Hunt, A. J.; Odde, D. J. Rapid Microtubule Self-Assembly Kinetics. *Cell 146*, 582–592.
116. Gesquiere, A. J.; Lee, Y. J.; Yu, J.; Barbara, P. F. Single Molecule Modulation Spectroscopy of Conjugated Polymers. *J. Phys. Chem. B* **2005**, *109*, 12366–12371.
117. Gidwani, A.; Holowka, D.; Baird, B. Fluorescence Anisotropy Measurements of Lipid Order in Plasma Membranes and Lipid Rafts from RBL-2H3 Mast Cells. *Biochemistry* **2001**, *40*, 12422–12429.
118. Giepmans, B. N. G.; Adams, S. R.; Ellisman, M. H.; Tsien, R. Y. The Fluorescent Toolbox for Assessing Protein Location and Function. *Science* **2006**, *312*, 217–224.
119. Greer, L. F. I.; Szalay, A. A. Imaging of Light Emission from the Expression of Luciferases in Living Cells and Organisms: a Review. *Luminescence* **2002**, *17*, 43–74.
120. Grier, D. G. A Revolution in Optical Manipulation. *Nature* **2003**, *424*, 810–816.
121. Grievenkamp, J. E. *Field Guide to Geometrical Optics*; SPIE Press: Bellingham, WA USA, 2004; Vol. FG01.
122. Grigalevicius, S.; Forster, M.; Ellinger, S.; Landfester, K.; Scherf, U. Excitation Energy Transfer from Semi-Conducting Polymer Nanoparticles to Surface-Bound Fluorescent Dyes. *Macromolecular Rapid Communications* **2006**, *27*, 200–202.
123. Gronborg, M.; Pavlos, N. J.; Brunk, I.; Chua, J. J. E.; Agnieszka, M.-W.; Riedel, D.; Ahnert-Hilger, G.; Urlaub, H.; Jahn, R. Quantitative Comparison of Glutamatergic and GABAergic Synaptic Vesicles Unveils Selectivity for Few Proteins Including MAL2, a Novel Synaptic Vesicle Protein. *Journal of Neuroscience* **2010**, *30*, 2–12.
124. Gun, B. T. F. van der; Melchers, L. J.; Ruiters, M. H. J.; Leij, L. F. M. H. d.; McLaughlin, P. M. J.; Rots, M. G. EpCAM in Carcinogenesis: The Good, the Bad or the Ugly. *Carcinogenesis* **2010**, *31*, 1913–1921.

125. Hajjar, E.; Mahendran, K. R.; Kumar, A.; Bessonov, A.; Petrescu, M.; Weingart, H.; Ruggerone, P.; Winterhalter, M.; Ceccarelli, M. Bridging Timescales and Length Scales: From Macroscopic Flux to the Molecular Mechanism of Antibiotic Diffusion Through Porins. *Biophysical Journal* **2010**, *98*, 569–575.
126. Hammer, D. X.; Jansen, D. E.; Frenz, M.; Noojin, G. D.; Thomas, R. J.; Noack, J.; Vogel, A.; Rockwell, B. A.; Welch, A. J. Shielding Properties of Laser-induced Breakdown in Water for Pulse Durations from 5 Ns to 125 Fs. *Applied Optics* **1997**, *36*, 5630–5640.
127. Hashim, Z.; Howes, P.; Green, M. Luminescent Quantum-dot-sized Conjugated Polymer Nanoparticles-nanoparticle Formation in a Miniemulsion System. *Journal of Materials Chemistry* **2011**, *21*, 1797–1803.
128. He, M.; Edgar, J. S.; Jeffries, G. D. M.; Lorenz, R. M.; Shelby, J. P.; Chiu, D. T. Selective Encapsulation of Single Cells and Subcellular Organelles into Picoliter- and Femtoliter-Volume Droplets. *Anal. Chem.* **2005**, *77*, 1539–1544.
129. He, M.; Kuo, J. S.; Chiu, D. T. Effects of Ultrasmall Orifices on the Electrogeneration of Femtoliter-Volume Aqueous Droplets. *Langmuir* **2006**, *22*, 6408–6413.
130. He, M.; Sun, C.; Chiu, D. T. Concentrating Solutes and Nanoparticles Within Individual Aqueous Microdroplets. *Anal. Chem.* **2004**, *76*, 1222–1227.
131. He, M.; Kuo, J. S.; Chiu, D. T. Electro-generation of Single Femtoliter- and Picoliter-volume Aqueous Droplets in Microfluidic Systems. *Applied Physics Letters* **2005**, *87*, 031916.
132. Heilmann, I.; Pidkowich, M. S.; Girke, T.; Shanklin, J. Switching Desaturase Enzyme Specificity by Alternate Subcellular Targeting. *Proc Natl Acad Sci USA* **2004**, *101*, 10266–10271.
133. Heisterkamp, A.; Maxwell, I. Z.; Mazur, E.; Underwood, J. M.; Nickerson, J. A.; Kumar, S.; Ingber, D. E. Pulse Energy Dependence of Subcellular Dissection by Femtosecond Laser Pulses. *Optics Express* **2005**, *13*, 3690–3696.
134. Henriksen, H.; Taylor, A. R.; Brownlee, C.; Assmann, S. M. Laser Microsurgery of Higher Plant Cell Walls Permits Patch-Clamp Access. *Plant Physiology* **1996**, *110*, 1063–1068.
135. Hide, F.; DÍaz-GarcÍa, M. A.; Schwartz, B. J.; Heeger, A. J. New Developments in the Photonic Applications of Conjugated Polymers. *Accounts of Chemical Research 30*, 430–436.
136. Hill, J. J.; Royer, C. Fluorescence Approaches to Study of Protein-Nucleic Acid Complexation. *Methods in Enzymology* **1997**, *278*.
137. Hirata, T.; Iwamoto-Kihara, A.; Sun-Wada, G.-H.; Okajima, T.; Wada, Y.; Futai, M. Subunit Rotation of Vacuolar-type Proton Pumping ATPase: Relative Rotation of the G and c Subunits. *The Journal of Biological Chemistry* **2003**, *278*, 23714–23719.
138. Holden, M. A.; Cremer, P. S. Light Activated Patterning of Dye-Labeled Molecules of Surfaces. *J. Am. Chem. Soc.* **2003**, *125*, 8074–8075.

139. Holt, M.; Riedel, D.; Schuette, C.; Jahn, R. Synaptic Vesicles Are Constitutively Active Fusion Machines That Function Independently of Ca2+. *Current Biology* **2008**, *18*, 715–722.
140. Hu, D.; Yu, J.; Wong, K.; Bagchi, B.; Rossky, P. J.; Barbara, P. F. Collapse of Stiff Conjugated Polymers with Chemical Defects into Ordered, Cylindrical Conformations. *Nature* **2000**, *405*, 1030–1033.
141. Huang, B.; Bates, M.; Zhuang, X. Super Resolution Fluorescence Microscopy. *Annu Rev Biochem* **2009**, *78*, 993–1016.
142. Huang, K.; Murphy, R. F. From Quantitative Microscopy to Automated Image Understanding. *J. Biomed. Opt* **2004**, *9*, 893–912.
143. Huang, T.; Nallathamby, P. D.; Gillet, D.; Xu, X.-H. N. Design and Synthesis of Single-Nanoparticle Optical Biosensors for Imaging and Characterization of Single Receptor Molecules on Single Living Cells. *Anal. Chem.* **2007**, *79*, 7708–7718.
144. Huser, T.; Yan, M.; Rothberg, L. J. Single Chain Spectroscopy of Conformational Dependence of Conjugated Polymer Photophysics. *Proc Natl Acad Sci USA* **2000**, *97*, 11187–11191.
145. Hyeon, C.; Onuchic, J. N. A Structural Perspective on the Dynamics of Kinesin Motors. *Biophysical Journal* **2011**, *101*, 2749–2759.
146. Hyman, A. A.; Salser, S.; Drechsel, D. N.; Unwin, N.; Mitchison, T. J. Role of GTP Hydrolysis in Microtubule Dynamics: Information from a Slowly Hydrolyzable Analogue, GMPCPP. *Molecular Biology of the Cell* **1992**, *3*, 1155–1167.
147. Imamura, H.; Nakano, M.; Noji, H.; Muneyuki, E.; Ohkuma, S.; Yoshida, M.; Yokoyama, K. Evidence for Rotation of V1-ATPase. *Proceedings of the National Academy of Sciences of the United States of America* **2003**, *100*, 2312–2315.
148. Innocenti, B.; Parpura, V.; Haydon, P. G. Imaging Extracellular Waves of Glutamate During Calcium Signaling in Cultured Astrocytes. *The Journal of Neuroscience* **2000**, *20*, 1800–1808.
149. Jahnig, F. Structural Order of Lipids and Proteins in Membranes: Evaluation of Fluorescence Anisotropy Data. *Proc. Natl. Acad. Sci. USA* **1979**, *76*, 6361–6365.
150. Jakubiak, R.; Collison, C. J.; Wan, W. C.; Rothberg, L. J. Aggregation Quenching of Luminescence in Electroluminescent Conjugated Polymers. *Journal of Physical Chemistry A* **1999**, *103*, 2394–2398.
151. Jameson, D. M.; Ross, J. A. Fluorescence Polarization/Anisotropy in Diagnostics and Imaging. *Chemical Reviews* **2010**, *110*, 2685–2708.
152. Janshoff, A.; Neitzert, M.; Oberdorfer, Y.; Fuchs, H. Force Spectroscopy of Molecular Systems - Single Molecule Spectroscopy of Polymers and Biomolecules. *Angewandte Chemie* **2000**, *39*, 3212–3237.
153. Janz, R.; Goda, Y.; Geppert, M.; Missler, M.; Südhof, T. C. SV2A and SV2B Function as Redundant Ca2+ Regulators in Neurotransmitter Release. *Neuron* **1999**, *24*, 1003–1016.

154. Jeffries, G. D. M.; Edgar, J. S.; Zhao, Y.; Shelby, J. P.; Fong, C.; Chiu, D. T. Using Polarization-Shaped Optical Vortex Traps for Single-Cell Nanosurgery. *Nano Lett.* **2007**, *7*, 415–420.
155. Jeffries, G. D. M.; Kuo, J. S.; Chiu, D. T. Controlled Shrinkage and Re-expansion of a Single Aqueous Droplet Inside an Optical Vortex Trap. *J. Phys. Chem. B* **2007**, *111*, 2806–2812.
156. Jessel, R.; Haertel, S.; Socaciu, C.; Tykhonova, S.; Diehl, H. A. Kinetics of Apoptotic Markers in Exogeneously Induced Apoptosis of EL4 Cells. *Journal of Cellular and Molecular Medicine* **2002**, *6*, 82–92.
157. Jin, Y.; Ye, F.; Zeigler, M.; Wu, C.; Chiu, D. T. Near-Infrared Fluorescent Dye-Doped Semiconducting Polymer Dots. *ACS Nano* **2011**, *5*, 1468–1475.
158. Johnson, B. K.; Prud'homme, R. K. Mechanism for Rapid Self-Assembly of Block Copolymer Nanoparticles. *Physical Review Letters 91*, 118302–1–118302–4.
159. *Molecular Probes Handbook, A Guide to Fluorescent Probes and Labeling Technologies*; Johnson, I.; Spence, M. T. Z., Eds.; 11th ed.; Life Technologies, 2010.
160. Jones, H. M.; Kunhardt, E. E. Pre-breakdown Currents in Water and Aqueous Solutions and Their Influence on Pulsed Dielectric Breakdown. *Journal of Applied Physics* **1994**, *78*, 3308–3314.
161. Jordan, M.; Wurm, F. Transfection of Adherent and Suspended Cells by Calcium Phosphate. *Methods* **2003**, *33*, 136–143.
162. Jung, S. Y.; Holden, M. A.; Cremer, P. S.; Collier, P. C. Two-Component Membrane Lithography via Lipid Backfilling. *ChemPhysChem* **2005**, *6*, 423–426.
163. Kaan, H. Y. K.; Hackney, D. D.; Kozielski, F. The Structure of the Kinesin-1 Motor-Tail Complex Reveals the Mechanism of Autoinhibition. *Science 333*, 883–885.
164. Kaminski, C. Quantitative Fluorescence Microscopy. *Journal of the Royal* **2009**, *6*, S1–S2.
165. Kampmann M; Atkinson C.E; Mattheyses A.L; Simon S.M Mapping the orientation of nuclear pore proteins in living cells with polarized fluorescence microscopy. *Nat. Struct. Mol. Biol. Nature Structural and Molecular Biology* **2011**, *18*, 643–649.
166. Kask, P.; Palo, K.; Ullmann, D.; Gall, K. Fluorescence-intensity Distribution Analysis and Its Application to Biomolecular Detection Technology. *Proceedings of the National Academy of Sciences of the United States of America* **1999**, *96*, 13756–13761.
167. Kassu, A.; Taguenang, J. M.; Sharma, A. Photopatterning of Polybutadiene Substrates by Interferometric Ultraviolet Lithography: Fabrication of Phospholipid Microarrays. *Applied Optics* **2007**, *46*, 489–494.
168. Kastrup, L.; Hell, S. W. Absolute Optical Cross Section of Individual Fluorescent Molecules. *Angewandte Chemie International Edition* **2004**, *43*, 2–5.

169. Kerssemakers, J. W. J.; Janson, M. E.; Horst, A. van der; Dogterom, M. Optical Trap Setup for Measuring Microtubule Pushing Forces. *Applied Physics Letters* **2003**, *83*, 4441–4443.
170. Khodjakov, A.; Cole, R. W.; Rieder, C. L. A Synergy of Technologies: Combining Laser Microsurgery With Green Fluorescent Protein Tagging. *Cell Motility and the Cytoskeleton* **1997**, *38*, 311–317.
171. Kinoshita, K. J.; Itoh, H.; Ishiwata, S.; Hirano, K.; Takayuki, N.; Hayakawa, T. Dual-View Microscopy with a Single Camera: Real-Time Imaging of Molecular Orientations and Calcium. *Journal of Cell Biology* **1991**, *115*, 67–73.
172. Klärner, G.; Lee, J.-I.; Davey, M. H.; Miller, R. D. Exciton Migration and Trapping in Copolymers Based on Dialkylfluorenes. *Advanced Materials* **1999**, *11*, 115–119.
173. Kleefen, A.; Pedone, D.; Grunwald, C.; Wei, R.; Firnkas, M.; Abstreiter, G.; Rant, U.; Tampé, R. Multiplexed Parallel Single Transport Recordings on Nanopore Arrays. *Nano Lett.* **2010**.
174. Koffie, R. M.; Farrar, C. T.; Saidi, L.-J.; William, C. M.; Hyman, B. T.; Spires-Jones, T. L. Nanoparticles Enhance Brain Delivery of Blood-brain Barrier-impenetrable Probes for in Vivo Optical and Magnetic Resonance Imaging. *Proceedings of the National Academy of Sciences of the United States of America* **2011**, *108*, 18837–18842.
175. Kohli, V.; Acker, J. P.; Elezzabi, A. Y. Reversible Permeabilization Using High-Intensity Femtosecond Laser Pulses: Applications to Biopreservation. *Biotechnology and Bioengineering* **2005**, *92*, 889–899.
176. Kohli, V.; Elezzabi, A. Y.; Acker, J. P. Cell Nanosurgery Using Ultrashort (Femtosecond) Laser Pulses: Applications to Membrane Surgery and Cell Isolation. *Lasers in Surgery and Medicine* **2005**, *37*, 227–230.
177. Kohli, V.; Elezzabi, A. Y. Laser Surgery of Zebrafish (Danio Rerio) Embryos Using Femtosecond Laser Pulses: Optimal Parameters for Exogenous Material Delivery, and the Laser's Effect on Short- and Long-term Development. *BMC Biotechnology* **2008**, *8*.
178. Kohli, V.; Elezzabi, A. Y. Prospects and Developments in Cell and Embryo Laser Nanosurgery. *Nanomedicine and Nanobiotechnology* **2009**, *1*, 11–25.
179. Kolb, H. C. Click Chemistry: Diverse Chemical Function from a Few Good Reactions.
180. Krasieva, T. B.; Chapman, C. F.; LaMorte, V. J.; Venugopalan, B.; Berns, M. W.; Tromberg, B. J. Cell Permeabilization and Molecular Transport by Laser Microirradiation. *SPIE Proceedings* **1998**, *3260*, 38–44.
181. Kratohvil, J. P.; Lee, M.-P.; Kerker, M. Angular Distribution of Fluorescence from Small Particles. *Applied Optics* **1978**, *17*, 1978–1980.
182. Kretzschmar, S.; Volknandt, W.; Zimmermann, H. Colocalization on the Same Synaptic Vesicles of Syntaxin and SNAP-25 with Synaptic Vesicle Proteins: a Re-evaluation of Functional Models Required? *Neuroscience Research* **1996**, *26*, 141–148.

183. Kuimova, M. K.; Botchway, S. W.; Parker, A. W.; Balaz, M.; Collins, H. A.; Anderson, H. L.; Suhling, K.; Ogilby, P. R. Imaging Intracellular Viscosity of a Single Cell During Photoinduced Cell Death. *Nature Chemistry* **2009**, *1*, 69–73.
184. Kuimova, M. K.; Yahioglu, G.; Levitt, J. A.; Suhling, K. Molecular Rotor Measures Viscosity of Live Cells via Fluorescence Lifetime Imaging. *J. Am. Chem. Soc.* **2008**, *130*, 6672–6673.
185. Kuyper, C. L.; Brewood, G. P.; Chiu, D. T. Initiating Conformation Transitions of Individual YOYO-Intercalated DNA Molecules with Optical Trapping. *Nano Letters* **2003**, *3*, 1387–1389.
186. Kyriacou, S. V.; Brownlow, W. J.; X.-H.N, X. Using Nanoparticle Optics Assay for Direct Observation of the Function of Antimicrobial Agents in Single Live Bacterial Cells. *Biochemistry* **2004**, *43*, 140–147.
187. Lai, C.-Y.; Wu, C.-H.; Chen, C.-C.; Li, P.-C. Quantitative Relations between Acoustic Inertial Cavitation and Gene Transfection Rate/Cell Viability. In *2005 IEEE Ultrasonics Symposium*; 2005.
188. Lakowicz, J. R. *Principles of Fluorescence Spectroscopy*; 3rd ed.; Springer, 2006.
189. Lapotko, D. O.; Lukianova, E. Y.; Shnip, A. I. Photothermal Detection of Laser-induced Damage in Single Intact Cells. *Lasers in Surgery and Medicine* **2003**, *33*, 320–329.
190. Lavis, L. D.; Raines, R. T. Bright Ideas for Chemical Biology. *ACS Chemical Biology* **2008**, *3*, 142–155.
191. Lee, J.-I.; Zyung, T.; Miller, R. D.; Kim, Y. H.; Jeoung, S. C.; Kim, D. Photoluminescence Study on Exciton Migration and Trapping in a Copolymer Based on Poly(fluorene). *Journal of Materials Chemistry* **2000**, *10*, 1547–1550.
192. Lee, J. Y.; Lesoine, J. F.; Krogmeier, J. R.; Kang, H.; Clarke, M.; Chang, R.; Sackett, D. L.; Nossal, R.; Hwang, J. Real-time Fluorescence Polarization Microscopy for Probing Local Distributions of Biomolecules. *Proceedings of SPIE* **2011**, *7891*.
193. Lee, J. B.; Hong, J.; Bonner, D. K.; Poon, Z.; Hammond, P. T. Self-assembled RNA Interference Microsponges for Efficient siRNA Delivery. *Nat Mater* **2012**, *advance online publication*.
194. Lee, K.-S.; El-Sayed, M. A. Gold and Silver Nanoparticles in Sensing and Imaging: Sensitivity of Plasmon Response to Size, Shape, and Metal Composition. *J. Phys. Chem. B* **2006**, *110*, 19220–19225.
195. Lee, W. M.; Reece, P. J.; Marchington, R. F.; Metzger, N. K.; Dholakia, K. Construction and Calibration of an Optical Trap on a Fluorescence Optical Microscope. *Nat. Protocols* **2007**, *2*, 3226–3238.
196. Lee, W.-K.; Kim, H.-J.; Min, H.-K.; Kang, U.-B.; Lee, C.; Lee, S.-W.; Kim, I. Y.; Lee, S.-T.; Kwon, O.-S.; Yu, Y. G. A Comprehensive Identification of Synaptic Vesicle Proteins in Rat Brains by cRPLC/MS-MS and 2DE/MALDI-TOF-MS. *Bull. Korean Chem, Soc.* **2007**, *28*, 1499–1509.
197. Lichtman, J. W.; Conchello, J.-A. Fluorescence Microscopy. *Nature Methods 2*, 910–919.

198. Lieb, M. A.; Zavislan, J. M.; Novotny, L. Single-molecule Orientations Determined by Direct Emission Pattern Imaging. *Journal of the Optical Society of America B* **2004**, *21*, 1210–1215.
199. Lin, Y.; Böker, A.; He, J.; Sill, K.; Xiang, H.; Abetz, C.; Li, X.; Wang, J.; Emrick, T.; Long, S. *et al.* Self-directed Self-assembly of Nanoparticle/copolymer Mixtures. *Nature* **2005**, *434*, 55–59.
200. List, E. J. W.; Creely, C.; Leising, G.; Schulte, N.; Schlu¨ter, A. D.; Scherf, U.; Mu¨llen, K.; Graupner, W. Excitation Energy Migration in Highly Emissive Semiconducting Polymers. *Chemical Physics Letters* **2000**, *325*, 132–138.
201. Liu, Y.; Ogawa, K.; Schanze, K. S. Conjugated Polyelectrolytes as Fluorescent Sensors. *Journal of Photochemistry and Photobiology C: Photochemistry Reviews* **2009**, *10*, 173–190.
202. Liu, Y.; Edwards, R. H. The Role of Vesicular Transport Proteins in Synaptic Transmission and Neural Degeneration. *Annu. Rev. Neurosci.* **1997**, *20*, 125–156.
203. Livanec, P. W.; Dunn, R. C. Single-Molecule Probes of Lipid Membrane Structure. *Langmuir* **2008**, *24*, 14066–14073.
204. Lizard, G.; Fournel, S.; Genestier, L.; Dhedin, N.; Chaput, C.; Flacher, M.; Mutin, M.; Panaye, G.; Revillard, J. P. Kinetics of Plasma Membrane and Mitochondrial Alterations in Cells Undergoing Apoptosis. *Cytometry* **1995**, *21*, 275–283.
205. Lorenz, R. M.; Edgar, J. S.; Jeffries, G. D. M.; Chiu, D. T. Microfluidic and Optical Systems for the On-Demand Generation and Manipulation of Single Femtoliter-Volume Aqueous Droplets. *Anal. Chem.* **2006**, *78*, 6433–6439.
206. Lorenz, R. M.; Edgar, J. S.; Jeffries, G. D. M.; Zhao, Y.; McGloin, D.; Chiu, D. T. Vortex-Trap-Induced Fusion of Femtoliter-Volume Aqueous Droplets. *Anal. Chem.* **2007**, *79*, 224–228.
207. Loss, S. R.; Will, T.; Marra, P. P. The Impact of Free-ranging Domestic Cats on Wildlife of the United States. *Nature Communications* **2013**, *4*, 1396.
208. Lucido, A. L.; Gopalakrishnan, G.; Yam, P. T.; Colman, D. R.; Lennox, B. R. Isolation of Functional Presynaptic Complexes from CNS Neurons: A Cell-Free Preparation for the Study of Presynaptic Compartments In Vitro. *ACS Chem. Neurosci.* **2010**, *1*, 535–541.
209. Lynch, B. A.; Lambeng, N.; Nocka, K.; Kensel-Hammes, P.; Bajjalieh, S. M.; Matagne, A.; Fuks, B. The Synapticvesicle Protein SV2A Is the Binding Site for the Antiepileptic Drug Levetiracetam. *Proc. Natl. Acad. Sci. USA* **2004**, *101*, 9861–9866.
210. Marešová, L.; Hošková, B.; Urbánková, E.; Chaloupka, R.; Sychrová, H. New Applications If pHluorin - Measuring Intracelular pH of Prototrophic Yeasts and Determining Changes in the Buffering Capacity of Strains with Affected Potassium Homeostasis. *Yeast* **2010**, *27*, 317–325.
211. Marshansky, V.; Futai, M. The V-type H+-ATPase in Vesicular Trafficking: Targeting, Regulation and Function. *Current Opinion in Cell Biology* **2008**, *20*, 415–426.

212. Martín-Badosa, E.; Montes-Usategui, M.; Carnicer, A.; Andilla, J.; Pleguezuelos, E.; Juvells, I. Design Strategies for Optimizing Holographic Optical Tweezers Set-ups. *Journal of Optics A: Pure and Applied Optics* **2007**, *9*, S267–S277.
213. Mataga, N.; Kaifu, Y.; Koizumi, M. Solvent Effects Upon Fluorescence Spectra and the Dipolemoments of Excited Molecules. *Bulletin of the Chemical Society of Japan* **1956**, *29*, 465–470.
214. Mattheyses, A. L.; Kampmann, M.; Atkinson, C. E.; Simon, S. M. Fluorescence Anisotropy Reveals Order and Disorder of Protein Domains in the Nuclear Pore Complex. *Biophysical Journal* **2010**, *99*, 1706–1717.
215. Maycox, P. R.; Deckwerth, T.; Hell, J. W.; Jahn, R. Glutamate Uptake by Brain Synaptic Vesicles. *The Journal of Bological Chemistry* **1988**, *263*, 15423–15428.
216. McCauley, T. G.; Hamaguchi, N.; Stanton, M. Aptamer-based Biosensor Arrays for Detection and Quantification of Biological Macromolecules. *Analytical Biochemistry* **2003**, *319*, 244–250.
217. McFarland, A. D.; Duyne, R. P. Van Single Silver Nanoparticles as Real-Time Optical Sensors with Zeptomole Sensitivity. *Nano Letters* **2003**, *3*, 1057–1062.
218. McMahan, U. J.; Marshall, R. M.; Stoschek, A.; Ress, D.; Harlow, M. L. The Architecture of Active Zone Material at the Frog's Neuromuscular Junction. *Nature* **2001**, *409*, 479–484.
219. Medina, C.; Santos-Martinez, M. J.; Radomski, A.; Corrigan, O. I.; Radomski, M. W. Nanoparticles: Pharmacological and Toxicological Significance. *Br J Pharmacol* **2007**, *150*, 552–558.
220. Mehier-Humbert, S.; Guy, R. H. Physical Methods for Gene Transfer: Improving the Kinetics of Gene Delivery into Cells. *Advanced Drug Delivery Reviews Pharmacokinetics in Gene Delivery* **2005**, *57*, 733–753.
221. Mejean, C. O.; Schaefer, A. W.; Millman, E. A.; Forscher, P.; Dufresne, E. R. Multiplexed Force Measurements on Live Cells with Holographic Optical Tweezers. *Optics Express* **2009**, *17*, 6209–6217.
222. Melnik, V. I.; Bikbulatova, L. S.; Gulyaeva, N. V.; Bazyan, A. S. Synaptic Vesicle Acidification and Exocytosis Studied with Acridine Orange Fluorescence in Rat Brain Synaptosomes. *Neurochemical Research* **2001**, *26*, 549–554.
223. Meng, Q.; Li, Z.; Li, G.; Zhang, X.; An, Y.; Zhu, X. X. Aggregation of Biotinylated Polymeric Microspheres Induced by Interaction with Avidin. *Pure Appl. Chem.* **2007**, *79*, 1575–1582.
224. Michalet, X.; Pinaud, F.; Lacoste, T. D.; Dahan, M.; Bruchez, M. P.; Alivisatos, A. P.; Weiss, S. Properties of Fluorescent Semiconductor Nanocrystals and Their Application to Biological Labeling. *Single Mol.* **2001**, *2*, 261–276.
225. Miller-Jaster, K. N.; Petrie Aronin, C. E.; Guilford, W. H. A Quantitative Comparison of Blocking Agents in the In Vitro Motility Assay. *Biomedical Engineering Society* **2012**, *5*, 44–51.
226. Min, Y.; Akbulut, M.; Kristiansen, K.; Golan, Y.; Israelachvili, J. The Role of Interparticle and External Forces in Nanoparticle Assembly. *Nature Materials* **2008**, *7*, 527–538.

227. Moffitt, J. R.; Chemla, Y. R.; Smith, S. B.; Bustamante, C. Recent Advances in Optical Tweezers. *Annual Reviews of Biochemistry* **2008**, *77*, 205–228.
228. Moffitt, J. R.; Chemla, Y. R.; Smith, S. B.; Bustamante, C. Recent Advances in Optical Tweezers. *Annual Review of Biochemistry* **2008**, *77*, 205–228.
229. Mogensen, M. M.; Tucker, J. B. Taxol Influences Control of Protofilament Number at Microtubule-nucleating Sites in Drosophila. *J Cell Sci* **1990**, *97*, 101–107.
230. Mogensen, M. M.; Tucker, J. B. Taxol Influences Control of Protofilament Number at Microtubule-nucleating Sites in Drosophilia. *Journal of Cell Science* **1990**, *97*, 101–107.
231. Mohanty, S. K.; Rapp, A.; Monajembashi, S.; Gupta, P. K.; Greulich, K. O. Comet Assay Measurements of DNA Damage in Cells by Laser Microbeams and Trapping Beams With Wavelengths Spanning a Range of 308 Nm to 1064 Nm. *Radiation Research* **2002**, *157*, 378–385.
232. Morgans, C. W.; Kensel-Hammes, P.; Hurley, J. B.; Burton, K.; Idzerda, R.; McKnight, G. S.; Bajjalieh, S. M. Loss of the Synaptic Vesicle Protein SV2B Results in Reduced Neurotransmission and Altered Synaptic Vesicle Protein Expression in the Retina. *PLoS ONE* **2009**, *4*, 1–8?
233. Müller, C. B.; Loman, A.; Pacheco, V.; Koberling, F.; Willbold, D.; Richtering, W.; Enderlein, J. Precise Measurement of Diffusion by Multi-color Dual-focus Fluorescence Correlation Spectroscopy. *Europhysics Letters* **2008**, *83*, 46001.
234. Mun, J. S.; Jo, J.; Heeger, A. J. Nanomorphology of PCDTBT: P70BM Bulk Heterojunction Solar Cells. *Advanced Energy Materials* **2012**, *2*, 304–308.
235. Mutch, S. A.; Kensel-Hammes, P.; Gadd, J. C.; Fujimoto, B. S.; Allen, R. W.; Schiro, P. G.; Lorenz, R. M.; Kuyper, C. L.; Kuo, J. S.; Bajjalieh, S. M. *et al.* Protein Quantification at the Single Vesicle Level Reveals a Subset of Synaptic Vesicle Proteins Are Trafficked with High Precision. *The Journal of Neuroscience* **2011**, *31*.
236. Nagata, S.; Obana, A.; Gohto, Y.; Nakajima, S. Necrotic and Apoptotic Cell Death of Human Malignant Melanoma Cells Following Photodynamic Therapy Using an Amphiphilic Photosensitizer, ATX-S10(Na). *Lasers in Surgery and Medicine* **2003**, *33*, 64–70.
237. Naoki Nakajima; Yoshito Ikada Mechanism of Amide Formation by Carbodiimide for Bioconjugation in Aqueous Media. *Bioconjugate Chem. 6*, 123–130.
238. Nasir, M. S.; Jolley, M. E. Fluorescence Polarization: An Analytical Tool for Immunoassay and Drug Discovery. *Combinatorial Chemistry & High Throughput Screening* **1999**, *2*, 177–190.
239. Naumann, R.; Jonczyk, A.; Kopp, R.; Esch, J. van; Ringsdorf, H.; Knoll, W.; Gräber, P. Incorporation of Membrane Proeins in Solid-Supported Lipid Layers. *Angewandte Chemie* **2003**, *34*, 2056–2058.
240. Neuman, K. C.; Block, S. M. Optical Trapping. *Review of Scientific Instruments* **2004**, *75*, 2787–2809.

241. Ng, J.; Lin, Z.; Chan, C. T. Theory of Optical Trapping by an Optical Vortex Beam. *Phys. Rev. Lett.* **2010**, *104*, 103601.
242. Nguyen, T.-Q.; Doan, V.; Schwartz, B. J. Conjugated Polymer Aggregates in Solution: Control of Interchain Interactions. *Journal of Chemical Physics* **1999**, *110*, 4068–4078.
243. Niemz, M. H. *Laser-Tissue Interactions: Funamentals and Applications*; Springer: Heidelberg, Germany, 2004.
244. Nitzsche, B.; Ruhnow, F.; Diez, S. Quantum-dot-assisted Characterization of Microtubule Rotations During Cargo Transport. *Nature Nanotechnology* **2008**, *3*, 552–556.
245. Ohkohchi, N.; Itagaki, H.; Hideyuki, D.; Taguchi, Y.; Satomi, S.; Satoh, S. New Technique for Producing Hybridoma by Using Laser Irradiation. *Lasers in Surgery and Medicine* **2000**, *27*, 262–268.
246. Palumbo, G.; Caruso, M.; Crescenzi, E.; Tecce, M. F.; Roberti, G.; Colasanti, A. Targeted Gene Transfer in Eukaryotic Cells by Dye-assisted Laser Optoporation. *Journal of Photochemistry and Photobiology B: Biology* **1996**, *36*, 41–46.
247. Paterson, L.; Agate, B.; Comrie, M.; Ferguson, R.; Lake, T. K.; Morris, J. E.; Carruthers, A. E.; Brown, C. T. A.; Sibbett, W.; Bryant, P. E. *et al.* Photoporation and Cell Transfection Using a Violet Diode Laser. *Optics Express* **2005**, *13*, 595–600.
248. Peterman, E. J. G.; Sosa, H.; Goldstein, L. S. B.; Moerner, W. E. Polarized Fluorescence Microscopy of Individual and Many Kinesin Motors Bound to Axonemal Microtubules. *Biophysical Journal* **2001**, *81*, 2851–2863.
249. Petkau, K.; Kaeser, A.; Fischer, I.; Brunsveld, L.; Schenning, A. P. H. J. Pre- and Postfunctionalized Self-assembled Π-conjugated Fluorescent Organic Nanoparticles for Dual Targeting. *J. Am. Chem. Soc.* **2011**, *133*, 17063–17071.
250. Pittman IV, I.; Nakagawa, S. H.; Tager, H. S.; Steiner, D. F. Maintenance of the B-chain Beta-turn in [GlyB24] Insulin Mutants: a Steady-state Fluorescence Anisotropy Study. *Biochemistry* **1997**, *36*, 3430–3437.
251. Poon, Z.; Chang, D.; Zhao, X.; Hammond, P. T. Layer-by-Layer Nanoparticles with a pH-Sheddable Layer for in Vivo Targeting of Tumor Hypoxia. *ACS Nano* **2011**.
252. Pyle, R. A.; Schivell, A. E.; Hidaka, H.; Bajjalieh, S. M. Phosphorylation of Synaptic Vesicle Protein 2 Modulates Binding to Synaptotagmin. *The Journal of Bological Chemistry* **2000**, *275*, 17195–17200.
253. Quinto-Su, P. A.; Hsuan-Hong, L.; Yoon, H. H.; Sims, C. E.; Allbritton, N. L.; Venugopalan, V. Examination of Laser Microbeam Cell Lysis in a PDMS Microfluidic Channel Using Time-resolved Imaging. *Lab on a Chip* **2008**, *8*, 408–414.
254. Rahamimoff, R.; Fernandez, J. M. Pre- and Postfusion Regulation of Transmitter Release. *Neuron* **1997**, *18*, 17–27.
255. Reicherter M; Haist T; Wagemann EU; Tiziani HJ Optical particle trapping with computer-generated holograms written on a liquid-crystal display. *Optics letters* **1999**, *24*, 608–10.

256. Reichman, J. *Handbook of Optical Filters for Fluorescence Microscopy*; Chroma Technology, 2010.
257. Reigada, D.; Díez-Pérez, I.; Gorostiza, P.; Verdaguer, A.; Gómez de Aranda, I.; Pineda, O.; Vilarrasa, J.; Marsal, J.; Blasi, J.; Aleu, J. *et al.* Control of Neurotransmitter Release by an Internal Gel Matrix in Synaptic Vesicles. *Proceedings of the National Academy of Sciences of the United States of America* **2003**, *100*, 3485–3490.
258. Resch-Genger, U.; Grabolle, M.; Cavaliere-Jaricot, S.; Nitschke, R.; Nann, T. Quantum dots versus organic dyes as fluorescent labels. *Nat Meth Nature Methods* **2008**, *5*, 763–775.
259. Rizzoli, S. O.; Betz, W. J. The Structural Organization of the Readily Releasable Pool of Synaptic Vesicles. *Science* **2004**, *303*, 2037–2039.
260. Rohrbach, A.; Tischer, C.; Neumayer, D.; Florin, E.-L.; Stelzer, E. H. K. Trapping and Tracking a Local Probe with a Photonic Force Microscope. *Review of Scientific Instruments* **2004**, *75*, 2197–2210.
261. Rong, Y.; Wu, C.; Yu, J.; Zhang, X.; Ye, F.; Zeigler, M.; Gallina, M. E.; Wu, I.-C.; Zhang, Y.; Chan, Y.-H. *et al.* Multicolor Fluorescent Semiconducting Polymer Dots with Narrow Emissions and High Brightness. *ACS Nano* **2013**, *7*, 376–384.
262. Roos, A.; Boron, W. F. Intracellular pH. *Physiological Reviews* **1981**, *61*, 296–434.
263. Rubenstein, J. L.; Merzenich, M. M. Model of Autism: Increased Ratio of Excitation/inhibition in Key Neural Systems. *Genes, Brain and Behavior* **2003**, *2*, 255–267.
264. Rusinova, E.; Tretyachenko-Ladokhina, V.; Vele, O. E.; Senear, D. F.; Alexander Ross, J. B. Alexa and Oregon Green Dyes as Fluorescence Anisotropy Probes for Measuring Protein-protein and Protein-nucleic Acid Interactions. *Analytical Biochemistry* **2002**, *308*, 18–25.
265. Ryan, T. A. Presynaptic Imaging Techniques. *Current Opinion in Neurobiology* **2001**, *11*, 544–549.
266. Salmena, Leonardo; Poliseno, Laura; Tay, Yvonne; Kats, Lev; Pandolfi, Pier Paolo A ceRNA Hypothesis: The Rosetta Stone of a Hidden RNA Language? *Cell 146*, 353–358.
267. Sanghamitra, R.; Meyerhöfer, E.; Milligan, R. A.; Howard, J. Kinesin Follows the Microtubule's Protofilament Axis. *The Journal of Cell Biology* **1993**, *121*, 1083–1093.
268. Sapsford, K. E.; Tyner, K. M.; Dair, B. J.; Deschamps, J. R.; Medintz, I. L. Analyzing Nanomaterial Bioconjugates: A Review of Current and Emerging Purification and Characterization Techniques. *Analytical Chemistry 83*, 4453–4488.
269. Sase, I.; Miyata, H.; Corrie, J. E. T.; Craik, J. S.; Kinosita, K. J. Real Time Imaging of Single Fluorophores on Moving Actin with an Epifluorescence Microscope. *Biophysical Journal* **1995**, *69*, 323–328.

270. Sase, I.; Miyata, H.; Ishiwata, S.; Kinosita, K. J. Axial Rotation of Sliding Actin Filaments Revealed by Single-fluorophore Imaging. *Proceedings of the National Academy of Sciences of the United States of America* **1997**, *94*, 5456–5650.
271. Schartel, B.; Wachtendorf, V.; Grell, M.; Bradley, D. D. C.; Hennecke, M. Polarized Fluorescence and Orientational Order Parameters of a Liquid-crystalline Conjugated Polymer. *Physical Review B* **1999**, *60*, 277–283.
272. Schmidt, T.; Schütz, G. J.; Baumgartner, W.; Gruber, H. J.; Schindler, H. Imaging of Single Molecule Diffusion. *PNAS* **1996**, *93*, 2926–2929.
273. Schneckenburger, H. Total Internal Reflection Fluorescence Microscopy: Technical Innovations and Novel Applications. *Current Opinion in Biotechnology* **2005**, *16*, 13–18.
274. Schneckenburger, H.; Hendinger, A.; Sailer, R.; Strauss, W. S. L.; Schmitt, M. Laser-assisted Optoporation of Single Cells. *Journal of Biomedical Optics* **2002**, *7*, 410–416.
275. Schubert, S.; Delaney, J. T. J.; Schubert, U. S. Nanoprecipitation and Nanoformulation of Polymers: From History to Powerful Possibilities Beyond Poly(lactic Acid). *Soft Matter* **2011**, *7*, 1581–1588.
276. Schultz, S.; Smith, D. R.; Mock, J. J.; Schultz, D. A. Single-target Molecule Detection with Nonbleaching Multicolor Optical Immunolabels. *PNAS* **1999**, *97*, 996–1001.
277. Schütz, G. J.; Schindler, H.; Schmidt, T. Imaging Single-molecule Dichroism. *Optics Letters* **1997**, *22*, 651–653.
278. Schütze, F.; Stempfle, B.; Jüngst, C.; Wöll, D.; Zumbusch, A.; Mecking, S. Fluorescent Conjugated Block Copolymer Nanoparticles by Controlled Mixing. *Chemical Communications* **2012**, *48*, 2104–2106.
279. Schwarcz, R. Effects of Tissue Storage and Freezing on Brain Glutamate Uptake. *Life Sciences* **1981**, *28*, 1147–1154.
280. Schwartz, B. J.; Nguyen, T.-Q.; Wu, J.; Tolbert, S. H. Interchain and Intrachain Exciton Transport in Conjugated Polymers: Ultrafast Studies of Energy Migration in Aligned MEG-PPV/mesoporous Silica Composites. *Synthetic Metals* **2001**, *116*, 35–40.
281. Seeger, M. A.; Rice, S. E. Microtubule-associated Protein-like Binding of the Kinesin-1 Tail to Microtubules. *The Journal of Biological Chemistry* **2010**, *285*, 8155–8162.
282. Seeger, S.; Monajembashi, S.; Hutter, K. J.; Futterman, G.; Wolfrum, J.; Greulich, K. O. Application of Laser Optical Tweezers in Immunology and Molecular Genetics. *Cytometry* **1991**, *12*, 497–504.
283. Seferos, D. S.; Giljohann, D. A.; Hill, H. D.; Prigodich, A. E.; Mirkin, C. A. Nano-Flares: Probes for Transfection and mRNA Detection in Living Cells. *J. Am. Chem. Soc.* **2007**, *129*, 15477–15479.
284. Seksek, O.; Biwerski, J.; Verkman, A. S. Translational Diffusion of Macromolecule-sized Solutes in Cytoplasm and Nucleus. *The Journal of Cell Biology* **1997**, *138*, 131–142.

285. Sgro, A. E.; Allen, P. B.; Chiu, D. T. Thermoelectric Manipulation of Aqueous Droplets in Microfluidic Devices. *Anal. Chem.* **2007**, *79*, 4845–4851.
286. Shelby, J. P.; Edgar, J. S.; Chiu, D. T. Monitoring Cell Survival After Extraction of a Single Subcellular Organelle Using Optical Trapping and Pulsed-nitrogen Laser Ablation. *Photochem. Photobiol.* **2005**, *81*, 994–1001.
287. Shelby, J. P.; Chiu, D. T. Controlled Rotation of Biological Micro- and Nano-particles in Microvortices. *Lab on a Chip* **2004**, *4*, 168–170.
288. Shelby, J. P.; Edgar, J. S.; Chiu, D. T. Monitoring Cell Survial After Extraction of a Single Subcellular Organelle Using Optical Trapping and Pulsed-Nitrogen Laser Ablation. *Photochemistry and Photobiology* **2005**, *81*, 994–1001.
289. Shin, L.; Basi, N.; Jeremic, A.; Lee, J.-S.; Cho, W. J.; Chen, Z.; Abu-Hamadah, R.; Oupicky, D.; Jena, B. P. Involvement of vH+-ATPase in Synaptic Vesicle Swelling. *Journal of Neuroscience Research* **2010**, *88*, 95–101.
290. Shribak, M.; Inoue, S.; Oldenbourg, R. Polarization Aberrations Caused by Differential Transmission and Phase Shift in High-numerical-aperture Lenses: Theory, Measurement, and Rectification. *Opt. Eng.* **2002**, *41*, 943–954.
291. Soares, M. M.; King, S. W.; Thorpe, P. E. Targeting Insode-out Phosphatidylserine as a Therapeutic Strategy for Viral Diseases. *Nature Medicine* **2008**, *14*, 1357–1362.
292. Sonar, P.; Williams, E. L.; Singh, S. P.; Dodabalapur, A. Thiophene–benzothiadiazole–thiophene (D–A–D) Based Polymers: Effect of Donor/acceptor Moieties Adjacent to D–A–D Segment on Photophysical and Photovoltaic Properties. *J. Mater. Chem.* **2011**, *21*, 10532–10541.
293. Soughayer, J. S.; Krasieva, T.; Jacobson, S. C.; Ramsey, J. M.; Tromberg, B. J.; Allbritton, N. L. Characterization of Cellular Optoporation with Distance. *Anal. Chem* **2000**, *72*, 1342–1347.
294. Spector, D. L.; Goldman, R. D.; Leinwand, L. A. *Cells: a Laboratory Manual*; Cold Spring Harbor Laboratory Press, 1998.
295. Spillmann, C. M.; Naciri, J.; Anderson, G. P.; Chen, M.-S.; Ratna, B. R. Spectral Tuning of Organic Nanocolloids by Controlled Molecular Interacions. *ACS Nano* **2009**, *3*, 3214–3220.
296. Staal, R. G. W.; Mosharov, E. V.; Sulzer, D. Dopamine Neurons Release Transmitter via a Flickering Fusion Pore. *Nature Neuroscience* **2004**, *7*, 341–346.
297. Stark, R. W.; Rubio-Sierra, F.-J.; Thalhammer, S.; Heckl, W. M. Combined Nanomanipulation by Atomic Force Microscopy and UV-Laser Ablation for Chromosomal Dissection. *Eur. Biophys. J.* **2003**, *32*, 33–39.
298. Stevenson, D.; Agate, B.; Tsampoula, X.; Fischer, P.; Brown, C. T. A.; Sibbett, W.; Riches, A.; Gunn-Moore, F.; Dholakia, K. Femtosecond Optical Transfection of Cells: Viability and Efficiency. *Optics Express* **2006**, *14*, 7125–7133.
299. Stevenson, D. J.; Gunn-Moore, F. J.; Campbell, P.; Dholakia, K. Single Cell Optical Transfection. *Journal of the Royal Society Interface* **2010**, *7*, 863–871.
300. Stokes, G. G. On the Change of Refrangibility of Light. *Philosophical Transactions of the Royal Society of London* **1852**, *142*, 462–562.

301. Sudhof, T. C. The Synaptic Vesicle Cycle: a Cascade of Protein-protein Interactions. *Nature* **1995**, *375*, 645–653.
302. Südhof, T. C. The Synaptic Vesicle Cycle. *Annual Review of Neuroscience* **2004**, *27*, 509–547.
303. Suhling, K.; French, P. M. W.; Phillips, D. Time-resolved Fluorescence Microscopy. *Photochem. Photobiol. Sci.* **2005**, *4*, 13–22.
304. Suhling, K.; Siegel, J.; Lanigan, P. M. P.; Leveque-Fort, S.; Webb, S. E. D.; Phillips, D.; Davis, D.; French, P. M. W. Time-resolved Fluorescence Anisotropy Imaging Applied to Live Cells. *Optics Letters* **2004**, *29*, 584–586.
305. Sun, B.; Chiu, D. T. Spatially and Temporally Resolved Delivery of Stimuli to Single Cells. *J. Am. Chem. Soc.* **2003**, *125*, 3702–3703.
306. Sun, B.; Chiu, D. T. Synthesis, Loading, and Application of Individual Nanocapsules for Probing Single-Cell Signaling. *Langmuir* **2004**, *20*, 4614–4620.
307. Sun, B.; Chiu, D. T. Determination of the Encapsulation Efficiency of Individual Vesicles Using Single-Vesicle Photolysis and Confocal Single-Molecule Detection. *Anal. Chem.* **2005**, *77*, 2770–2776.
308. Sun, B.; Lim, D. S. W.; Kuo, J. S.; Kuyper, C. L.; Chiu, D. T. Fast Initiation of Chemical Reactions with Laser-Induced Breakdown of a Nanoscale Partition. *Langmuir* **2004**, *20*, 9437–9440.
309. Sun, W.; Hayden, S.; Jin, Y.; Rong, Y.; Yu, J.; Ye, F.; Yang-Hsiang, C.; Zeigler, M.; Wu, C.; Chiu, D. T. A Versatile Method for Generating Semiconducting Polymer Dot Nanocomposites. *Nanoscale* **2012**, *4*, 7246–7249.
310. Supatto, W.; Debarre, D.; Moulia, B.; Brouzes, E.; Martin, J.-L.; Farge, E. In Vivo Modulation of Morphogenetic Movements in Drosophila Embryos with Femtosecond Laser Pulses. *PNAS* **2004**, *102*, 1047–1052.
311. Swaminathan, R.; Hoang, C. P.; Verkman, A. S. Photobleaching Recovery and Anisotropy Decay of Green Fluorescent Protein GFP-S65Tin Solution and Cells: Cytoplasmic Viscosity Probed by Green Fluorescent Protein Translational and Rotational Diffusion. *Biophysical Journal* **1997**, *72*, 1900–1907.
312. Szymanski, C.; Wu, C.; Hooper, J.; Salazar, M. A.; Perdomo, A.; Dukes, A.; Mcneill, J. Single Molecule Nanoparticles of the Conjugated Polymer MEH-PPV, Preparation and Characterization by Near-Field Scanning Optical Microscopy. *Journal of Physical Chemistry B Letters* **2005**, *109*, 8543–8546.
313. Tabares, L.; Ruiz, R.; Linares-Clemente, P.; Gaffield, M. A.; Alvarez de Toledo, G.; Fernanez-Chaco´n, R.; Betz, W. J. Monitoring Synaptic Function at the Neuromuscular Junction of a Mouse Expressing SynaptopHluorin. *The Journal of Neuroscience* **2007**, *27*, 5422–5430.
314. Takamori, S.; Holt, M.; Stenius, K.; Lemke, E. A.; Grønborg, M.; Riedel, D.; Urlaub, H.; Schenck, S.; Brügger, B.; Ringler, P. *et al.* Molecular Anatomy of a Trafficking Organelle. *Cell* **2006**, *127*, 831–846.
315. Tang, J.; Jofre, A. M.; Lowman, G.; Kishore, R. B.; Reiner, J. E.; Helmerson, K.; Goldner, L. S.; Greene, M. E. Green Fluorescent Protein in Inertially Injected Aqueous Nanodroplets. *Langmuir* **2008**, *24*, 4975–4978.

316. Tang, W. T.; Chung, E.; Kim, Y.; So, P. T. C.; Sheppard, C. J. R. Effects of Using a Metal Layer in Total Internal Reflection Fluorescence Microscopy. *Appl. Phys. A* **2007**, *89*, 333–335.
317. Tang, Y.; Cook, T. A.; Cohen, A. E. Limits on Fluorescence Detected Circular Dichroism of Single Helicene Molecules. *Journal of Physical Chemistry A Letters* **2009**, *113*, 6213–6216.
318. Tao, W.; Wilkinson, J.; Stanbridge, E. J.; Berns, M. W. Direct Gene Transfer into Human Cultured Cells Facilitated by Laser Micropuncture of the Cell Membrane. *PNAS* **1987**, *84*, 4180–4184.
319. Taraska, J. W.; Zagotta, W. N. Fluorescence Applications in Molecular Neurobiology. *Neuron* **2010**, *66*, 170–189.
320. Terpetschnig, E.; Szmacinski, H.; Lakowicz, J. R. Fluorescence Polarization Immunoassay of a High-Molecular-Weight Antigen Based on a Long-Lifetime Ru-Ligand Complex. *Analytical Biochemistry* **1995**, *227*, 140–147.
321. Thompson, R. E.; Larson, D. R.; Webb, W. W. Precise Nanometer Localization Analysis for Individual Fluorescent Probes. *Biophysical Journal* **2002**, *82*, 2775–2783.
322. Tirlapur, U. K.; Konig, K. Targeted Transfection by Femtosecond Laser. *Nature* **2002**, *418*, 290–291.
323. Tirlapur, U. K.; Konig, K. Femtosecond Near-infrared Laser Pulses as a Versatile Non-invasive Tool for Intra-tissue Nanoprocessing in Plants Without Compromising Viability. *The Plant Journal* **2002**, *31*, 365–374.
324. Toprak, E.; Enderlein, J.; Syed, S.; McKinney, S. A.; Petschek, R. G.; Ha, T.; Goldman, Y. E.; Selvin, P. R. Defocused Orinetation and Position Imaging (DOPI) of Myosin V. *Proc. Natl. Acad. Sci. USA* **2006**, *103*, 6495–6499.
325. Triller, A.; Choquet, D. New Concepts in Synaptic Biology Derived from Single-Molecule Imaging. *Neuron* **2008**, *59*, 359–374.
326. Urban, N. T.; Willig, K. I.; Hell, S. W.; Nägeri, U. V. STED Nanoscopy of Actin Dynamics in Synapses Deep Inside Living Brain Slices. *Biophysical Journal* **2011**, *101*, 1277–1284.
327. Uthirakumar, P.; Hong, C.-H.; Suh, E.-K.; Lee, Y.-S. Preparation and Photophysical Properties of Organic Fluorescent Polymers and Their Nanoparticles. *Journal of Appied Polymer Science* **2006**, *102*, 5344–5350.
328. Uy, J. L.; Asbury, C. L.; Petersen, T. W.; Engh, G. van den The Polarization of Fluorescence of DNA Stains Depends on the Incorporation Densityof the Dye Molecules. *Cytometry Part A* **2004**, *61A*, 18–25.
329. Vale, R. D. The Molecular Motor Toolbox for Intracellular Transport. *Cell* **2003**, *112*, 467–480.
330. Valtorta, F.; Meldolesi, J.; Fesce, R. Synaptic Vesicles: Is Kising a Matter of Competence? *TRENDS in Cell Biology* **2001**, *11*, 324–328.
331. Vaughan-Jones, R. D.; Wu, M.-L. pH Dependence of Intrinsic H+ Buffering Power in the Sheep Cardiac Purkinje Fibre. *Journal of Physiology* **1990**, *425*, 429–448.

332. Venugopalan, V.; Guerra, A.; Nahen, K.; Vogel, A. Role of Laser-Induced Plasma Formation in Pulsed Cellular Microsurgery and Micromanipulation. *Phys. Rev. Lett. J1 - PRL* **2002**, *88*, 078103.
333. Verma, V.; Hancock, W. O.; Catchmark, J. M. The Role of Casein in Supporting the Operation of Surface Bound Kinesin. *Journal of Biological Engineering 2*.
334. Villringer, A.; Chance, B. Non-invasive Optical Spectroscopy and Imaging of Human Brain Function. *Trends in Neurosciences* **1997**, *20*, 435–442.
335. Vishwasrao, H. D.; Heikal, A. A.; Kasischke, K. A.; Webb, W. W. Conformational Dependence of Intracellular NADH on Metabolic State Revealed by Associated Fluorescence Anisotropy. *The Journal of Bological Chemistry* **2005**, *280*, 25119–25126.
336. Visscher, K.; Gross, S. P.; Block, S. M. Construction of Multiple-beam Optical Traps with Nanometer-resolution Position Sensing. *IEEE Journal of Selected Topics in Quantum Electronics* **1996**, *2*, 1066 –1076.
337. Vogel, A.; Noack, J.; Huttman, G.; Paltauf, G. Mechanisms of Femtosecond Laser Nanosurgery of Cells and Tissues. *Appl. Phys. B* **2005**, *81*, 1015–1047.
338. Vogel, A.; Noack, J.; Nahen, K.; Theisen, D.; Busch, S.; Parlitz, U.; Hammer, D. X.; Noojin, G. D.; Rockwell, B. A.; Birnbruber, R. Energy Balance of Optical Breakdown in Water at Nanosecond to Femtosecond Time Scales. *Appl. Phys. B* **1999**, *68*, 271–280.
339. Vogel, A.; Venugopalan, V. Mechanisms of Pulsed Laser Ablation of Biological Tissues. *Chemical Reviews* **2003**, *103*, 577–644.
340. Vogelsang, J.; Kasper, R.; Steinhauer, C.; Person, B.; Heilmann, M.; Sauer, M.; Tinnefeld, P. A Reducing and Oxidizing System Minimizes Photobleaching and Blinking of Fluorescent Dyes. *Angewandte Chemie International Edition* **2008**, *47*, 5465–5469.
341. Wang, G.; Sun, W.; Luo, Y.; Fang, N. Resolving Rotational Motions of Nano-objects in Engineered Environments and Live Cells with Gold Nanorods and Differential Interference Contrast Microscopy. *Journal of the American Chemical Society* **2010**, *132*, 16417–16422.
342. Wang, J.; Gu, J.; Leszczynski, J. Theoretical Study of Absorption and Emission Spectra of the Monomer of PFBT. *Chemical Physics Letters* **2008**, *456*, 206–210.
343. Wang, X.; Xu, S.; Peng, L.; Wang, Z.; Wang, C.; Zhang, C.; Wang, X. Exploring Scientists' Working Timetable: Do Scientists Often Work Overtime? *Journal of Infometrics* **2012**, *6*, 655–660.
344. Weiss, S. Measuring Conformational Dynamics of Biomolecules by Single Molecule Fluorescence Spectroscopy. *Nature Structural & Molecular Biology* **2000**, *7*, 724–729.
345. Weisslender, R.; Tung, C.-H.; Mahmood, U.; Bogdanov, A. In Vivo Imaging of Tumors with Protease-activated Near-infrared Fluorescent Probes. *Nature Biotechnology* **1999**, *17*, 375–378.
346. Willets, K. A.; Duyne, R. P. V. Localized Surface Plasmon Resonance Spectroscopy and Sensing. *Ann. Rev. Phys. Chem.* **2006**, *58*, 267–297.

347. Woehlke, G.; Schliwa, M. Walking on Two Heads: The Many Talents of Kinesin. *Nature Reviews Molecular Cell Biology* **2000**, *1*, 50–58.
348. Wolosker, H.; Souza, D. O. de; Meis, L. de Regulation of Glutamate Transport into Synaptic Vesicles by Chloride and Proton Gradient. *The Journal of Biological Chemistry* **1996**, *271*, 11726–11731.
349. Wu, C.; Bull, B.; Szymanski, C.; Christensen, K.; McNeil, J. Multicolor Conjugated Polymer Dots for Biological Fluorescence Imaging. *ACS Nano* **2008**, *2*, 2415–2423.
350. Wu, C.; Chiu, D. T. Highly Fluorescent Semiconducting Polymer Dots for Biology and Medicine. *Angewandte Chemie International Edition* **2013**, n/a–n/a.
351. Wu, C.; Hansen, S. J.; Hou, Q.; Yu, J.; Zeigler, M.; Jin, Y.; Burnham, D. R.; Mcneill, J. D.; Olson, J. M.; Chiu, D. T. Design of Highly Emissive Polymer Dot Bioconjugates for In Vivo Tumor Targeting. *Angewandte Chemie* **2011**, *50*, 3430–3434.
352. Wu, C.; Jin, Y.; Schneider, T.; Burnham, D. R.; Smith, P. B.; Chiu, D. T. Ultrabright and Bioorthogonal Labeling of Cellular Targets Using Semiconducting Polymer Dots and Click Chemistry. *Angewandte Chemie International* **2010**, *49*, 9346–9440.
353. Wu, C.; Schneider, T.; Zeigler, M.; Yu, J.; Schiro, P. G.; Burnham, D. R.; McNeill, J.; Chiu, D. T. Bioconjugation of Ultrabright Semiconducting Polymer Dots for Specific Cellular Targeting. *J. Am. Chem. Soc.* **2010**, *132*, 15410–15417.
354. Wu, C.; Szymanski, C.; Cain, Z.; Mcneill, J. Conjugated Polymer Dots for Multiphoton Fluorescence Imaging. *J. Am. Chem. Soc.* **2007**, *129*, 12904–12905.
355. Wu, C.; Szymanski, C.; McNeill, J. Preparation and Encapsulation of Highly Fluorescent Conjugated Polymer Nanoparticles. *Langmuir* **2006**, *22*, 2956–2960.
356. Xu, T.; Bajjalieh, S. M. SV2 Modulates the Size of the Readily Releasable Pool of Secretory Vesicles. *Nature Cell Biology* **2001**, *3*, 691–698.
357. Xu, X.; Georganopoulou, D. G.; Hill, H. D.; Mirkin, C. A. Homogeneous Detection of Nucleic Acids Based Upon the Light Scattering Properties of Silver-Coated Nanoparticle Probes. *Anal. Chem.* **2007**, *79*, 6670–6654.
358. Yager, P.; Brody, J. P.; Bell, D. J. Using Poly(ethylene Glycol) Silane to Prevent Protein Adsorption in Microfabricated Silicon Channels. *SPIE* **1998**, *3258*, 134–139.
359. Yang, T.; Jung, S.; Mao, H.; Cremer, P. S. Fabrication of Phospholipid Bilayer-Coated Micochannels for On-Chip Immunoassays. *Analytical Chemistry* **2001**, *73*, 165–169.
360. Yguerabide, J.; Yguerabide, E. E. Light-Scattering Submicroscopic Particles as Highly Fluorescent Analogs and Their Use as Tracer Labels in CLinical and Biolgical Applications. *Anal. Biochem.* **1998**, *262*, 137–156.
361. Yildiz, A.; Selvin, P. R. Fluorescence Imaging with One Nanometer Accuracy: Application to Molecular Motors. *Accoun* **2005**, *38*, 574–582.
362. Yingling, Y. G.; Garrison, B. J. Photochemical Ablation of Organic Solids. *Nuclear Instruments and Methods in Physics Research B* **2003**, *202*, 188–194.

363. Yu, J.; Hu, D.; Barbara, P. F. Unmasking Electronic Energy Transfer of Conjugated Polymers by Suppression of O2 Quenching. *Science* **2000**, *289*, 1327 –1330.
364. Yu, J.; Wu, C.; Sahu, S. P.; Fernando, L. P.; Szymanski, C.; McNeill, J. Nanoscale 3D Tracking with Conjugated Polymer Nanoparticles. *Journal of the American Chemical Society* **2009**, *131*, 18410–18414.
365. Yu Rong, C. W. Multicolor Fluorescent Semiconducting Polymer Dots with Narrow Emissions and High Brightness. *ACS nano* **2013**.
366. Zeira, E.; Manevitch, A.; Khatchatouriants, A.; Pappo, O.; Hyam, E.; Darash-Yahana, M.; Tavor, E.; Honigman, A.; Lewis, A.; Galun, E. Femtosecond Infrared Laser- An Efficient and Safe in Vivo Gene Delivery System for Prolonged Expression. *Molecular Therapy* **2003**, *8*, 342–350.
367. Zhai, G. R.; Bellen, H. J. The Architecture of the Active Zone in Th Presynaptic Nerve Terminal. *Int. Union Physiol. Sci./Am.* **2004**, *19*, 262–270.
368. Zhang, G.; Palmer, G. M.; Dewhirst, M. W.; Fraser, C. L. A Dual-emissive-materials Design Concept Enables Tumour Hypoxia Imaging. *Nat Mater* **2009**, *8*, 747–751.
369. Zhang, H.; Liu, K.-K. Optical Tweezers for Single Cells. *Journal of the Royal Society Interface* **2008**, *5*, 671–690.
370. Zhang, Q.; Cao, Y.-Q.; Tsien, R. Y. Quantum Dots Provide an Optical Signal Specific to Full Collapse Fusion of Synaptic Vesicles. *Proc. Natl. Acad. Sci. USA* **2007**, *104*, 17843–17848.
371. Zhang, Q.; Pangršič, T.; Kreft, M.; Kržan, M.; Li, N.; Sul, J.-Y.; Halassa, M.; Bockstaele, E. V.; Zorec, R.; Haydon, P. G. Fusion-related Release of Glutamate from Astrocytes. *The Journal of Bological Chemistry* **2004**, *279*, 12724–12733.
372. Zhang, X.; Yu, J.; Wu, C.; Jin, Y.; Rong, Y.; Ye, F.; Chiu, D. T. Importance of Having Low-Density Functional Groups for Generating High-Performance Semiconducting Polymer Dots. *ACS Nano* **2012**, *6*, 5429–5439.
373. Zhang, Z.; Zhang, Z.; Jackson, M. B. Synaptotagmin IV Modulation of Vesicle Size and Fusion Pores in PC12 Cells. *Biophysical Journal* **2010**, *98*, 968–978.
374. Zhao, L. Modeling the Optical Properties of Noble Metal Nanoparticles, Nanoparticle Arrays, and Molecule-nanoparticle Complexes., 2006.
375. Zhou, Q.; Swager, T. M. Fluorescent Chemosensors Based on Energy Migration in Conjugated Polymers: The Molecular Wire Approach to Increased Sensitivity. *Journal of the American Chemical Society* **1995**, *117*, 12593–12602.
376. Zhou, Q.-H.; Miller, D. L.; Carlisle, R. C.; Seymour, L. W.; Oupicky, D. Ultrasound-enhanced Transfection Activity of HPMA-stabilized DNA Polyplexes with Prolonged Plasma Circulation. *Journal of Controlled Release* **2005**, *106*, 416–427.
377. Zhuang, X.; Ha, T.; Kim, H. D.; Centner, T.; Labeit, S.; Chu, S. Fluorescence Quenching: A Tool for Single-molecule Protein-folding Study. *Proceedings of the National Academy of Sciences of the United States of America* **2000**, *97*, 14241–14244.

378. Zoccarato, F.; Cavallini, L.; Alexandre, A. The pH-Sensitive Dye Acridine Orange as a Tool to Monitor Exocytosis/Endocytosis in Synaptosomes. *Journal of Neurochemistry* **1999**, *72*, 625–633.

Vita

Maxwell Zeigler was born and raised in Albuquerque, New Mexico. He attended the New Mexico Institute of Mining and Technology where he graduated with a Baccalaureate of Science in chemistry with a minor in biology in 2006. He joined Daniel Chiu's group at the University of Washington in 2006 where he skied, ran, salsa danced, climbed on rocks, and researched until he finished with his PhD in Chemistry in 2013.